Development of high-performance quantum dot mode-locked optical frequency comb

Shujie Pan

A thesis submitted to University College London for the degree of
Doctor of Philosophy (PhD)

Department of Electronic and Electrical Engineering

University College London

May 2022

Statement of originality

I, Shujie Pan, confirm that the work presented in this thesis is my own. Where information has been derived from other sources, I confirm that this has been indicated in the thesis.

Signed: Shujie Pan
_____

Date: 28/May/2022
_____

To my family

Abstract

This PhD thesis focus on the development of high-performance optical frequency combs (OFCs) generated by two-section passively mode-locked lasers (MLLs) based on novel optimised InAs quantum dot (QD) structures grown on GaAs substrates. Throughout the thesis, several important aspects are covered: the epitaxial structures, the device designs, the fabrication process, the characterisation of the fabricated laser devices and the evaluation of their performance.

To gain a deep level comprehension of the mode-locking mechanisms in two-section QD MLLs, a detailed study is presented on a series of QD MLLs with different saturable absorber (SA) to gain section length ratios (from 1: 3 to 1: 7) in either ridged-waveguide structure or tapered waveguide structure. The effect of temperature on different device configurations is experimentally examined. And the data transmission capability of the QD MLLs is systematically investigated in different scenarios.

In this thesis, an ultra-stable 25.5 GHz QD mode-locked OFC source emitted solely from the QD ground state from 20 °C to a world record 120 °C with only 0.07 GHz tone spacing variation has been demonstrated. Meanwhile, a passively QD MLL with 100 GHz fundamental repetition rate is developed for the first time, enabling 128 Gbit s^{-1} λ^{-1} PAM4 optical transmission and 64 Gbit s^{-1} λ^{-1} NRZ optical transmission through 5-km SSMF and 2-m free-space, respectively. All of the studies aim to prove that our two-section passively InAs QD MLLs can be used as simple, compact, easy-to-operate, and power-efficient multi-wavelength OFC sources for future high-speed and large-capacity optical communications.

Impact Statement

Due to the digitalisation of data in both commercial and home applications, the market for data centre servers has experienced tremendous growth. Currently, the explosion of demand for internet traffic imposes a heavy burden on computation, storage, and communication in data centres, which results in considerable operational expenditure to data centre providers and the internet congestion costs to end-users. Meanwhile, a key enabler for the upcoming 6G network era is 'connecting everything', which means the space, air, ground, and underwater networks will be ubiquitous and have unlimited connectivity. Therefore, optical interconnects will undoubtedly play a crucial role in future low-latency, high-speed and high-capacity communication systems.

The mode-locked optical frequency combs (OFCs) with the ability to provide tens to hundreds of equal distributed optical carriers have emerged as promising light sources for multi-wavelength coherent optical transmissions. And its employment in state-of-the-art dense wavelength-division multiplexing communication systems could be an ideal solution to effectively address the data traffic issue within the data centres. In addition, the novel quantum dot (QD) based semiconductor mode-locked lasers offer extra benefits, including small footprints, low power consumption, and great temperature stability. Therefore, this PhD research project aims to have a large impact both inside and outside academia by developing high-performance optical frequency combs based on III-V quantum dot mode-locked lasers.

This thesis is anticipated to significantly impact the semiconductor laser community by introducing new strategies to boost the performance of mode-locked OFCs. A number of promising results have been achieved due to the combined effect of QD growth conditions, device design, and advanced characterisation techniques. An ultra-stable QD passively comb source with 25.5 GHz mode-spacing, compatible with the ITU-T G.694.1 recommendation, is obtained to operate up to a record

120°C. This work has been selected as the '*Spotlight on Optics*' by the *Optical Society (OSA)*. A reliable 100 GHz QD mode-locked OFCs with a conventional two-section structure is shown to be capable of 128 Gbit s^{-1} λ^{-1} PAM4 optical fibre transmission. And this work has been invited to publish in the *special issue* of the *Journal of Physics D*. In addition, it has been confirmed for the first time that the OFCs based on 100 GHz QD MLL can be used for high-speed space transmissions. And this work has been reported at the *postdeadline session* of the *Asia Communications and Photonics (ACP) Conference*. It is hoped that our results could fulfil the future development of III-V QD mode-locked OFCs, as well as their potential integration on CMOS-compatible silicon substrate.

Economically, the multi-wavelength OFC source with broad bandwidth could potentially replace numerous individual light sources, and hence, lower the overall operating costs. Besides, the temperature-independent property of QD OFCs could eliminate the usage of expensive thermoelectric cooling systems, which can further reduce operational costs. Furthermore, society will benefit from improved communications and information processing.

Overall, the final goal of this research project is to develop compact, low-cost, energy-efficient, and highly reliable mode-locked OFCs for near-instant tera-scale data transmission and to satisfy the emerging services and applications.

Acknowledgements

The research presented in this dissertation was conducted over several years with the support of many people, for which I am extremely grateful.

First of all, I would like to express my deepest appreciation to my supervisor, Dr Siming Chen. His guidance and encouragement have greatly assisted my professional development during this PhD study. I am greatly indebted for his assistance in developing relationships with researchers in laboratories outside the UCL and for all the training opportunities he has provided me. The work presented in this dissertation would not have been possible without his invaluable insights and extraordinary efforts. I also would like to express my gratitude to my secondary supervisor, Prof. Huiyun Liu, for inspiring me to pursue a PhD after BEng.

I would like to acknowledge all current and previous members of the UCL MBE group for their help and friendships: Dr Jiang Wu, Dr Mingchu Tang, Dr Dongyoung Kim, Dr Daqian Guo, Dr Yunyan Zhang, Dr Pamela Jurczak, Dr Shun Chan, Dr Zizhuo Liu, Dr Junjie Yang, Dr Keshuang Li, Miss Ying Lu, Miss Victoria Cao, and Mr Huiwen Deng. I would also like to extend my gratitude to Dr Mengya Liao for being an excellent mentor to me. I am extremely grateful to her and Dr Jae-Seong Park for their careful readings of the manuscript and helpful comments. I have enjoyed working with you all.

My acknowledgement also goes to our collaborators: Dr Wei Li from Beijing University of Technology; Dr Zhixin Liu, Dr Zichuan Zhou and Dr Mu-chieh Lo from the UCL ONG group; Dr Zizheng Cao and Dr Jianou Huang from the Eindhoven University of Technology; Dr Ting Wang and Dr Zihao Wang from the Institute of Physics (IoP), Chinese Academy of Sciences (CAS); and Dr Xi Xiao, Dr Hongguang Zhang, Dr Xiao Hu, Mr Jie Yan, and Mr Dingyi Wu from the National Optoelectronics Innovation Center (NOEIC), for invaluable assistance in device fabrication and characterisations. All collaborations are fruitful, resulting in several high-performance mode-locked laser devices with record features.

Finally, I humbly offer my most sincere gratitude to my family, my parents, and my brother for their continuous support, unconditional trust, and endless love. Without their understanding and admiration, my research life would not be that bright and cheerful.

May. 2022

Acknowledgements (Chinese)

致 谢

行文至此，将近五年的博士生涯即将接近尾声。在撰写此博士论文期间，我曾无数次的想过要如何编辑致谢中的文字，怕遗漏了任何细节，怕词不达意，同时也怕在焦头烂额赶论文的情况下这章会被草草带过。思虑再三，在某个思绪飞扬的凌晨三点，秉承着择日不如撞日的理念，我打开了电脑并码下了这些文字。或许多年之后回看这篇致谢会觉得情感过于幼稚，但我还是希望将此时此刻的真情实感如实记录。虽然人生感激之情会常有，但是二十来岁的心态却不常在。

犹记得在二零一七年的三月，彼时做为伦敦大学学院 (UCL) 电子电机工程系 (Electro and Electronic Engineering) 三年级本科生的我在完成毕业设计的时候偶然得知当时的指导老师，之后也是我博士期间的二导 prof. Huiyun Liu 课题组有博士名额。经过几次激烈的探讨，我做出了人生中的一个重大决定——直博。因此，我首先要感谢刘教授在几次轻松愉快的探讨之后，同意让当时的我，一个知识储备欠缺的本科生加入他的博士课题组。我愿称之为，梦开始的地方。

其次，我极其感恩年轻有为的陈思铭老师 (Dr. Siming Chen) 愿意成为我的博士生导师，并且一路坚持"不抛弃、不放弃"的精神，无数次的打捞在学海沉浮的我。从最开始激光器后工艺的摸索、器件性能的测试，到 CSC 奖学金的申请文书、面试环节的准备，以及在疫情期间实验平台的寻找与搭建,陈老师都给予了我最悉心的指导与最无私的帮助。遇良师不易，结益友更难，我万分感激与陈老师之间亦师亦友的师生关系，使我度过了受益匪浅的五年。尤其是新冠疫情爆发后的这两年半，思铭老师经过多方协调，使我有机会到武汉国家信息光电子创新中心 (NOEIC)和北京中科院物理所 (IoP) 进行实验测试与交流学习，以此保证了我在滞留中国期间仍能有科研产出，将疫情对科研进度的影响最小化。这些经历给我最大的感触便是，老师可能不是给出答案的人，但他一定会是最努力尝试解决问题的人。饮水思源，缘木思本。我再次衷心感谢陈思铭老师对我的无条件信任，精心指导与栽培，以及为我提供去各个平台锻炼的机会。

再次，我要感谢我的同门师兄弟姐妹们: UCL MBE 组的所有小伙伴们。尤其是我的师姐廖梦雅博士，她以自己的经验给予了我非常多的指导与帮助。每当遇到棘手的问题，我会第一时间咨询她，而她也会很及时的给我最中肯最可靠的意见或建议。与此同时，我要感谢来自 UCL

ONG 组的刘智鑫老师 (Dr. Zhixin Liu) 以及他的学生周子川和他的博士后 Mu-Chieh Lo. 作为我心中当之无愧的光电通信大佬，刘智鑫老师会耐心的回答我每个愚钝的问题，并在我遭遇科研瓶颈的时候提出建设性的解决方案。打个不恰当的比喻，当我与智鑫老师探讨学术问题的时候，我脑中常会浮现西游记里观音菩萨尝试点化孙悟空的画面。正因为有他的鞭策和激励，我才能在实验合作期间飞速成长，快速填补知识盲区。

高质量的科研产出离不开不同科研团队之间的相互配合，本论文中许多亮眼的成果都是通过与其他课题组、研究单位的合作实现的。因此，我想感谢荷兰 TUE 大学的 Dr. Zizeng Cao 和 Dr. Jian'ou Huang；中科院物理所的王霆博士、王子昊博士、郭明辰和杨礴；还有武汉国家信息光电子创新中心的肖希博士、傅焰峰博士、胡晓博士、张红广博士、严杰和吴定益。谢谢他们在合作期间给了我极大的帮助与支持，使我的想法与实验计划可以得到高效的落实与反馈。

我要感谢身边的朋友们对我持之以恒的鼓励。尤其是我的室友 Fungi (陈悦琪女士)和饺子妈(张亦钦女士)， 见证了我读博期间无数个灰心丧气的瞬间，不停的为我加油打气，不断地以美食和旅行宽慰我焦虑的内心，在异国他乡为我带来了如家人般的温暖陪伴。

最后，我要感谢我的家人们对我的疼爱与信任。感恩潘华敏先生与王荷飞女士愿意倾其所有的培养我，谢谢他们的努力工作，让我有底气做任何事情，在将近三十岁的日子里还能无忧无虑的追逐自己的科研梦想，当一个快乐的米虫，没有后顾之忧。

最后的最后，我还要感谢自己，在任何条件下都没有动过放弃的念头。读博是一种经历更是一场磨砺，就如游戏中的打怪升级，需要遭遇一次次挫折打击之后才能累积经验值并且成长。在这五年里，我最大的收获与感悟就是要学会与自己和解，接纳自己的不完美，调整好心态，才能面对一个又一个不期而至的挑战。

感恩所有的经历，感谢所有的相遇。

山水有来路，早晚复相逢。

祝愿我们都能平凡而不平庸!

2022 年 5 月

Table of Contents

List of Abbreviations

AC	Autocorrelator
ACPML	Anti-Colliding Pulse Mode-Locking
ASE	Amplified Spontaneous Emission
AWG	Arbitrary Waveform Generator
B2B	Back-to-Back
BER	Bit-Error Rate
CEO	Carrier-Envelope Offset
CMOS	Complementary Metal-Oxide Semiconductor
CW	Continuous Wave
DI	Deionised
DOS	Density of States
DSO	Digital Storage Oscilloscope
DSP	Digital Signal Processing
DWDM	Dense Wavelength Division Multiplexing
DWELL	Dot-in-Well
EBL	Electron Beam Lithography
EO	Electro-Optic
EOM	Electro-Optic Modulator
ES	Excited State
ESA	Electrical Spectrum Analyser
FFE	Feed-Forward Equaliser
FSO	Free-Space Optical
FSR	Free Spectral Range
FWHM	Full-Width-Half-Maximum
FWM	Four-Wave Mixing
GD	Group Delay
GDD	Group Delay Dispersion
GS	Ground State
GVD	Group Velocity Dispersion
HD-FEC	Hard-Decision Forward Error Correction
HDP	High-Density Plasma
IBL	Ion Beam Lithography
ICP	Inductively Coupled Plasma
ICPECVD	Inductively Coupled Plasma-Enhanced Chemical Vapour Deposition
ICT	Information and Communication Technologies

IPA	Isopropyl Alcohol
ISI	Inter-Symbol-Interference
LDWL	Laser Direct Writing Lithography
LiDAR	Light Detection and Ranging
MBE	Molecular Beam Epitaxy
ML	Monolayer
MLL	Mode-Looked Laser
MZM	Mach-Zehnder modulator
NLC	Nonlinear Compensation
OBPF	Optical Bandpass Filter
OFC	Optical Frequency Comb
OSA	Optical Spectrum Analyser
OSNR	Optical Signal-to-Noise Ratio
PC	Polarisation Controller
PD	Photodiode
PDFA	Praseodymium-Doped Fibre Amplifier
PECVD	Plasma-Enhanced Chemical Vapour Deposition
PL	Photoluminescence
PRBS	Pseudo-Random Bit Sequence
QCSE	Quantum-Confinement Stark Effect
QD	Quantum Dot
QW	Quantum Well
RF	Radio Frequency
RIE	Reactive-Ion Etching
RIN	Relative Intensity Noise
RMS	Root-Mean-Square
RRC	Root-Raised-Cosine
RTA	Rapid Thermal Annealing
SA	Saturable Absorber
SAGO	Space-Air-Ground-Ocean
SD-FEC	Soft-Decision Forward Eerror Correction
SHG	Second-Harmonic Generation
SK	Stranski-Krastanov
SNR	Signal-to-Noise Ratio
SRL	Strain-Reducing Layer
SSB	Single-Sideband
TBP	Time-Bandwidth Product

TEC	Thermoelectric Temperature Controller
TEM	Transmission Electron Microscopy
UTC-PD	Uni-Traveling-Carrier Photodiode
VB	Valence Band
VOA	Variable Optical Attenuator
WPE	Wall-Plug Efficiency

List of Figures

List of Tables

List of Publications

Journal Publications

[1]   **S. Pan.**, H. Zhang., Z. Liu., M. Liao., M. Tang., D. Wu., X. Hu, J. Yan., L. Wang., M. Guo., Z. Wang., T. Wang., P. M. Smowton., A. Seeds., H. Liu., X. Xiao., and S. Chen., "Multi-wavelength 128 Gbit s− 1 λ− 1 PAM4 optical transmission enabled by a 100 GHz quantum dot mode-locked optical frequency comb," *Journal of Physics D: Applied Physics,* vol. 55, no. 14, p. 144001, 2022. (***Special Issue: Emerging Leaders 2021***)

[2]   **S. Pan.**, J. Huang., Z. Zhou., Z. Liu., L. Ponnampalam., Z. Liu., M. Tang., M. Lo., Z. Cao., K. Nishi., K. Takemasa., M. Sugawara., R. Penty., I. White., A. Seeds., H. Liu., and S. Chen., "Quantum dot mode-locked frequency comb with ultra-stable 25.5 GHz spacing between 20° C and 120° C," *Photonics Research,* vol. 8, no. 12, pp. 1937-1942, 2020. (***Spotlight on Optics***)

[3]   **S. Pan.**, V. Cao., M. Liao., Y. Lu., Z. Liu., M. Tang., S. Chen., A. Seeds., and H. Liu., "Recent progress in epitaxial growth of III–V quantum-dot lasers on silicon substrate," *Journal of Semiconductors,* vol. 40, no. 10, p. 101302, 2019. (***Invited paper***)

[4]   J. Yang., Z. Liu., P. Jurczak., M. Tang., K. Li., **S. Pan.**, A. Sanchez., R. Beanland., J-C. Zhang., H. Wang., F. Liu., Z. Li., S. Shutts., P. M. Smowton., S. Chen., A. Seeds., and H. Liu., "All-MBE grown InAs/GaAs quantum dot lasers with thin Ge buffer layer on Si substrates," *Journal of Physics D: Applied Physics,* vol. 54, no. 3, p. 035103, 2020.

[5]   Z. Liu., C. Hantschmann., M. Tang., Y. Lu., J-S. Park., M. Liao., **S. Pan.**, A. Sanchez., R. Beanland., M. Martin., T. Baron., S. Chen., A. Seeds., R. Penty., I. White., and H. Liu., "Origin of defect tolerance in InAs/GaAs quantum dot lasers grown on silicon," *Journal of Lightwave Technology,* vol. 38, no. 2, pp. 240-248, 2019.

[6]   T. Zhou., M. Tang., G. Xiang., B. Xiang., S. Hark., M. Martin., T. Baron., **S. Pan.**, J-S. Park., Z. Liu., S. Chen., Z. Zhang., and H. Liu., "Continuous-wave quantum dot photonic crystal lasers grown on on-axis Si (001)," *Nature communications,* vol. 11, no. 1, pp. 1-7, 2020.

Conference Papers and Presentations

[1]   **S. Pan.**, H. Zhang., D. Wu., Z. Wang., T. Wang., A. Seeds., H. Liu., X. Xiao., and S. Chen., "O-band 100 GHz quantum dot mode-locked optical frequency comb with 128 Gbit/s/λ PAM-4 optical transmission ability," in *Asia Communications and Photonics Conference (ACP)*, 2021: Optical Society of America, p. T4D. 7. (***Postdeadline Session, Oral***)

[2]   **S. Pan.**, J. Huang., Z. Zhou., Z. Liu., L. Ponnampalam., Z. Liu., M. Tang., M-C. Lo., Z. Cao., A. Seeds., H. Liu., and S. Chen., "Ultra-stable 25.5 GHz quantum dot mode-locked frequency comb operating up to 120° C," in *Conference on Lasers and Electro-Optics (CLEO): Science and Innovations*, 2021: IEEE, p. SF2F. 3. (***Oral***)

[3]   **S. Pan.**, M. Liao., Z. Liu., Y. Lu., V. Cao., M. Tang., J-S. Park., J. Wu., S. Chen., A. Seeds., and H. Liu., "O-band InAs Quantum Dot Light Sources Monolithically Grown on Si," in *Conference on Lasers and Electro-Optics/Pacific Rim (CLEO-PR)*, 2018: Optical Society of America, p. W1F. 2. (***Invited***)

Chapter 1 Introduction

1.1 Background and Motivation

The past decade has witnessed tremendous growth and advancements in information and communication technologies (ICT) as the demand for high-speed data transmission has been continuously fuelled by new services and applications [1-3]. Despite the recent advances in ICT, the unprecedented traffic congestion in the conventional data centre promoted the development of novel high-rate and large-capacity optical transmission systems, in which signals are carried as modulation data on an optical carrier [4, 5]. In other words, replacing the traditional copper-based networks with optical interconnects is becoming inevitable [6].

Based on the existing optical communication infrastructure, there are three options to increase transmission ability: adopt advanced modulation formats, increase the data rate, and increase the number of optical carriers [7]. The first two options impose stringent requirements on signal levels and are strictly limited by the involved electrical and electro-optical components [8-10]. Therefore, increasing the number of optical carriers is more preferred for transmission capacity expansion. Currently, the well-developed dense wavelength division multiplexing (DWDM) technology has been widely used to multiplex a number of optical carriers in optical transmission systems [11, 12]. One of the key advantages of the DWDM system is the parallel transmission of separate wavelengths within a single optical fibre. Indeed, multiple wavelengths could carry different types of modulation formats simultaneously and independently at different bit-rates [13, 14]. However, DWDM systems require extremely precise wavelength control to avoid inter-channel crosstalk. The most straightforward way to create DWDM channels is to use several discrete single-wavelength lasers, each of which operates at a slightly different wavelength [13]. However, the involvement of numerous lasers makes this approach costly. Besides, careful control and close monitoring are required to avoid wavelengths drifting into the spectral region of adjacent sources over time

and temperature [15]. For this reason, replacing multiple lasers with a single multi-carrier light source in DWDM systems is particularly appealing for low-cost and power-efficient optical communication [16-18]. Such multi-carrier light sources are also known as optical frequency combs (OFCs) and can be generated by various techniques [19, 20]. Among all generation methods, the OFCs generated by mode-locked lasers (MLLs) are attractive for DWDM systems due to their small footprints and low power consumption [21, 22].

Recently, the development in material sciences has inspired the exploration of low dimensional structures, such as the quantum dot (QD) and quantum well (QW) nanostructures. Compared with their bulk and QW counterparts, the QD material owing to its inherent properties, including a broad inhomogeneous gain spectrum [23], reduced threshold current [24], ultrafast carrier dynamic [25, 26], and temperature resilience [27], is more desirable for mode-locking operation [28]. The generation of low-timing jitter, sub-picosecond pulses with repetition rates up to several tens of gigahertz (GHz) has been successfully demonstrated in QD-based MLLs [29-31]. Besides, the temperature stability of QD MLLs has also been proved by several research groups [32-34]. The maturity of the QD mode-locking technology could allow us to obtain high-performance chip-scale OFC sources, offer opportunities for future complementary metal-oxide-semiconductor (CMOS)-compatible photonic integrated circuits (PIC) technology, and potentially accelerate the transition of OFCs from research laboratory experiments to practical scenarios [35].

Based on the above views, the main objective of this thesis is to develop stable two-section QD MLLs, investigate the characteristics of QD mode-locked OFCs and verify their reliability as a multi-carrier light source in high-speed optical data transmission systems.

1.2 Optical frequency comb (OFC)

The OFC provides a direct connection between optical and microwave domains that have revolutionised many research fields, including atomic clock

distribution/recovery [36], precision measurements [37, 38], gas spectroscopy [39, 40], and optical communications [41-44]. This section will briefly explain the basics of OFCs and discuss the three most common methods for OFC generation.

1.2.1 OFC definition

An optical frequency comb (OFC) is a light source that contains a series of equivalently distributed comb lines in the frequency domain, which corresponds to consecutive optical pulses in the time domain [45]. A representation of an OFC in time and frequency domains is shown in Fig. 1.1. As can be observed, for successive pulses in the time domain, there is a dephasing ($\Delta\phi_{CEO}$) between the optical carrier and the pulse envelop, and its origin is related to the specific comb generation methods used [46]. For MLLs, it arises from the difference between the phase and group velocities in the laser cavity [46, 47]. This phase-shift induces a global carrier-envelope offset (CEO) frequency (f_{CEO}) for all modes in the frequency domain [47]:

$$f_{CEO} = f_{rep} \cdot \frac{\Delta\phi_{CEO}}{2\pi} \qquad 1.1$$

In most cases, the f_{CEO} lies between 0 and the fundamental repetition rate (f_{rep}). Therefore, the oscillation frequencies of the spectral modes are not necessarily an integer multiple of the f_{rep} and the absolute position of individual mode in an ideal OFC can be defined by the well-known comb equation [48, 49]:

$$\nu_N = N \cdot f_{rep} + f_{CEO} \qquad 1.2$$

The comb equation indicates that only two degrees of freedom (the f_{rep} and the f_{CEO}) are required to identify the absolute frequency of an optical mode [50]. While the f_{rep} can be easily accessed through a RF spectrum analyser, the f_{CEO} related to the phase information of the pulse train is extremely difficult to be directly obtained [20]. The conventional nonlinear *'f-to-2f'* interferometry method is considered as the simplest way for f_{CEO} detection, where the fundamental frequency on the low end of the optical comb spectrum (ν_N) is doubled and

heterodyned with the light at twice the frequency (ν_{2N}) [47, 51]:

$$f_{CEO} = 2 \times \nu_N - \nu_{2N} = 2 \times (N \cdot f_{rep} + f_{CEO}) - (2N \cdot f_{rep} + f_{CEO}) \qquad 1.3$$

Consequently, knowing the absolute frequency of one mode allows us to determine the absolute frequency of any other modes [20].
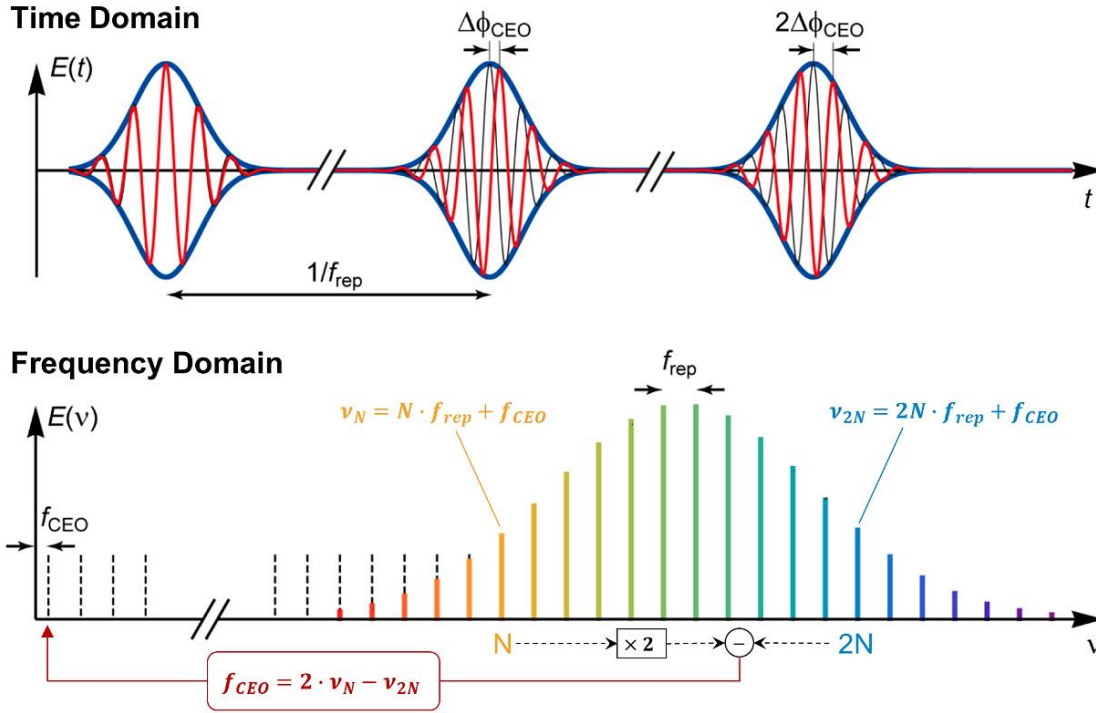
Figure 1.1 Time-domain (Top) and frequency-domain (down) representation of an optical frequency comb based on MLLs.

1.2.2 Methods of OFC generation

The last two decades have witnessed the rapid development of the OFC technology, and the OFCs have evolved into valuable tools for numerous applications [51]. The ideal characteristics of an OFC vary according to the target application, which motivates the research on assorted methods for OFC generation [52]. Three of the most popular techniques for generating an OFC, namely electro-optic (EO) modulation, Kerr microresonators, and MLLs, will be discussed below.

Electro-optic modulation

The OFCs generated with EO modulators (EOMs), also known as the EO modulation-based combs or simply the EO combs, are induced by the second-order nonlinear optical effect ($\chi^{(2)}$) [53]. Among all three approaches, the EO comb generator is the only OFC source that can offer large flexibility in the agile tuning of both central frequency and comb spacing [54, 55]. This approach involves three main components, including a continuous wave (CW) laser, one or several EOMs, and the RF signal generator. Each modulator is based on phase modulation, and additional functionalities may be acquired by adding other surrounding components (e.g., polarisers, interferometer, etc.). A summary of different setups used for EO comb generation is given in [54]. Overall, the CW signal is modulated by a sequence of discrete EOMs driven by the external RF oscillator [56-58]. The CW laser determines the central wavelength of the emerged comb while the comb spacing is defined by the RF signal generator. By cascading several EOMs and adjusting the corresponding driving conditions, a large number of comb lines can be obtained, leading to a broad bandwidth [57-59]. Besides, by selecting the appropriate EOMs and carefully controlling the RF signals and the bias voltages, a flat spectrum with a high optical signal-to-noise ratio (OSNR) can be realised [56]. However, it is undeniable that the maximum available comb spacing achieved with these setups is limited by the bandwidth of EOMs, which is typically around 40 GHz for conventional and commercial EOMs. Moreover, the large insertion loss of the modulators as well as the power-hungry high-frequency electronics involved in this method has a significant impact on cost and power consumption. Hence, despite the EO comb generators being very attractive in their flexible setting characteristics, the trade-off between the number of combs and the setup complexity must be considered during operations. As a result, the EO combs are not suitable for data transmission applications unless low-noise, high-frequency RF oscillators and low-driving-voltage high-power handling EO modulators are employed [57].

Kerr microresonators

An alternative method for comb generation is to use Kerr microresonators via the third-order nonlinear susceptibility ($\chi^{(3)}$) [60]. In general, the optical microresonators are driven by an external CW pump laser through evanescent coupling. The interaction between the pump laser and the modes of the high-Q microresonator yields efficient parametric frequency conversion based on both degenerate and non-degenerate four-wave mixing (FWM) [61-63]. Firstly, two pumped photons are annihilated and converted into a new pair of photons (the signal and the idler photons) through the degenerate FWM process, resulting in the emergence of signal and idler sidebands [44, 64]. Due to the energy conservation, the generated signal-idler sidebands are equidistant from the pump laser, but may not necessarily be mutually equidistant as required for OFC formation [60, 61]. Then, the newly emerged frequency components could serve as seeds for further parametric frequency conversion via the non-degenerate FWM process, in which all generated sidebands are equally distributed from each other [61]. When the new frequencies coincide with optical microresonator modes, the parametric process will be enhanced, leading to higher efficiency of sideband generation. One of the main advantages of this technique is the ultra-wide comb span (up to hundreds of nanometres), which results from the intrinsically broadband nature of optical parametric gain [60]. With a suitable selection of materials and proper dispersion engineering, an even broader comb generation can be expected [65, 66]. Moreover, the repetition rate of Kerr combs is ultimately limited by the effective path length of the microresonators rather than the RF oscillators and, hence, mode-spacing up to Terahertz (THz) can be obtained [19]. However, due to the complexity of the formation dynamics within the Kerr resonators, controlling the coherence of combs as well as achieving large detuning of the comb spacing remains challenging [16, 56, 67].

Mode-locked lasers

In comparison to other OFC sources, mode-locked lasers have an extensive

history dating over 60 years [68, 69]. Numerous review papers and books discuss mode-locked lasers and explain their operating principles [50, 70, 71]. Despite providing broad spectra and wide mode spacing, these OFCs do not have much tunability [72]. Overall, the term 'mode-locking' refers to the well-established phenomenon within the multimode laser operation where a periodic pulse train spaced at a period equal to the round-trip time of the laser cavity, leading to equally distributed discrete combs in the frequency domain [28, 73, 74]. Even though mode-locking has been achieved in multiple material systems through different techniques (detailed in Section 1.2), the fundamental principle behind them stays similar and will be briefly explained in this section.

In a multimode laser cavity, the phase of one mode is irrelevant to other laser modes. Thus, with no attempt to control the laser spectrum, the 'free-running' laser mode oscillates independently with its own phase [75]. Subsequently, the resulting laser output will be incoherent and fluctuate in the time domain, being similar to Fig. 1.2 (a). Despite being periodic, it would be difficult to observe the output due to its low intensity. However, by locking up the phases of all the modes to a certain degree, the multimode laser will operate as an MLL. This process can be easily understood in the time domain. As presented in Fig. 1.2 (b), the phases of all the modes are forced to have a fixed relationship to each other. In this case, an amplitude modulation resulting from the superposition of laser modes within the cavity will be employed for the output signal. As a result, those modes will radiate in phase regularly, producing a train of 'coherent spikes' [76]. One could also consider that this output pulse train arises from the dynamic competition between the gain from the laser medium and the loss created by either internal or external modulation. Ideally, within a period, a short-time window of net gain and a consistent loss for the rest of time is preferred to generate a desirable ultrashort pulse with extremely high power. Issues related to MLLs will be discussed in more detail further on in this chapter, and all the essential parameters of those mode-locked OFCs will be detailed in Section 1.3.

(a) Random Case
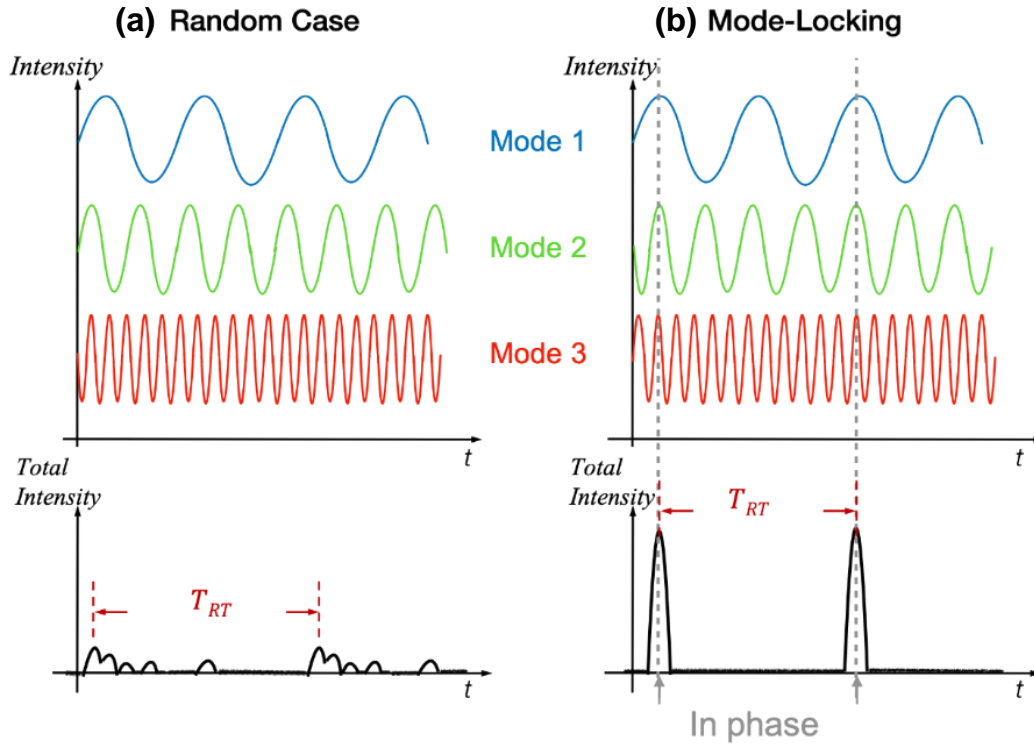
(b) Mode-Locking

Figure 1.2 Laser output in the time domain for (a) random case and (b) mode-locking case.

1.3 Mode-locking in lasers

1.3.1. Types of Mode-Locked Lasers

The mode-locking technique could be assorted by different types of lasers. In this section, the four best-known types of lasers among all laser kinds for mode-locking will be discussed. They are dye lasers, solid-state bulk lasers, fibre lasers and semiconductor lasers.

Dye lasers

At the early stage, most of the original works of ultrashort pulse generation was carried out with dye lasers [77-79]. A dye laser uses a dye cell in the form of vapor, liquid, or solid as the gain medium, which needs an optical pump source. Commonly, the emission wavelengths depend on the dye cells used, with a wide selection of dye cells, and the dye lasers can cover an unparalleled broad spectral region from ultraviolet to near-infrared spectrum (300 nm ~ 1100 nm) [80]. Dye

lasers with broad gain bandwidth are favoured candidates not only for wavelength tuneable applications but also for generating ultrashort pulses. However, this type of laser generally needs an expensive external optical pumping. Moreover, mixtures of dyes and solvents tend to undergo chemical degradation over time. This means that the dye solutions are supposed to be exchanged every tens or hundreds of operation hours. Also, additional precautions are needed when handling dye lasers since most of the dye solutions are poisonous and even carcinogenic. For these reasons, dye lasers are diminishingly used and gradually replaced by solid-state lasers in the field of ultrafast pulse generation once they are sufficiently developed.

Solid-state lasers

The term solid-state lasers refer to optically-pumped lasers with ion-doped solid gain materials (usually in crystal or glass form) [80]. Ever since the first demonstration of the ruby laser in 1960 [81], tremendous progress has been observed in using solid-state lasers to generate ultrafast pulses [82], and thus they are currently the dominant type of mode-locked lasers. There are various solid-state lasers due to the diversity of gain materials and the numerous dopant ions. In this section, the solid-state lasers will be divided more specifically into solid-state bulk lasers and fibre lasers according to the form of gain media.

Solid-state bulk lasers

Solid-state bulk lasers are made with bulk host materials that are doped with either rare-earth ions or transition metal ions. The most common solid-state laser used today is the neodymium-doped yttrium aluminium garnet (Nd: YAG) laser, while others, such as the ruby laser and the titanium-doped sapphire (Ti: sapphire) laser, are continuously used in certain applications. As the beam propagates freely in a non-processed (bulk) area, the beam radius is primarily determined by the design of laser resonators rather than by the gain medium. Normally, the operation wavelength of solid-state lasers can range from red to near-infrared spectrum (600

nm ~ 1000 nm). However, employing the non-linear wavelength conversion technique allows extending the emission wavelength in the visible and even the ultraviolet spectrum [83, 84]. The optical pump sources, which strongly impact on laser characteristics, are undoubtedly essential to solid-state bulk laser systems. When choosing a pump source, the trade-off between its cost and the beam quality should always be kept in mind. For example, the lamp-pumped sources are relatively cheap while the power efficiency is low and strong thermal effects might degrade beam quality. On the contrary, the diode-pumped sources with higher power efficiency could provide superior beam quality, but the price could be very high. Besides, solid-state bulk lasers are comprised of at least a pump source, a solid gain medium, lenses, output couplers, mirrors, and a cooling system, which limits an ultra-compact integration because of their large footprint. Although the construction is relatively simple, highly skilled users are always needed to optimize the alignments in these multi-element systems.

Fibre lasers

Once the bulk host material is fabricated into a light-guiding optical fibre, a special kind of solid-state laser called fibre laser is formed. The fibre lasers are normally treated separately from the bulk solid-state lasers because of their unique waveguide structures in the gain medium, where a doped optical fibre is employed as the resonant cavity. Although fibre lasers are relatively new to the market, they have achieved remarkable growth in recent years. It is widely believed that fibre lasers will eventually replace most of bulk lasers since they could reach the same or better performance at a potentially lower cost. As mentioned above, the conventional bulk solid-state lasers require critical alignments between optical components, which means that they are sensitive to movements. Fibre lasers, on the other hand, are immune to this drawback since the generated laser beams are very stable inside the fibres. Meanwhile, the fibre optic core could shield the propagating light from the environment, maintain the focused beam size, and ensure an extremely high-quality output beam. Furthermore, the fibre lasers show higher wall-plug efficiency than that bulk lasers, so less power will be lost in the

form of heat energy. Thanks to the long and thin fibre geometries, heat dissipation will be evenly distributed along the length of the fibre, which means that the thermal effects could be negligible in most fibre lasers [85]. However, such fibre geometry is also the source of the main limitation. The long propagation length and small effective mode area will bring inevitable nonlinear effects, significantly restricting achievable pulse duration or peak power [86, 87]. In addition, the twist dependence of polarization characteristics should always be considered when dealing with fibre lasers [88]. Therefore, despite the various benefits of fibre, they still face challenges in specific operation regimes at the same time.

Semiconductor lasers

Currently, semiconductor lasers present one of the most compact and efficient laser sources. They are comprised of a large group of binary, ternary, and quaternary elements from Group III–V of the periodic table. The two major commercial families of semiconductor lasers are those grown on InP and GaAs substrates. Although semiconductor materials are solid objects, semiconductor lasers are normally classified separately from solid-state lasers mainly due to their unique mechanisms of pumping and lasing [89]. Almost all semiconductor lasers are qualitatively the same and could be treated as the electrically pumped p-n junction. When forward-biased, a condition of population inversion is reached. The recombination of electrons and holes releases photons in the form of light with energy roughly equal to the bandgap energy of the gain material. Such direct conversion of electricity to light brings out a higher wall-plug efficiency than other optically pumped lasers [90]. The emission wavelength of semiconductor lasers is mainly determined by the choices of materials, dopants, and layer thickness. With band structure engineering, the operating wavelength could be further refined from 0.4 μm (GaN) to 20 μm (lead salt). Moreover, instead of using mirrors, the optical feedback in the laser cavity is achieved by cleaved-facets which are perfectly parallel to each other [91]. Such a simple construction could bring us compact, lightweight, and easy-operation light sources.

Undeniably, semiconductor lasers may not suit many general laser applications due to their limited output power and great beam divergence. There are still dozens of ongoing research in this area, mainly due to their ability for potential monolithic integration with Silicon substrate and their capability for future CMOS compatible integration [92]. In 2016, our group demonstrated the very first electrically-pumped Si-based QD semiconductor laser working at room temperature [93]. Subsequently, the UCSB research group announced highly reliable Si-based semiconductor lasers, offering up to 87% efficiency and working over one million hours [94]. Those astonishing findings inspire intensive research into certain applications, especially for those applications in Silicon photonics. In addition, the semiconductor mode-locked lasers could easily accomplish picosecond (ps) or femtosecond (fs) pulse trains with a multi-gigahertz (GHz) fundamental repetition rate. This property is indispensable in optical communications. In addition, the semiconductor mode-locked lasers could easily accomplish picosecond (ps) or femtosecond (fs) pulse trains with a multi-gigahertz (GHz) fundamental repetition rate. This property is important for applications in high-speed optical communications.

1.3.2 Mode-locking techniques

In general, the most common design for semiconductor MLLs is a multi-section Fabry-Perot (FP) cavity with cleaved mirror facets. The electrical isolation between the segments allows for different operating regimes along the laser cavity. By considering whether an external modulator is involved in achieving phase locking in the laser cavity, the mode-locking techniques could be classified into three types: active, passive and hybrid. These mode-locking techniques will be discussed in more detail below, and the main features of each technique are summarised in Table 1.1.

Active mode-locking

Active mode-locking is achieved by periodically modulating the resonator gain/loss with an external RF signal at a frequency synchronised with the cavity longitudinal

mode spacing (f_{rep}). As shown in Fig. 1.4 (a), the modulation is normally applied to the injection current (I_i), resulting in a well-defined time window at each round-trip. The width of this window is mainly determined by the external electrical signal and the laser dynamic, which will ultimately determine the output pulse duration [82]. In principle, only the circulating pulse that experiences a net round-trip gain (i.e., gain > loss) can survive within the resonator, while the intracavity radiation that undergoes a negative round-trip gain (i.e., gain < loss) will continuously diminish until it disappeared. With a highly stable driving source, the active mode-locking provides the lowest pulse-to-pulse timing jitter (< 0.5 ps) among all three techniques [95, 96]. However, it has been proved that neither ultra-short pulse durations nor high repetition rates can be easily obtained in an actively MLL due to the restrictions of suitable high-frequency RF oscillators, available impedance matching circuitry, and ideal laser design with minimum parasitic capacitance, and applicable high-speed packages [97]. For these reasons, pulse shaping mechanism dominated by saturable absorption is more preferred for applications where particularly short pulses or high repetition rates are required.

Passive mode-locking

Unlike the active mode-locking, passive mode-locking benefits from the nonlinear dynamics of the intracavity saturable absorber (SA) and, it does not require external modulation during pulse generation [28, 98]. The SA can be considered as a lossy element whose transmission ability is enhanced with increasing light intensity [99]. The typical biasing condition for a passively MLL is presented in Fig. 1.4 (b), where a reverse voltage source (V_{rev}) is applied to the SA region while the gain section is injected with a forward current source (I_i). The working principle of the passively MLL is schematically presented in Fig. 1.3. When I_i above the threshold current (I_{th}) is applied, an optical waveform will propagate within the resonator cavity, with experiencing an amplification in the gain section and suffering an attenuation in the SA section. The light absorption in the SA section, due to the band filling mechanism, decreases nonlinearly until the absorber section reaches a temporary condition called self-induced transparency or 'bleach' for a

short time interval [100, 101]. Before recovery takes place, this positive feedback tends to cause a sudden rise in light intensity (i.e., pulse formation) in the SA region [102]. Immediately, the inverted-carrier population in the gain section will be depleted with the pulse propagation, resulting in a temporary gain saturation. The relative dynamic of SA and gain saturation intrinsically governs the pulse shaping mechanism in the passive MLL. Several round trips are usually required to obtain a stable pulse train emission due to the self-starting nature of the passive mode-locking. Detailed discussions of conditions for achieving passive mode-locking will be covered in Section 1.2.3. Considering that the passively MLLs are free from running oscillators with no high-stable driving source involved in the pulse shaping process, they have the highest timing jitter levels (~ 100 ps).
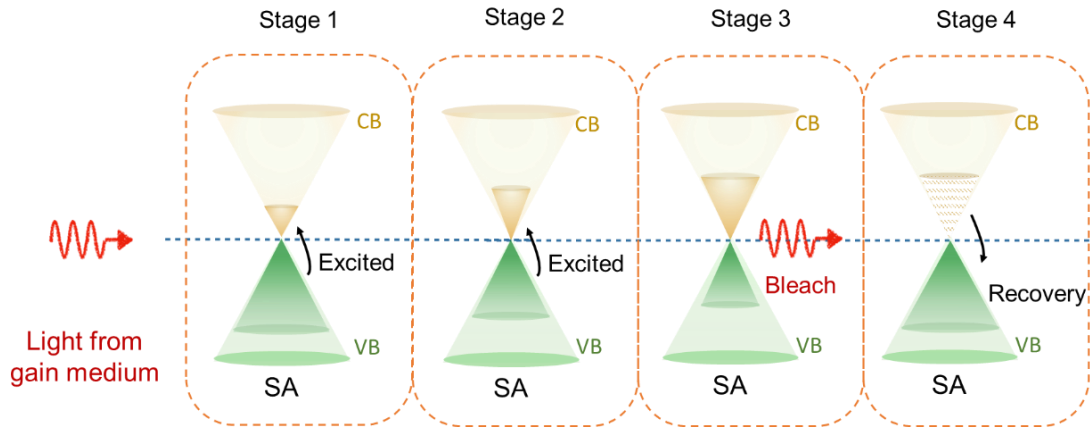
Figure 1.3 Schematic of carrier dynamic within the SA section.

Hybrid mode-locking

The hybrid mode-locking combines both active and passive mode-locking techniques, where an external RF modulation signal is applied to either gain or SA section to stabilise the generated pulse train [28]. Hence, it allows us to take advantage of the strong pulse-shortening effect in passive mode-locking while preserving the low timing jitter associated with active mode-locking. In addition, the f_{rep} tuning on the order of few tens of MHz is enabled with modulation signal to compensate a certain degree of the frequency error resulting from the uncertainty of device cleaving [103, 104]. The most common biasing condition for a hybrid MLL

is shown in Fig. 1.4 (c). As can be seen, the V_{rev} applied to the SA section is modulated with a frequency synchronised to the T_{RT} of the laser cavity [105]. Despite the inherent advantages mentioned above, the hybrid mode-locking is to some extent similar to the active mode-locking that is stringently limited by the electrical RF drive signal, particularly the extremely short devices with ultra-high f_{rep} [106]. To this end, the passive mode-locking technique is more favoured for a higher repetition rate (e.g., f_{rep} > 20 GHz) [107].
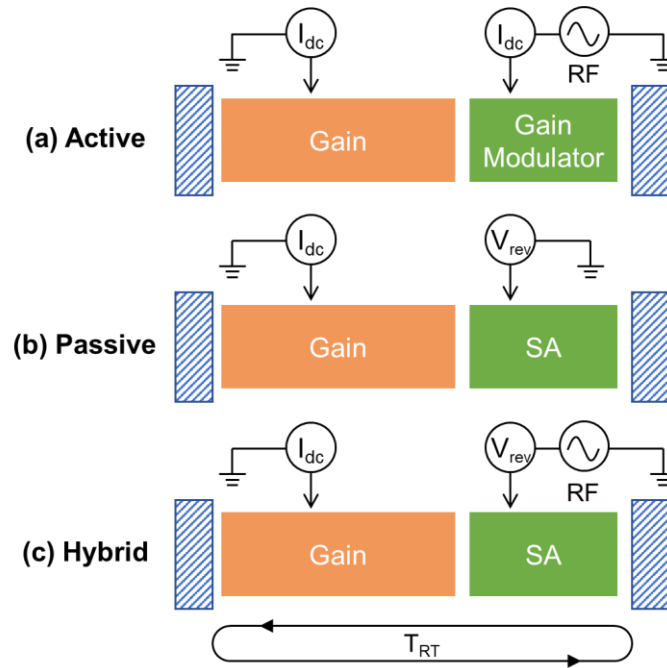
Figure 1.4 Typical biasing condition for (a) active mode-locking, (b) passive mode-locking, and (c) hybrid mode-locking.

Table 1.1 Comparison of active, passive and hybrid mode-locking techniques.

Features	Active	Passive	Hybrid
τ_p	Longest	Shortest	Relatively short
f_{rep}	Up to tens of GHz	Up to THz	Up to tens of GHz
Timing jitter	Lowest (< 0.5 ps)	Highest (~ 100 ps)	Relatively low
Tunability of f_{rep}	Flexible	Ridged	Flexible

External driving signal	Required	Not required	Required
Stability	Strong	Weak	Relatively strong
Construction	Complex	Simple	Relatively complex
Cost	High	Low	High

1.3.3 Conditions for passive mode-locking

This research mainly focuses on the high-repetition-rate MLL generated by the passive mode-locking, whose pulse shaping process is dominated by the SA section. Hence, a good understanding of the mutual interference between the gain and SA regions is essential to figure out the working principle behind those laser devices and thus optimise their performance. Therefore, this section briefly reviews the saturation dynamics in both gain and SA sections and highlights the crucial conditions for achieving passive mode-locking.
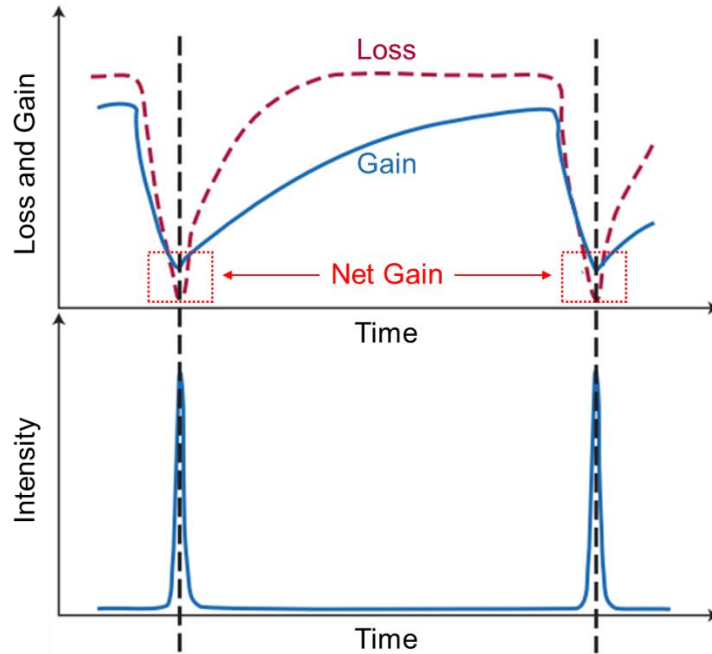
Figure 1.5 The gain and loss dynamics for passive mode-locking.

Figure 1.5 illustrates the time-dependent gain and loss dynamics during passive mode-locking operation in a QD-MLL. As shown, the unsaturated loss level is

initially higher than the unsaturated gain level [28]. The propagation of the travelling wave inside the cavity will gradually saturate the SA region until it becomes transparent, i.e., the loss level reaches the minimum point. When the light saturation in the SA section is faster than that in the gain section, a well-defined temporal window of net amplification occurs. Soon after, the SA section recovers immediately from the saturated state to the original high loss state. Then, the net gain window closes, and the pulse formation completes. The width of this window is governed by the interplay between the SA absorption and gain saturation, which will ultimately determine the τ_p [99, 108]. As can be noticed, both leading edges and the trailing edges of the optical pulses experience greater attenuation than the high-intensity peaks at each round-trip. As a result, the generated pulses will undergo a continuous reshape within the laser cavity till the steady state is eventually reached after a certain transient time [70]. We can therefore conclude that the carrier lifetime (τ) in the SA and gain regions and the mutual interference of the saturation energy (E_{sat}) between those two sections are the two prerequisites for pulse generation in passive MLLs.

Carrier lifetime

As already mentioned, the τ_p is intrinsically decided by the relative dynamics of the gain and loss sections. In the same time interval, the SA section must recover faster than the gain medium to obtain very short pulses. At the same time, the gain saturation and recovery must be slower to avoid any potential amplifications happening between two consecutive pulses [109]. Since the recovery times are predominantly determined by the carrier lifetimes, the $\tau_a < \tau_g$ should be obeyed all the time [98], where τ_a and τ_g are the carrier lifetimes in the SA and gain sections, respectively. In practical, a high V_{rev} is usually applied to the SA section to solidify this relationship and ensure short-pulse generation.

Saturation energy

For stable passive mode-locking emission, the saturation energy of the SA region

(E_{sat}^a) should always be smaller than that of the gain section (E_{sat}^g) [29, 110]. That is, for a given pulse energy, the absorber must saturate faster than the gain medium. The energy saturation energies of these two sections are defined as [29, 98, 111]:

$$E_{sat}^g = \frac{hvA}{\Gamma \dfrac{dg}{dn}} \qquad\qquad 1.4$$

$$E_{sat}^a = \frac{hvA}{\Gamma \dfrac{d\alpha}{dn}} \qquad\qquad 1.5$$

where hv is the photon energy, A is the optical modal gain, Γ is the optical confinement factor, dg/dn and $d\alpha/dn$ are the material differential gain and loss, respectively.

This condition can be better explained in conjunction with Fig. 1.6, in which the profile of differential gain/loss against carrier density in QD materials is exhibited. In general, the semiconductor materials have limited DoS, and, therefore, the rate of change in gain/loss decreases continuously with increasing carrier density. As can be easily observed, the differential loss in the absorption region is always greater than the differential gain in the gain region ($d\alpha/dn > dg/dn$). Assuming that the A and the Γ remain constant for both two regions, from the Equation 1.4 and 1.5, we can deduce that larger saturation energy is expected in the gain section than in the absorber regime (i.e., $E_{sat}^a < E_{sat}^g$) [29]. To fulfil this condition, in practice, the SA region is normally applied by reverse bias, while the gain section is usually injected under forwarding bias.

Unfortunately, there is a trade-off between the above two conditions. With a higher level of V_{rev}, a faster τ_a can be attained through more efficient carrier extraction, which allows us to strengthen the pulse-shortening mechanism. However, it also induces a larger cavity loss, resulting in a higher I_{th} of the laser device. Additionally, an increase in E_{sat}^a might occur due to the bandgap detuning caused by the

electric-field induced quantum-confinement stark effect (QCSE) [102]. On the other hand, an enhanced I_i could boost the E_{sat}^g, but at the same time, it may lead to a faster τ_g and result in unwanted pulse-broadening mechanism. Consequently, it is rather challenging to simultaneously optimise both $\tau_a < \tau_g$ and $E_{sat}^a < E_{sat}^g$ for best mode-locking performance. Therefore, stable passive mode-locking can only be achieved through a delicate balance between competing phenomena in both SA and gain sections, leading to a limited driving range for ideal short and intense pulse formations [112].
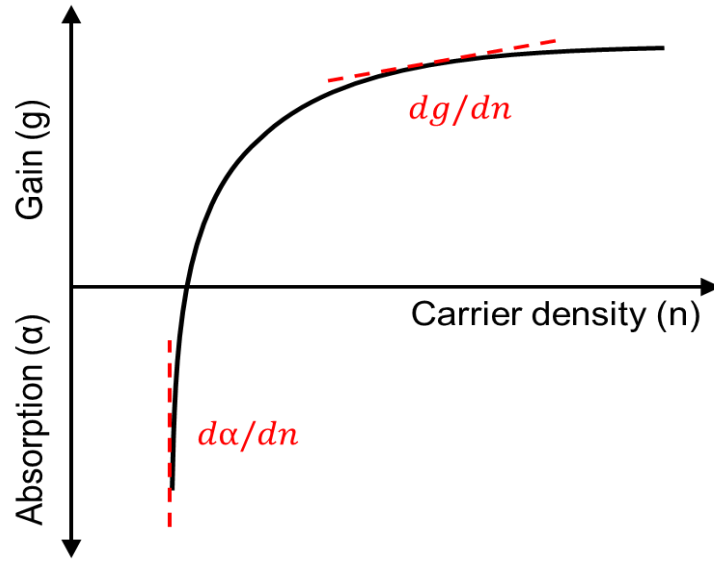
Figure 1.6 Schematic representation of the gain and absorption versus carrier density for QD materials [29, 97].

1.4 Parameters for mode-locked OFCs

The mode-locked OFCs in this project is aimed at optical data transmission in the telecommunication sector. Hence, a number of unique requirements on the comb parameters related to this application field should be concerned, such as the fundamental repetition rate, emission spectra, power per comb, OSNR, pulse duration and timing jitter. Instead of elaborating on the characterisation techniques (which are covered in section 2.3), this section specifies the physical meaning of the main characteristics and discusses how those parameters might limit the

transmission ability of a given comb source. Understanding those constrictions could motivate device design and discussions in the following chapters.

1.4.1 Fundamental repetition rate

The fundamental repetition rate (f_{rep}) of a passively MLL is also known as the tone spacing or the free spectral range (FSR) of the laser device. It corresponds to the time taken for light to make an exactly one-round trip of the laser cavity L and is given by:

$$f_{rep} = \frac{c}{2nL}$$ 1.6

where c is the vacuum speed of light and n is the refractive index of the active region.

For OFC-based WDM transmission systems, the f_{rep} is expected to comply with the ITU-T Rec. G.694.1 spectral grids, i.e., located within the range of 12.5 GHz to 200 GHz [13, 49]. The OFC sources with a higher f_{rep} are normally less susceptible to the interference beating between adjacent combs, hence, can potentially minimise the influence of wavelength drift of laser devices in DWDM networks [113, 114]. Besides, the large mode-spacing of the OFCs allows individual tones to be separated more easily by available optical filters, which brings extra benefits in practical applications. On the other hand, a lower f_{rep} leads to denser OFCs, which increases the difficulties in filter out comb lines for individual data modulations. Furthermore, the f_{rep} directly determines the highest symbol rate at which a tone can be modulated [115]. Therefore, the OFCs with lower f_{rep} require more comb lines to achieve the same bit rate compared to the higher f_{rep} cases.

1.4.2 Centre wavelength and spectral width

For practical applications, the multi-wavelength OFC source should be compatible with the existing telecommunication infrastructure based on standard silica fibres,

i.e., optical communication in either telecom O-band at 1.3 μm (with low chromatic dispersion) or telecom C-band at 1.55 μm (with the minimum attenuation) [116, 117]. Although the conventional telecom C-band is still the most commonly used in reality, increasing attention has been paid to telecom O-band to fulfilling the transmission capacity of the current photonic networks. As a key parameter, the centre wavelength (λ_{centre}) of semiconductor laser is determined by the band gap of the active material [118]:

$$\lambda_{centre} = \frac{hc}{E_g}$$ 1.7

where h is the Planck constant, c is the vacuum speed of light and E_g is the energy gap in eV. Theoretically, with suitable material choice and proper band-gap engineering, the fabricated MLLs could be tailored to specific wavelengths for target applications.

The spectral width (3dB bandwidth or full width at half maximum (FWHM)) of the emission spectrum ($\Delta\lambda_{BW}$) is another important characteristic of mode-locked OFCs, which can be expressed as:

$$\Delta\lambda_{BW} = \lambda_2 - \lambda_1 = \frac{c}{f_2} - \frac{c}{f_1} = \frac{c}{f_1 f_2} \cdot \Delta f_{BW}$$ 1.8

where λ_1 and λ_2 are the lower and upper half-power points, repectively. The value of $\Delta\lambda'_{3dB}$ is mostly affected by the homogeneous broadening and inhomogeneous broadening of the gain medium [119, 120]: Though the homogeneous broadening may influence the shape of the emission spectrum, in our case, the inhomogeneous broadening mechanism is dominant, and thus, the influence of homogeneous broadening is negligible [121]. It has been proved that with simple Fourier analysis, the achievable pulse duration is inversely proportional to the $\Delta\lambda_{BW}$ [122]. Typically, large inhomogeneous broadening leads to a broad gain bandwidth, corresponding to a relative short τ_p. Furthermore, a broad $\Delta\lambda_{BW}$ is particularly desired for data transmission purposes as it enables a large number of

comb lines for parallel data transmission, which can directly affect the aggregate transmission capacity of the laser device [123-125].

1.4.3 Power and OSNR

The power and noise levels for OFCs impose a significant impact on transmission performance. The ratio between those two levels in a given bandwidth (normally is 0.1 nm) is defined as the OSNR, which constrains the modulation format options [126, 127]. High output power is always desired in optical transmission for eliminating the usage of optical amplifiers, which will add extra amplified spontaneous emission (ASE) noise and degrade the OSNR level. Furthermore, assuming that the 3-dB bandwidth of the emission spectra remains the same, the average power per comb is believed to decrease with the number of channels due to the gain saturation [128]. That is, if the output powers of all MLLs were in the same order, a higher power per comb will be achieved with a larger f_{rep} since the total output power is spread over fewer assumed modes.

It should be mentioned that the average power per comb received after optical transmission needs to be above a certain level for useful data analysis. To determine such a lower limit for the power per comb, it is critical to consider several factors, including the modulation format, the medium for light propagation, the transmission distance, and the receiver sensitivity.

1.4.4 Pulse duration and TBP

As mentioned in previous sections, the laser pulse generated through mode-locking mechanism contains a series of frequency components that travel independently within the cavity. The associated spectral phase can be treated as a smooth function which can be expressed using a Taylor series expansion around an angular frequency ω_o [109, 129]:

$$\varphi(\omega) = \varphi_0 + \frac{\varphi_1}{1!}(\omega - \omega_0) + \frac{\varphi_2}{2!}(\omega - \omega_0)^2 + \frac{\varphi_3}{3!}(\omega - \omega_0)^3 + \cdots \qquad 1.9$$

where the φ_1 and φ_2 are the group delay (GD) and the group delay dispersion

(GDD), respectively:

$$GD = \varphi_1 = \frac{d\varphi(\omega)}{d\omega} \qquad 1.10$$

$$GDD = \varphi_2 = \frac{d^2\varphi(\omega)}{d\omega^2} \qquad 1.11$$

In general, the GDD describes the wavelength dependency of the GD in a given length of a dispersive medium. The GDD per unit length is known as the group velocity dispersion (GVD) [130]:

$$GVD = \frac{GDD}{L} \qquad 1.12$$

If the value of GDD equalled to 0, the GD was constant for all frequency components and the pulse profile could be maintained during light propagation. On the other hand, a non-zero GDD means that each wavelength travels at different speeds within the resonator, resulting in pulse broadening in the time domain [131]. Therefore, it is extremely important to have a low GDD over the operational bandwidth for ultrashort pulse generation [132]. The pulses generated by passive MLLs are typically in the sub-picosecond range, making it unrealistic to directly detect the optical signal with a conventional photodiode (PD), whose bandwidth is limited to 100 GHz. For this reason, the intensity autocorrelator (AC) based on second-harmonic generation (SHG) is widely used to provide a fairly good estimation of pulse characterisation. Detailed information on AC technique and how it derives the τ_p is referred in section 2.3.2. It is important to note that the τ_p can only be obtained by assuming a specific waveform of the generated pulse. The two most commonly used waveforms are Gaussian and hyperbolic secant squared (sech^2), and each wave shape has its own deconvolution factor as listed in Table 1.2 [133]. Inappropriate assumptions may result in large differences between the calculation results and the actual values [134].

The time-bandwidth product (TBP) is another figure-of-merit, indicating the quality

of the generated pulse and can be expressed as [135]:

$$TBP = \tau_p \cdot \Delta f_{BW} \qquad\qquad 1.13$$

Even though the TBP value could vary from case to case, there will be a minimum level for the certain pulse profile. In the other words, the achievable τ_p for a given optical spectrum always has a lower limit that leads to the maximum pulse peak intensity, and the attained pulse from this limit is called the Fourier-transform-limited pulse or transform-limited pulse [109]. Due to the non-zero GDD, the actual TBP obtained is often larger than the theoretical minimum value. The difference between measured and ideal TBP allows us to deduce how much the generated pulse can potentially be compressed [136].

Table 1.2 The deconvolution factors and the minimum TBP values for different pulse profiles.

Pulse profile	Deconvolution Factor (τ_p/τ_{AC})	Fourier-transform-limited TBP
Gaussian	0.707	0.441
Sech²	0.648	0.325

1.4.5 Timing jitter

Timing jitter, another significant factor in almost all communication systems, is defined as the deviation of the instant pulse positions from their ideal location in the time domain [137]. The time fluctuations ($\Delta t(t)$) can be expressed as followed:

$$\Delta t(t) = t_p(t) - t_{p0}(t) \qquad\qquad 1.14$$

where t_p is the temporal position of the pulse and t_{p0} is the nominal position determined by the f_{rep}. Commonly, the phase noise and timing jitter are related to each other and can be utilised interchangeably [138, 139]. Hence, the term $\Delta t(t)$ can be converted into equivalent phase variations ($\phi(t)$) in radiance by employing the following equation:

$$\phi(t) = 2\pi f_{rep} \Delta t(t) \qquad\qquad 1.15$$

The timing jitter (σ_j) can then be quantified in terms of the $\phi(t)$ [140]:

$$\sigma_j^2 = \langle |\phi(t)|^2 \rangle \qquad\qquad 1.16$$

The root-mean-square (RMS) of the timing jitter ($\sigma_{j,RMS}$) can be computed as [141, 142]:

$$\sigma_{j,RMS\_\infty} = \sqrt{\int_{-\infty}^{\infty} S_{\phi(f)} \, df} \qquad\qquad 1.17$$

where $S_{\phi(f)}$ is the phase noise spectral density. The phase noise spectral density can be further expressed in terms of the single sideband (SSB) phase noise ($L_{(f)}$), which can be directly measured by an RF spectrum analyser [143]:

$$L_{(f)} = \frac{S_{\phi(f)}}{2} \qquad\qquad 1.18$$

In practical, the timing jitter is often obtained over a certain frequency interval $[f_i, f_x]$ rather than an infinite amount of time. Thus, the $\sigma_{j,RMS}$ can be written as:

$$\sigma_{j,RMS} \ (radians) = \sqrt{2 \int_{f_i}^{f_x} L_{(f)} \, df} \qquad\qquad 1.19$$

$$\sigma_{j,RMS} \ (seconds) = \frac{\sqrt{2 \int_{f_i}^{f_x} L_{(f)} \, df}}{2\pi f_{rep}} \qquad\qquad 1.20$$

Low timing jitter is necessary to reduce transmission errors and accomplish good optical communication. It is believed that the random fluctuations in the gain and refractive index are the major sources of timing jitter [28, 98]. To stabilise those fluctuations and thereby obtain an ultra-low level of σ_j (~ fs), an optical feedback loop is usually implemented [144, 145].

1.5 Advantages of QDs

Based on the discussions in sections 1.2 and 1.3, this section will explain in detail the unique advantages of QD materials over their bulk or QW counterparts.

Since the first successful demonstration of double heterostructure lasers in 1970, researchers have gradually realised that carrier confinement is necessary for achieving efficient lasing [146]. The growing interests in quantum-confined materials have promoted the development of semiconductor lasers worldwide. By reducing the dimensionality of the active region, 1-D confined QW structure, and 3-D confined QD structure can be achieved. The dimensionality here refers to the number of directions in which the electronic carriers could move freely [147]. Figure 1.7 presents the density of states (DOS) as a function of energy in bulk (3D), QW (2D) and QD (0D) structures. As can be noted, the QD structure features a delta-function-like DOS that can effectively confine carriers in discrete energy levels. Moreover, it has been proved that QD material exhibits a number of inherent optical properties owing to such a low-dimensional nanostructure [148, 149], including low threshold current [149, 150], broad emission spectrum [23], improved temperature stability [27, 32, 151, 152], ultrafast carrier dynamics [25], and large ratio of saturation energies in the gain and SA sections [29]. These advantages make the QD structure an appealing candidate for stable OFC generation and will be further described below.
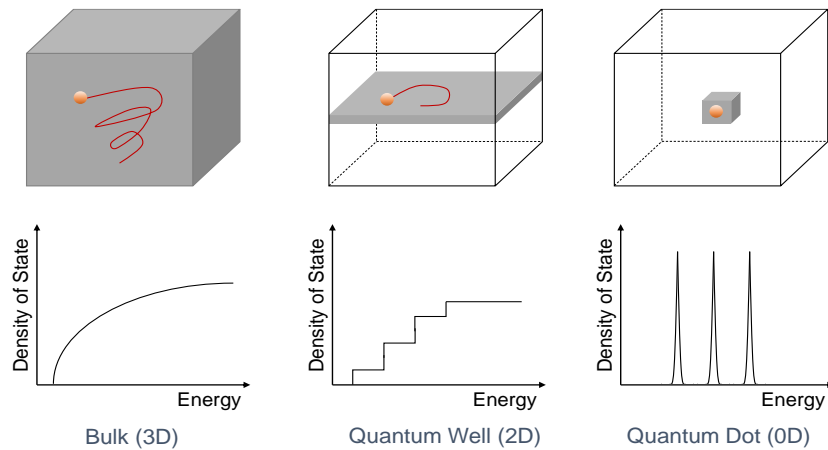
Figure 1.7 Schematic diagram of density of states in bulk, quantum well and quantum dot structures.

Low threshold current

The first advantage of using QDs as an active medium in laser devices is the low threshold current. As already mentioned, QDs are zero-dimension (0D) nanoparticles, in which the carriers are confined in all 3 dimensions. The overall active region volume of the QD structure is much smaller than that of the conventional bulk or QW structures [153]. Because of the strong carrier confinement and the limited energy states, the carriers are spread over a small energy range and rapidly filled into working energy states, which leads to a high probability of radiative recombination [150, 154]. As a result, fewer injection carriers are required for achieving population inversion, and thereby, lasing at a low threshold current could be obtained. In addition, for QD MLLs, the mode-locking behaviour normally occurs near the threshold current, where the carriers contributing to non-stimulated emission are reduced. Therefore, the level of amplified spontaneous emission (ASE) within the cavity is low [155-157]. Laser devices with low power consumption and low ASE are always favoured for real-life applications, especially in the optical communication field.

Broad emission spectrum

Although the theoretical model predicted excellent uniformity in ideal self-assembled QDs, in reality, inhomogeneous broadening arising from the size variation is inevitable [27, 158, 159]. In general, QDs can only undergo stimulated emission at a certain energy level that is determined by their geometric size. Thus, the individual QD can be treated as an uncorrelated emission source from other QDs, leading to a broad emission spectrum that is particularly beneficial for MLLs in optical communication systems [160]. Sub-picosecond pulses corresponding to an optical spectrum of 14 nm have been successfully demonstrated in two-section InAs/GaAs QD MLLs [161]. According to Fourier transform analysis, a broader optical spectrum could potentially produce shorter optical pulses [28, 162]. Hence, the researchers believe that sub-100 fs pulses could be achieved with a broader gain spectrum in simple QD MLL configurations [28].

Improved temperature stability

Compared with other bulk or QW materials, QD lasers with improved temperature characteristics could enable stable high-temperature operations and open a new market for cost-effective applications [149]. The superior temperature stability of QD lasers is mainly attributed to the enhanced energy separations between the ground state (GS) and the first excited state (ES1), which effectively prevents carriers from escaping out of the GS at elevated temperatures [163-165]. Otherwise, the carrier leakage will result in a decrease of QD gain for the same injection current, which in turn leads to an unexpected increment in the threshold current density [163, 166]. The temperature-independent QD lasers are realised by a well-known technological breakthrough that implements p-type doping during the QDs growth [167-169]. The key of this technique is to introduce a permanent population of holes into QDs, compensating the hole thermal spreading across the closely spaced energy states in the valence band (VB) [170]. Consequently, the degradation of device performance at high working temperatures can be avoided. Our group has developed a stable QD MLL operating up to 120°C (detailed in Chapter 4), and the results of this work suggest that QD MLLs could be employed as uncooled OFC sources for data transmission [32].

Ultrafast carrier dynamics

QD structure also benefits from the ultrafast carrier dynamics owing to its low dimensionality [171]. The fast carrier capture and relaxation in QDs result in ultrafast gain/absorption recovery processes, which has been widely proved [25, 101, 172, 173]. And this property makes passive QD MLLs particularly attractive for short pulse generation, as the pulse duration is primarily determined by their absorber recovery times. Besides, it has been experimentally demonstrated that the recovery time can be further reduced by applying a reverse field to the SA section (e.g., from 62 ps with V_{rev} = 0 V to ~ 700 fs with V_{rev} = −10 V) [101]. Hence, the ultrafast gain and absorber dynamics associated with QD material are ideal for passive mode-locking operation.

Saturation energy

The large ratio of the gain to SA section saturation energies adds extra benefit to QD MLLs. As depicted in Fig. 1.8, for any structure of semiconductor materials, the differential gain is generally higher in the absorption regime than in the gain regime as the modal gain spectra tend to flatten out with increasing carrier density, which is a consequence of the limited density of available states [29]. Therefore, less energy is required to saturate the reverse-biased absorber section as compared to the forward-biased gain section [98]. This phenomenon is more prominent in QD material owing to its discrete nature of DOS. As stated before, the pulse shaping mechanism within the two-section MLLs is governed by the ratio of saturation energies in the gain and SA sections, which correspond to the pulse-broadening and pulse-shortening mechanisms, respectively. With careful balance, QD MLLs could take advantage of a low E_{sat}^a to enhance the pulse shortening effect while simultaneously benefiting from a high E_{sat}^g to facilitate the formation of high peak power pulses [174-176]. These factors make QD materials prime candidates for stable pulse generation.
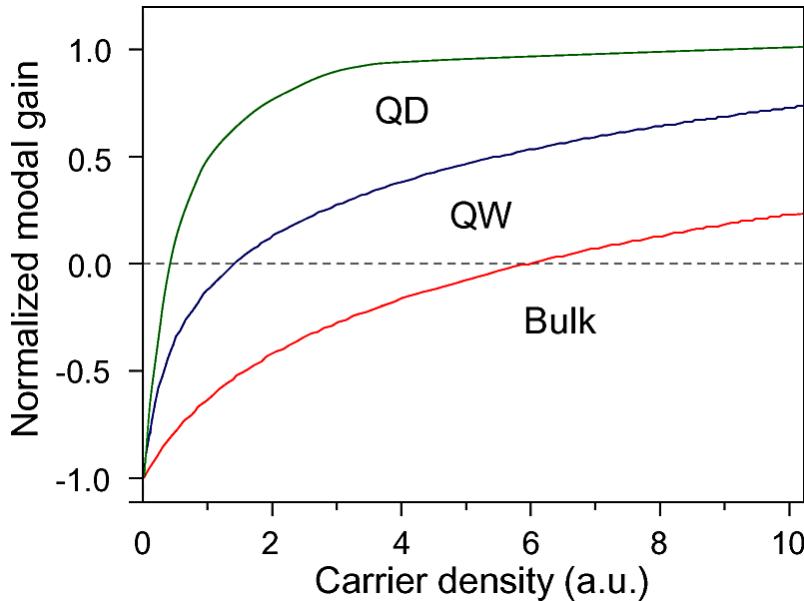
Figure 1.8 Normalised modal gain versus carrier density for bulk (red), quantum well (blue) and quantum dot (green) materials [29].

1.6 Reference

[1]   V. N. I. Cisco, "The zettabyte era: Trends and analysis (2017)," ed: White Paper Cisco Public San Jose, CA, USA, 2017.

[2]   C. V. N. I. Cisco, "Forecast and Methodology 2013-2018, 2014," *Cited on,* p. 23.

[3]   B. Corcoran *et al.*, "Ultra-dense optical data transmission over standard fibre with a single chip source," *Nature Communications,* vol. 11, no. 1, pp. 1-7, 2020.

[4]   H. Kaushal and G. Kaddoum, "Optical communication in space: Challenges and mitigation techniques," *IEEE communications surveys & tutorials,* vol. 19, no. 1, pp. 57-96, 2016.

[5]   M. Chen, S. Mao, Y. Zhang, and V. C. Leung, *Big data: related technologies, challenges and future prospects*. Springer, 2014.

[6]   P. Green, "Progress in optical networking," *IEEE Communications magazine,* vol. 39, no. 1, pp. 54-61, 2001.

[7]   E. Agrell *et al.*, "Roadmap of optical communications," *Journal of Optics,* vol. 18, no. 6, p. 063002, 2016.

[8]   R. A. Linke and A. H. Gnauck, "High-capacity coherent lightwave systems," *Journal of Lightwave Technology,* vol. 6, no. 11, pp. 1750-1769, 1988.

[9]   J. Geyer *et al.*, "Practical implementation of higher order modulation beyond 16-QAM," in *2015 Optical Fiber Communications Conference and Exhibition (OFC)*, 2015: IEEE, pp. 1-3.

[10]   R.-J. Essiambre, G. Kramer, P. J. Winzer, G. J. Foschini, and B. Goebel, "Capacity limits of optical fiber networks," *Journal of Lightwave Technology,* vol. 28, no. 4, pp. 662-701, 2010.

[11]   G. Yan, Z. Ruixia, D. Weifing, and C. Xiaorong, "Point-to-point DWDM system design and simulation," in *Proceedings. The 2009 International Symposium on Information Processing (ISIP 2009)*, 2009: Citeseer, p. 90.

[12]   Q. Cheng, M. Bahadori, M. Glick, S. Rumley, and K. Bergman, "Recent advances in optical technologies for data centers: a review," *Optica,* vol. 5, no. 11, pp. 1354-1370, 2018.

[13]   R. Antil, S. B. Pinki, and S. Beniwal, "An overview of DWDM technology & network," *Int. J. Sci. Technol. Res,* vol. 1, no. 11, pp. 43-46, 2012.

[14]   J.-P. Laude, *DWDM fundamentals, components, and applications*. Artech House Norwood, MA, 2002.

[15]   G. E. Keiser, "A review of WDM technology and applications," *Optical Fiber Technology,* vol. 5, no. 1, pp. 3-39, 1999.

[16]   M. Imran, P. M. Anandarajah, A. Kaszubowska-Anandarajah, N. Sambo, and L. Potí, "A survey of optical carrier generation techniques for terabit capacity elastic optical networks," *IEEE Communications Surveys & Tutorials,* vol. 20, no. 1, pp. 211-263, 2017.

[17]   M. Koshiba, "Wavelength division multiplexing and demultiplexing with photonic crystal waveguide couplers," *journal of lightwave technology,* vol. 19, no. 12, p. 1970, 2001.

[18]   B. J. Chun, S. Hyun, S. Kim, S.-W. Kim, and Y.-J. Kim, "Frequency-comb-referenced multi-channel fiber laser for DWDM communication," *Optics Express,* vol. 21, no. 24, pp. 29179-29185, 2013.

[19]   L. Chang, S. Liu, and J. E. Bowers, "Integrated optical frequency comb technologies," *Nature Photonics,* vol. 16, no. 2, pp. 95-108, 2022/02/01 2022, doi: 10.1038/s41566-021-00945-1.

[20]   T. Fortier and E. Baumann, "20 years of developments in optical frequency comb technology and applications," *Communications Physics,* vol. 2, no. 1, pp. 1-16, 2019.

[21]   S. A. Diddams, K. Vahala, and T. Udem, "Optical frequency combs: Coherently uniting the electromagnetic spectrum," *Science,* vol. 369, no. 6501, p. eaay3676, 2020.

[22]   F. Grillot, W. W. Chow, B. Dong, S. Ding, H. Huang, and J. Bowers, "Multimode Physics in the Mode Locking of Semiconductor Quantum Dot Lasers," *Applied Sciences,* vol. 12, no. 7, p. 3504, 2022.

[23]   J. C. Norman *et al.*, "A review of high-performance quantum dot lasers on silicon," *Ieee J Quantum Elect,* vol. 55, no. 2, pp. 1-11, 2019.

[24]   A. Stintz, G. Liu, H. Li, L. Lester, and K. Malloy, "Low-threshold current density 1.3-μm InAs quantum-dot lasers with the dots-in-a-well (DWELL) structure," *Ieee Photonic Tech L,* vol. 12, no. 6, pp. 591-593, 2000.

[25]   P. Borri, S. Schneider, W. Langbein, and D. Bimberg, "Ultrafast carrier dynamics in InGaAs quantum dot materials and devices," *Journal of Optics A: Pure and Applied Optics,* vol. 8, no. 4, p. S33, 2006.

[26]   V. Klimov, P. H. Bolivar, and H. Kurz, "Ultrafast carrier dynamics in semiconductor quantum dots," *Physical review B,* vol. 53, no. 3, p. 1463, 1996.

[27]   Y. Arakawa and H. Sakaki, "Multidimensional quantum well laser and temperature dependence of its threshold current," *Appl Phys Lett,* vol. 40, no. 11, pp. 939-941, 1982.

[28]   E. U. Rafailov, M. A. Cataluna, and W. Sibbett, "Mode-locked quantum-dot lasers," *Nature photonics,* vol. 1, no. 7, pp. 395-401, 2007.

[29]   M. G. Thompson, A. R. Rae, M. Xia, R. V. Penty, and I. H. White, "InGaAs quantum-dot mode-locked laser diodes," *IEEE Journal of Selected Topics in Quantum Electronics,* vol. 15, no. 3, pp. 661-672, 2009.

[30]   S. Pan *et al.*, "Multi-wavelength 128 Gbit s$-$ 1 $\lambda-$ 1 PAM4 optical transmission enabled by a 100 GHz quantum dot mode-locked optical frequency comb," *Journal of Physics D: Applied Physics,* vol. 55, no. 14, p. 144001, 2022.

[31]   D. I. Nikitichev *et al.*, "High peak power and sub-picosecond Fourier-limited pulse generation from passively mode-locked monolithic two-section gain-guided tapered InGaAs quantum-dot lasers," *Laser Physics,* vol. 22, no. 4, pp. 715-724, 2012.

[32]   S. Pan *et al.*, "Quantum dot mode-locked frequency comb with ultra-stable 25.5 GHz spacing between 20° C and 120° C," *Photonics Research,* vol. 8, no. 12, pp. 1937-1942, 2020.

[33]   J. K. Mee, M. T. Crowley, R. Raghunathan, D. Murrell, and L. F. Lester, "Characteristics of Passively Mode-Locked Quantum Dot Lasers from 20 to 120 degrees C," (in English), *Physics and Simulation of Optoelectronic Devices Xxi,* vol. 8619, 2013, doi: Artn 86190b 10.1117/12.2004567.

[34]   M. A. Cataluna, E. U. Rafailov, A. McRobbie, W. Sibbett, D. A. Livshits, and A. Kovsh, "Stable mode-locked operation up to 80/spl deg/C from an InGaAs quantum-dot laser," *Ieee Photonic Tech L,* vol. 18, no. 14, pp. 1500-1502, 2006.

[35]   J. C. Norman, D. Jung, Y. Wan, and J. E. Bowers, "Perspective: The future of quantum dot photonic integrated circuits," *APL photonics,* vol. 3, no. 3, p. 030901, 2018.

[36]   B. Bloom *et al.*, "An optical lattice clock with accuracy and stability at the 10$-$ 18 level," *Nature,* vol. 506, no. 7486, pp. 71-75, 2014.

[37]   K. Minoshima and H. Matsumoto, "High-accuracy measurement of 240-m distance in an optical tunnel by use of a compact femtosecond laser," *Applied Optics,* vol. 39, no. 30, pp. 5512-5517, 2000.

[38]   J. L. Hall, "Nobel Lecture: Defining and measuring optical frequencies," *Reviews of modern physics,* vol. 78, no. 4, p. 1279, 2006.

[39]   J. Hodgkinson and R. P. Tatam, "Optical gas sensing: a review," *Measurement Science and Technology,* vol. 24, no. 1, p. 012004, 2012.

[40]   L. Nugent-Glandorf, F. R. Giorgetta, and S. A. Diddams, "Open-air, broad-bandwidth trace gas sensing with a mid-infrared optical frequency comb," *Applied Physics B,* vol. 119, no. 2, pp. 327-338, 2015.

[41]   P. J. Delfyett *et al.*, "Optical frequency combs from semiconductor lasers and applications in ultrawideband signal processing and communications," *Journal of Lightwave Technology,* vol. 24, no. 7, p. 2701, 2006.

[42]   L. Lundberg *et al.*, "Phase-coherent lightwave communications with frequency combs," *Nature communications,* vol. 11, no. 1, pp. 1-7, 2020.

[43]   P. Marin-Palomo *et al.*, "Microresonator-based solitons for massively parallel coherent optical communications," *Nature,* vol. 546, no. 7657, pp. 274-279, 2017.

[44]   J. Pfeifle *et al.*, "Coherent terabit communications with microresonator Kerr frequency combs," *Nature photonics,* vol. 8, no. 5, pp. 375-380, 2014.

[45]   Y. Jun, H. Schnatz, and L. W. Hollberg, "Optical frequency combs: from frequency metrology to optical phase control," *IEEE Journal of Selected Topics in Quantum Electronics,* vol. 9, no. 4, pp. 1041-1058, 2003, doi: 10.1109/JSTQE.2003.819109.

[46]   D. J. Jones *et al.*, "Carrier-Envelope Phase Control of Femtosecond Mode-Locked Lasers and Direct Optical Frequency Synthesis," *Science,* vol. 288, no. 5466, pp. 635-639, 2000, doi: doi:10.1126/science.288.5466.635.

[47]   H. R. Telle, G. Steinmeyer, A. E. Dunlop, J. Stenger, D. H. Sutter, and U. Keller, "Carrier-envelope offset phase control: A novel concept for absolute optical frequency measurement and ultrashort pulse generation," *Applied Physics B,* vol. 69, no. 4, pp. 327-332, 1999/10/01 1999, doi: 10.1007/s003400050813.

[48]   T. W. Hänsch, "Nobel Lecture: Passion for precision," *Reviews of Modern Physics,* vol. 78, no. 4, pp. 1297-1309, 11/17/ 2006, doi: 10.1103/RevModPhys.78.1297.

[49]   L. Lundberg *et al.*, "Frequency comb-based WDM transmission systems enabling joint signal processing," *Applied Sciences,* vol. 8, no. 5, p. 718, 2018.

[50]   J. Ye and S. T. Cundiff, *Femtosecond optical frequency comb: principle, operation and applications*. Springer Science & Business Media, 2005.

[51]   S. A. Diddams, "The evolving optical frequency comb," *JOSA B,* vol. 27, no. 11, pp. B51-B62, 2010.

[52]   N. R. Newbury, "Searching for applications with a fine-tooth comb," *Nature photonics,* vol. 5, no. 4, pp. 186-188, 2011.

[53]   M. Zhang *et al.*, "Broadband electro-optic frequency comb generation in a lithium niobate microring resonator," *Nature,* vol. 568, no. 7752, pp. 373-377, 2019.

[54]   A. Parriaux, K. Hammani, and G. Millot, "Electro-optic frequency combs," *Adv. Opt. Photon.,* vol. 12, no. 1, pp. 223-287, 2020/03/31 2020, doi: 10.1364/AOP.382052.

[55] A. Rueda, F. Sedlmeir, M. Kumari, G. Leuchs, and H. G. L. Schwefel, "Resonant electro-optic frequency comb," *Nature,* vol. 568, no. 7752, pp. 378-381, 2019/04/01 2019, doi: 10.1038/s41586-019-1110-x.

[56] H. Sun, M. Khalil, Z. Wang, and L. R. Chen, "Recent progress in integrated electro-optic frequency comb generation," *Journal of Semiconductors,* vol. 42, no. 4, p. 041301, 2021.

[57] V. Torres-Company and A. M. Weiner, "Optical frequency comb technology for ultra-broadband radio-frequency photonics," *Laser & Photonics Reviews,* vol. 8, no. 3, pp. 368-393, 2014.

[58] A. J. Metcalf, V. Torres-Company, D. E. Leaird, and A. M. Weiner, "High-power broadly tunable electrooptic frequency comb generator," *IEEE Journal of Selected Topics in Quantum Electronics,* vol. 19, no. 6, pp. 231-236, 2013.

[59] R. Wu, V. Supradeepa, C. M. Long, D. E. Leaird, and A. M. Weiner, "Generation of very flat optical frequency combs from continuous-wave lasers using cascaded intensity and phase modulators driven by tailored radio frequency waveforms," *Opt Lett,* vol. 35, no. 19, pp. 3234-3236, 2010.

[60] P. Del'Haye, A. Schliesser, O. Arcizet, T. Wilken, R. Holzwarth, and T. J. Kippenberg, "Optical frequency comb generation from a monolithic microresonator," *Nature,* vol. 450, no. 7173, pp. 1214-1217, 2007.

[61] T. J. Kippenberg, R. Holzwarth, and S. A. Diddams, "Microresonator-based optical frequency combs," *science,* vol. 332, no. 6029, pp. 555-559, 2011.

[62] T. Kippenberg, S. Spillane, and K. Vahala, "Kerr-nonlinearity optical parametric oscillation in an ultrahigh-Q toroid microcavity," *Physical review letters,* vol. 93, no. 8, p. 083904, 2004.

[63] D. Armani, T. Kippenberg, S. Spillane, and K. Vahala, "Ultra-high-Q toroid microcavity on a chip," *Nature,* vol. 421, no. 6926, pp. 925-928, 2003.

[64] W. Liang *et al.*, "High spectral purity Kerr frequency comb radio frequency photonic oscillator," *Nature communications,* vol. 6, no. 1, pp. 1-8, 2015.

[65] K. Luke, Y. Okawachi, M. R. Lamont, A. L. Gaeta, and M. Lipson, "Broadband mid-infrared frequency comb generation in a Si 3 N 4 microresonator," *Opt Lett,* vol. 40, no. 21, pp. 4823-4826, 2015.

[66] L. Chang *et al.*, "Ultra-efficient frequency comb generation in AlGaAs-on-insulator microresonators," *Nature communications,* vol. 11, no. 1, pp. 1-8, 2020.

[67] A. Pasquazi *et al.*, "Micro-combs: A novel generation of optical sources," *Physics Reports,* vol. 729, pp. 1-81, 2018.

[68] H. W. Mocker and R. Collins, "Mode competition and self-locking effects in aq-switched ruby laser," *Appl Phys Lett,* vol. 7, no. 10, pp. 270-273, 1965.

[69] A. DeMaria, D. Stetser, and H. Heynau, "Self mode-locking of lasers with saturable absorbers," *Appl Phys Lett,* vol. 8, no. 7, pp. 174-176, 1966.

[70] H. A. Haus, "Mode-locking of lasers," *IEEE Journal of Selected Topics in Quantum Electronics,* vol. 6, no. 6, pp. 1173-1185, 2000.

[71] W. Sibbett, A. Lagatsky, and C. Brown, "The development and application of femtosecond laser systems," *Optics Express,* vol. 20, no. 7, pp. 6989-7001, 2012.

[72] X. Yan, X. Zou, W. Pan, L. Yan, and J. Azaña, "Fully digital programmable optical frequency comb generation and application," *Opt Lett,* vol. 43, no. 2, pp. 283-286, 2018.

[73] Y. Nomura *et al.*, "Mode locking in Fabry-Perot semiconductor lasers," *Physical Review A,* vol. 65, no. 4, p. 043807, 2002.

[74] A. Sobiesierski and P. M. Smowton, "6.09 - Quantum-Dot Lasers: Physics and Applications," in *Comprehensive Semiconductor Science and Technology*, P. Bhattacharya, R. Fornari, and H. Kamimura Eds. Amsterdam: Elsevier, 2011, pp. 353-384.

[75] G. Laufer, *Introduction to optics and lasers in engineering*. Cambridge University Press, 1996.

[76] P. French, "The generation of ultrashort laser pulses," *Reports on Progress in Physics,* vol. 58, no. 2, p. 169, 1995.

[77] C. Shank and E. Ippen, "Subpicosecond kilowatt pulses from a mode-locked cw dye laser," *Appl Phys Lett,* vol. 24, no. 8, pp. 373-375, 1974.

[78] R. Fork, B. Greene, and C. V. Shank, "Generation of optical pulses shorter than 0.1 psec by colliding pulse mode locking," *Appl Phys Lett,* vol. 38, no. 9, pp. 671-672, 1981.

[79] J. Valdmanis, R. L. Fork, and J. P. Gordon, "Generation of optical pulses as short as 27 femtoseconds directly from a laser balancing self-phase modulation, group-velocity dispersion, saturable absorption, and saturable gain," *Opt Lett,* vol. 10, no. 3, pp. 131-133, 1985.

[80] H. Abramczyk, *Introduction to laser spectroscopy*. Elsevier, 2005.

[81] T. H. Maiman, "Stimulated optical radiation in ruby," 1960.

[82] U. Keller, "Ultrafast solid-state lasers," *Progress in Optics,* vol. 46, pp. 1-116, 2004.

[83] P. Černý, H. Jelínková, P. G. Zverev, and T. T. Basiev, "Solid state lasers with Raman frequency conversion," *Prog Quant Electron,* vol. 28, no. 2, pp. 113-143, 2004.

[84] A. Sennaroglu, *Solid-state lasers and applications*. CRC press, 2017.

[85] M. Eilchi and P. Parvin, "Heat generation and removal in fiber lasers," *Fiber Laser,* pp. 321-344, 2016.

[86] Y. Jaouën, G. Canat, S. Grot, and S. Bordais, "Power limitation induced by nonlinear effects in pulsed high-power fiber amplifiers," *Comptes Rendus Physique,* vol. 7, no. 2, pp. 163-169, 2006.

[87] C. Jauregui, J. Limpert, and A. Tünnermann, "High-power fibre lasers," *Nature photonics,* vol. 7, no. 11, pp. 861-867, 2013.

[88] H. Y. Kim, E. H. Lee, and B. Y. Kim, "Polarization properties of fiber lasers with twist-induced circular birefringence," *Applied optics,* vol. 36, no. 27, pp. 6764-6769, 1997.

[89] O. Svelto, "Solid-State, Dye, and Semiconductor Lasers," in *Principles of Lasers*: Springer, 1998, pp. 365-418.

[90] A. Knigge *et al.*, "Passively cooled 940 nm laser bars with 73% wall-plug efficiency at 70 W and 25/spl deg/C," *Electron Lett,* vol. 41, no. 5, pp. 250-251, 2005.

[91] T. D. Germann, "Semiconductor laser concepts," in *Design and Realization of Novel GaAs Based Laser Concepts*: Springer, 2012, pp. 5-15.

[92] D. Liang and J. E. Bowers, "Recent progress in lasers on silicon," *Nature photonics,* vol. 4, no. 8, pp. 511-517, 2010.

[93] S. Chen *et al.*, "Electrically pumped continuous-wave III–V quantum dot lasers on silicon," *Nature Photonics,* vol. 10, no. 5, pp. 307-311, 2016.

[94] D. Jung *et al.*, "Highly reliable low-threshold InAs quantum dot lasers on on-axis (001) Si with 87% injection efficiency," *ACS photonics,* vol. 5, no. 3, pp. 1094-1100, 2017.

[95] D. J. Derickson, P. Morton, J. Bowers, and R. Thornton, "Comparison of timing jitter in external and monolithic cavity mode-locked semiconductor lasers," *Appl Phys Lett,* vol. 59, no. 26, pp. 3372-3374, 1991.

[96] D. R. Hjelme and A. R. Mickelson, "Theory of timing jitter in actively mode-locked lasers," *Ieee J Quantum Elect,* vol. 28, no. 6, pp. 1594-1606, 1992.

[97] P. Vasil'Ev, "Ultrashort pulse generation in diode lasers," *Optical and quantum electronics,* vol. 24, no. 8, pp. 801-824, 1992.

[98] D. J. Derickson, R. J. Helkey, A. Mar, J. R. Karin, J. G. Wasserbauer, and J. E. Bowers, "Short pulse generation using multisegment mode-locked semiconductor lasers," *Ieee J Quantum Elect,* vol. 28, no. 10, pp. 2186-2202, 1992.

[99]   E. P. Ippen, "Principles of passive mode locking," *Applied Physics B,* vol. 58, no. 3, pp. 159-170, 1994.

[100]   R. N. Zitter, "Saturated optical absorption through band filling in semiconductors," *Appl Phys Lett,* vol. 14, no. 2, pp. 73-74, 1969.

[101]   D. Malins, A. Gomez-Iglesias, S. White, W. Sibbett, A. Miller, and E. Rafailov, "Ultrafast electroabsorption dynamics in an InAs quantum dot saturable absorber at 1.3 μ m," *Appl Phys Lett,* vol. 89, no. 17, p. 171111, 2006.

[102]   X. Huang *et al.*, "Bistable operation of a two-section 1.3/spl mu/m InAs quantum dot laser-absorption saturation and the quantum confined Stark effect," *Ieee J Quantum Elect,* vol. 37, no. 3, pp. 414-417, 2001.

[103]   I. Ogura, H. Kurita, T. Sasaki, and H. Yokoyama, "Precise operation-frequency control of monolithic mode-locked laser diodes for high-speed optical communication and all-optical signal processing," *Optical and Quantum Electronics,* vol. 33, no. 7, pp. 709-725, 2001.

[104]   M. Tahvili, L. Du, M. Heck, R. Nötzel, M. Smit, and E. Bente, "Dual-wavelength passive and hybrid mode-locking of 3, 4.5 and 10 GHz InAs/InP (100) quantum dot lasers," *Optics express,* vol. 20, no. 7, pp. 8117-8135, 2012.

[105]   R. Arkhipov *et al.*, "Hybrid Mode Locking in Semiconductor Lasers: Simulations, Analysis, and Experiments," (in English), *Ieee Journal of Selected Topics in Quantum Electronics,* vol. 19, no. 4, Jul-Aug 2013, doi: 10.1109/Jstqe.2012.2228633.

[106]   C. Calo, "Quantum dot based mode locked lasers for optical frequency combs," Institut National des Télécommunications, 2014.

[107]   A. Mar, *High power mode-locked semiconductor lasers*. University of California, Santa Barbara, 1994.

[108]   G. Tandoi, "Monolithic high power mode locked GaAs/AlGaAs quantum well lasers," University of Glasgow, 2011.

[109]   R. Rosales, "InAs/InP quantum dash mode locked lasers for optical communications," Evry, Institut national des télécommunications, 2012.

[110]   H. A. Haus, "Modelocking of semiconductor laser diodes," *Japanese Journal of Applied Physics,* vol. 20, no. 6, p. 1007, 1981.

[111]   L. Shi, Y. Chen, B. Xu, Z. Wang, Y. Jiao, and Z. Wang, "Status and trends of short pulse generation using mode-locked lasers based on advanced quantum-dot active media," *Journal of Physics D: Applied Physics,* vol. 40, no. 18, p. R307, 2007.

[112]   P. Stolarz *et al.*, "Spectral dynamical behavior in passively mode-locked semiconductor lasers," *Ieee Photonics J,* vol. 3, no. 6, pp. 1067-1082, 2011.

[113] E. Connolly, F. Smyth, A. Mishra, A. Kaszubowska-Anandarajah, and L. P. Barry, "Cross-channel interference due to wavelength drift of tunable lasers in DWDM networks," *Ieee Photonic Tech L,* vol. 19, no. 8, pp. 616-618, 2007.

[114] R. Tripathi, R. Gangwar, and N. Singh, "Reduction of crosstalk in wavelength division multiplexed fiber optic communication systems," *Progress In Electromagnetics Research,* vol. 77, pp. 367-378, 2007.

[115] H. Hu *et al.*, "Single-source chip-based frequency comb enabling extreme parallel data transmission," *Nature Photonics,* vol. 12, no. 8, pp. 469-473, 2018.

[116] P. J. Winzer, D. T. Neilson, and A. R. Chraplyvy, "Fiber-optic transmission and networking: the previous 20 and the next 20 years [Invited]," *Optics Express,* vol. 26, no. 18, pp. 24190-24239, 2018/09/03 2018, doi: 10.1364/OE.26.024190.

[117] H. J. Dutton, *Understanding optical communications*. Prentice Hall PTR New Jersey, 1998.

[118] G. P. Agrawal and N. K. Dutta, *Semiconductor lasers*. Springer Science & Business Media, 2013.

[119] M. Sugawara *et al.*, "Modeling room-temperature lasing spectra of 1.3-μm self-assembled InAs∕GaAs quantum-dot lasers: Homogeneous broadening of optical gain under current injection," *Journal of Applied Physics,* vol. 97, no. 4, p. 043523, 2005.

[120] A. P. Alivisatos, A. Harris, N. Levinos, M. Steigerwald, and L. Brus, "Electronic states of semiconductor clusters: Homogeneous and inhomogeneous broadening of the optical spectrum," *The Journal of Chemical Physics,* vol. 89, no. 7, pp. 4001-4011, 1988.

[121] M. Sugawara, K. Mukai, Y. Nakata, H. Ishikawa, and A. Sakamoto, "Effect of homogeneous broadening of optical gain on lasing spectra in self-assembled In x Ga 1− x A s/G a A s quantum dot lasers," *Physical Review B,* vol. 61, no. 11, p. 7595, 2000.

[122] U. Keller, "Recent developments in compact ultrafast lasers," *nature,* vol. 424, no. 6950, pp. 831-838, 2003.

[123] G. Liu *et al.*, "Passively mode-locked quantum dash laser with an aggregate 5.376 Tbit/s PAM-4 transmission capacity," *Optics express,* vol. 28, no. 4, pp. 4587-4593, 2020.

[124] G. Liu *et al.*, "InAs/InP quantum dot mode-locked laser with an aggregate 12.544 Tbit/s transmission capacity," *Optics Express,* vol. 30, no. 3, pp. 3205-3214, 2022/01/31 2022, doi: 10.1364/OE.441820.

[125] S. T. Liu *et al.*, "High-channel-count 20 GHz passively mode-locked quantum dot laser directly grown on Si with 4.1 Tbit/s transmission capacity," (in English), *Optica,* vol. 6, no. 2, pp. 128-134, Feb 20 2019, doi: 10.1364/Optica.6.000128.

[126]   W. Freude *et al.*, "Quality metrics for optical signals: Eye diagram, Q-factor, OSNR, EVM and BER," in *2012 14th International Conference on Transparent Optical Networks (ICTON)*, 2012: IEEE, pp. 1-4.

[127]   J. Pfeifle, *Terabit-rate transmission using optical frequency comb sources*. KIT Scientific Publishing, 2017.

[128]   H. Hu and L. K. Oxenløwe, "Chip-based optical frequency combs for high-capacity optical communications," *Nanophotonics,* vol. 10, no. 5, pp. 1367-1385, 2021.

[129]   R. G. Ungureanu, G. V. Cojocaru, R. A. Banici, and D. Ursescu, "Phase measurement in long chirped pulses with spectral phase jumps," *Optics Express,* vol. 22, no. 13, pp. 15918-15923, 2014.

[130]   J. D. Pickering, *Ultrafast Lasers and Optics for Experimentalists*. IOP Publishing, 2021.

[131]   G. Chauvel, "Dispersion in optical fibers," *Anritsu Corporation,* vol. 1, 2008.

[132]   F. Wang *et al.*, "Short terahertz pulse generation from a dispersion compensated modelocked semiconductor laser," *Laser & Photonics Reviews,* vol. 11, no. 4, p. 1700013, 2017.

[133]   M. Nakazawa, T. Hirooka, P. Ruan, and P. Guan, "Ultrahigh-speed "orthogonal" TDM transmission with an optical Nyquist pulse train," *Optics express,* vol. 20, no. 2, pp. 1129-1140, 2012.

[134]   T. F. Carruthers and I. N. Duling, "10-GHz, 1.3-ps erbium fiber laser employing soliton pulse shortening," *Opt Lett,* vol. 21, no. 23, pp. 1927-1929, 1996.

[135]   P. Lazaridis, G. Debarge, and P. Gallion, "Time–bandwidth product of chirped sech 2 pulses: application to phase–amplitude-coupling factor measurement," *Opt Lett,* vol. 20, no. 10, pp. 1160-1162, 1995.

[136]   T. Inoue and S. Namiki, "Pulse compression techniques using highly nonlinear fibers," *Laser & Photonics Reviews,* vol. 2, no. 1-2, pp. 83-99, 2008.

[137]   T. C. Weigandt, *Low-phase-noise, low-timing-jitter design techniques for delay cell based VCOs and frequency synthesizers*. University of California, Berkeley, 1998.

[138]   R. Poore, "Phase noise and jitter," *Agilent EEs of EDA,* 2001.

[139]   R. Cerda, "Sources of phase noise and jitter in oscillators," *Crystek Crystals Corporation,* 2006.

[140]   M. J. Rodwell, D. M. Bloom, and K. J. Weingarten, "Subpicosecond laser timing stabilization," *Ieee J Quantum Elect,* vol. 25, no. 4, pp. 817-827, 1989.

[141] W. Kester, "Converting oscillator phase noise to time jitter," *Tutorial MT-008, Analog Devices,* p. 2009, 2009.

[142] N. Da Dalt and A. Sheikholeslami, *Understanding Jitter and Phase Noise: A Circuits and Systems Perspective*. Cambridge University Press, 2018.

[143] W. P. Robins, *Phase noise in signal sources: theory and applications*. IET, 1984.

[144] D. Arsenijevic, M. Kleinert, and D. Bimberg, "Phase noise and jitter reduction by optical feedback on passively mode-locked quantum-dot lasers," (in English), *Appl Phys Lett,* vol. 103, no. 23, Dec 2 2013, doi: Artn 231101
10.1063/1.4837716.

[145] O. Solgaard and K. Y. Lau, "Optical feedback stabilization of the intensity oscillations in ultrahigh-frequency passively modelocked monolithic quantum-well lasers," *Ieee Photonic Tech L,* vol. 5, no. 11, pp. 1264-1267, 1993.

[146] Z. I. Alferov, "Nobel Lecture: The double heterostructure concept and its applications in physics, electronics, and technology," *Reviews of modern physics,* vol. 73, no. 3, p. 767, 2001.

[147] T. J. Bukowski and J. H. Simmons, "Quantum dot research: current state and future prospects," *Critical Reviews in Solid State and Material Sciences,* vol. 27, no. 3-4, pp. 119-142, 2002.

[148] O. Svelto and D. C. Hanna, *Principles of lasers*. Springer, 1998.

[149] K. Nishi, K. Takemasa, M. Sugawara, and Y. Arakawa, "Development of quantum dot lasers for data-com and silicon photonics applications," *IEEE Journal of Selected Topics in Quantum Electronics,* vol. 23, no. 6, pp. 1-7, 2017.

[150] M. Asada, Y. Miyamoto, and Y. Suematsu, "Gain and the threshold of three-dimensional quantum-box lasers," *Ieee J Quantum Elect,* vol. 22, no. 9, pp. 1915-1921, 1986.

[151] T. Kageyama *et al.*, "Extremely high temperature (220 C) continuous-wave operation of 1300-nm-range quantum-dot lasers," in *The European Conference on Lasers and Electro-Optics*, 2011: Optical Society of America, p. PDA_1.

[152] J. K. Mee *et al.*, "110 degrees C Operation of Monolithic Quantum Dot passively Mode-Locked Lasers," (in English), *2012 23rd Ieee International Semiconductor Laser Conference (Islc),* pp. 68-+, 2012. [Online]. Available: <Go to ISI>://WOS:000316820100035.

[153] Z.-z. Sun, D. Ding, Q. Gong, W. Zhou, B. Xu, and Z.-G. Wang, "Quantum-dot superluminescent diode: A proposal for an ultra-wide output spectrum," *Optical and quantum Electronics,* vol. 31, no. 12, pp. 1235-1246, 1999.

[154] J. Wu, S. Chen, A. Seeds, and H. Liu, "Quantum dot optoelectronic devices: lasers, photodetectors and solar cells," *Journal of Physics D: Applied Physics,* vol. 48, no. 36, p. 363001, 2015.

[155] X. Huang, A. Stintz, H. Li, L. Lester, J. Cheng, and K. Malloy, "Passive mode-locking in 1.3 μm two-section InAs quantum dot lasers," *Appl Phys Lett,* vol. 78, no. 19, pp. 2825-2827, 2001.

[156]   L. Zhang *et al.*, "Low timing jitter, 5 GHz optical pulses from monolithic two-section passively mode-locked 1250/1310 nm Quantum Dot lasers for high speed optical interconnects," in *Optical Fiber Communication Conference*, 2005: Optical Society of America, p. OWM4.

[157] T. W. Berg and J. Mørk, "Quantum dot amplifiers with high output power and low noise," *Appl Phys Lett,* vol. 82, no. 18, pp. 3083-3085, 2003.

[158] L. Asryan and R. Suris, "Inhomogeneous line broadening and the threshold current density of a semiconductor quantum dot laser," *Semiconductor science and technology,* vol. 11, no. 4, p. 554, 1996.

[159] A. Kovsh, I. Krestnikov, D. Livshits, S. Mikhrin, J. Weimert, and A. Zhukov, "Quantum dot laser with 75nm broad spectrum of emission," *Opt Lett,* vol. 32, no. 7, pp. 793-795, 2007.

[160] J. C. Norman *et al.*, "A Review of High-Performance Quantum Dot Lasers on Silicon," (in English), *Ieee J Quantum Elect,* vol. 55, no. 2, Apr 2019, doi: 10.1109/Jqe.2019.2901508.

[161] E. U. Rafailov *et al.*, "High-power picosecond and femtosecond pulse generation from a two-section mode-locked quantum-dot laser," *Appl Phys Lett,* vol. 87, no. 8, p. 081107, 2005.

[162] G. Steinmeyer, D. Sutter, L. Gallmann, N. Matuschek, and U. Keller, "Frontiers in ultrashort pulse generation: pushing the limits in linear and nonlinear optics," *Science,* vol. 286, no. 5444, pp. 1507-1512, 1999.

[163] N. Ledentsov *et al.*, "Direct formation of vertically coupled quantum dots in Stranski-Krastanow growth," *Physical Review B,* vol. 54, no. 12, p. 8743, 1996.

[164] A. Patane, A. Polimeni, M. Henini, L. Eaves, P. Main, and G. Hill, "Thermal effects in quantum dot lasers," *Journal of applied physics,* vol. 85, no. 1, pp. 625-627, 1999.

[165] S. Sanguinetti, M. Henini, M. G. Alessi, M. Capizzi, P. Frigeri, and S. Franchi, "Carrier thermal escape and retrapping in self-assembled quantum dots," *Physical Review B,* vol. 60, no. 11, p. 8276, 1999.

[166] D. Bimberg *et al.*, "Quantum dot lasers: breakthrough in optoelectronics," *Thin Solid Films,* vol. 367, no. 1-2, pp. 235-249, 2000.

[167]   H.-Y. Liu, Q.-F. Dai, L.-J. Wu, S. Lan, V. Trofimov, and S. Varentsova, "Effects of p-type doping on the optical properties of InAs/GaAs quantum dots," *Solid state communications,* vol. 152, no. 5, pp. 435-439, 2012.

[168]   O. Shchekin and D. Deppe, "The role of p-type doping and the density of states on the modulation response of quantum dot lasers," *Appl Phys Lett,* vol. 80, no. 15, pp. 2758-2760, 2002.

[169]   I. Sandall *et al.*, "The effect of p doping in InAs quantum dot lasers," *Appl Phys Lett,* vol. 88, no. 11, p. 111113, 2006.

[170]   D. G. Deppe, H. Huang, and O. B. Shchekin, "Modulation characteristics of quantum-dot lasers: The influence of p-type doping and the electronic density of states on obtaining high speed," *Ieee J Quantum Elect,* vol. 38, no. 12, pp. 1587-1593, 2002.

[171]   A. J. Zilkie *et al.*, "Carrier Dynamics of Quantum-Dot, Quantum-Dash, and Quantum-Well Semiconductor Optical Amplifiers Operating at 1.55$\mu {\hbox {m}} $," *Ieee J Quantum Elect,* vol. 43, no. 11, pp. 982-991, 2007.

[172]   B. Ohnesorge, M. Albrecht, J. Oshinowo, A. Forchel, and Y. Arakawa, "Rapid carrier relaxation in self-assembled In x Ga 1− x As/GaAs quantum dots," *Physical Review B,* vol. 54, no. 16, p. 11532, 1996.

[173]   R. K. Willardson, E. R. Weber, and M. Sugawara, *Self-Assembled InGaAs/GaAs Quantum Dots*. Academic Press, 1999.

[174]   F. X. Kurtner, J. A. Der Au, and U. Keller, "Mode-locking with slow and fast saturable absorbers-what's the difference?," *IEEE Journal of Selected Topics in Quantum Electronics,* vol. 4, no. 2, pp. 159-168, 1998.

[175]   M. Thompson *et al.*, "Properties of InGaAs quantum dot saturable absorbers in monolithic mode-locked lasers," in *2004 IEEE 19th International Semiconductor Laser Conference, 2004. Conference Digest.*, 2004: IEEE, pp. 53-54.

[176]   T. Akiyama *et al.*, "An ultrawide-band semiconductor optical amplifier having an extremely high penalty-free output power of 23 dBm achieved with quantum dots," *Ieee Photonic Tech L,* vol. 17, no. 8, pp. 1614-1616, 2005.

Chapter 2 Experimental Methods

2.1. Epitaxy Structure

The initial step in sample preparation is developing GaAs-based high-quality wafers with a specially designed InAs QDs active region. The wafers utilised in this work were all grown by the molecular beam epitaxy (MBE) machine, which allows precise control of the chemical composition and doping levels during the growth process [1-4]. Instead of explaining the working principle of the MBE, this section focuses mainly on our specialised QD formation process.

The entire epitaxial layer was deposited layer-by-layer in the growth chamber of the MBE, with chosen elements Be and Si for p-type and n-type doping, respectively. The detailed epitaxy configuration of the wafer is given in Table 2.1, where a general p-i-n structure is built on top of the GaAs (001) substrate by controlling the dopant concentration in each layer. An attention-grabbing feature of our active region is that rather than using a conventional dot-in-well (DWELL) structure where the QDs are sandwiched between two quantum wells, the self-assembled InAs QDs are directly grown on the GaAs surface via Stranski-Krastanov (SK) growth mode. As depicted in Fig. 2.1, the QD growth starts from the deposition of element In and As which leads to the formation of a two-dimensional (2D) InAs wetting layer on the surface of the GaAs layer. When the thickness of the InAs wetting layer reaches a critical value of 1.7 monolayers (MLs), this 2D thin-film layer transits to three-dimensional (3D) islands due to the 7.2% lattice mismatch between the InAs composition and the GaAs substrate [5-7]. Here, the InAs QDs are formed by supplying 2.7 MLs of InAs and capped by a 3.7 nm-thick InGaAs strain-reducing layer (SRL). Compared with GaAs, the larger lattice constant of InGaAs enables a strain relaxation in the growth direction of InAs QDs, resulting in larger dot size and longer emission wavelength (~ 1.3 μm) [8, 9]. Moreover, the dot coverage with InGaAs SRL could preserve a good dot uniformity, achieving relatively narrow photoluminescence (PL) full-width-half-maximum (FWHM) of ~28-30 meV at room temperature. In addition, a greater than the usual

number of QD layers (8 or 10 layers in total) is employed to obtain the desired high optical gain [10]. By adopting appropriate growth conditions, a high dot density with good dot uniformity can be preserved in such strain-driven self-assembly GaAs/InAs QDs. As presented in Fig. 2.1 (Right top), the AFM image reveals that an ultrahigh dot density of 5.9×10^{10} cm^{-2} is accomplished without any degradation in dot uniformity, which is almost double our previous result of 3×10^{10} cm^{-2} (shown in Right bottom of Fig. 2.1). The wafers used in this project were grown by the QD Laser Inc., Kawasaki, Kanagawa, Japan.

Table 2.1 Epitaxy layer structure of GaAs-based wafer.

Material	Designed Al content x	Designed Thickness (nm)	Typical Doping Density (cm^{-3})	Repeat
p-GaAs		100	Be: 2×10^{19}	1
		300	Be: 1.4×10^{19}	
p-Al$_x$Ga$_{1-x}$As	0.2	20	Be: 1.4×10^{19}	
	0.4	1400		
	0.2	20		
GaAs	-	24		
i-GaAs		35.5		8 or 10
InGaAs SRL		3.7		
InAs QD		0.8 (~ 2.7 ML)		
GaAs	-	60		1
n-Al$_x$Ga$_{1-x}$As	0.2	20		
	0.4	1400		
	0.2	20	Si: 6×10^{18}	
n-GaAs	-	300	Si: 1×10^{18}	
n-GaAs Sub.	-	3 inches	Si: 1-1.5 $\times 10^{18}$	
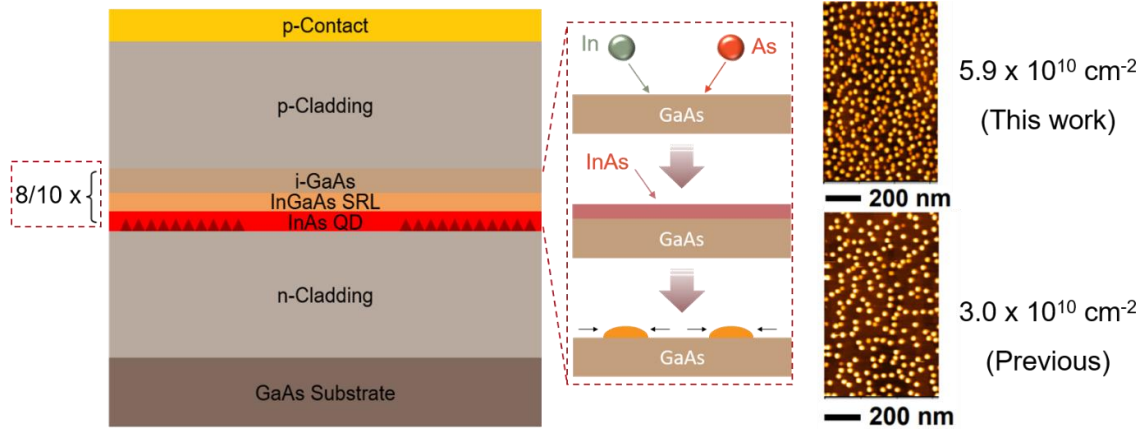
Figure 2.1 Left: Schematic diagram of InAs/GaAs QD layer structure. Middle: Schematic diagram showing formation sequence of self-assembled InAs QDs. Right: Atomic force microscope (AFM) images of InAs QDs density achieved in this and previous work.

2.2. Device Fabrication

After material inspections, the well-prepared wafer will be cleaved into pieces, and ready for nanofabrication. The layouts of the designed structures are shown in Fig. 2.2, where the two-section passively QD-MLLs with SA-to-gain length ratio ($\frac{L_{SA}}{L_{gain}}$) ranging from 1: 3 to 1: 7 can be found. The general fabrication process, including photolithography, wet/dry chemical etching, and metal/dielectric deposition, is summarised in a flowchart (Fig. 2.3). The corresponding cross-sectional and three-dimensional views of each main fabrication step are referred to Fig. 2.4. Appendix. A details the full fabrication procedure and corresponding parameters in each step; the following sections provide a brief description of the most essential methodologies involved.

It should be mentioned that due of the LCN clean-room refurbishment issue and the closure of UCL during the COVID-19 pandemic, all fabrication steps were conducted outside of UCL by me as an exchange student. With the help of Dr Jianou Huang, the first complete manufacturing cycle took place in 2019 at the Eindhoven University of Technology (TU/e), Netherlands. Later in 2021, as a consequence of the device degradation, samples were re-fabricated at the Institute of Physics, Chinese Academy of Sciences (CAS), China. The second process flow

was greatly supported by Mr Mingchen Guo and Mr Bo Yang.
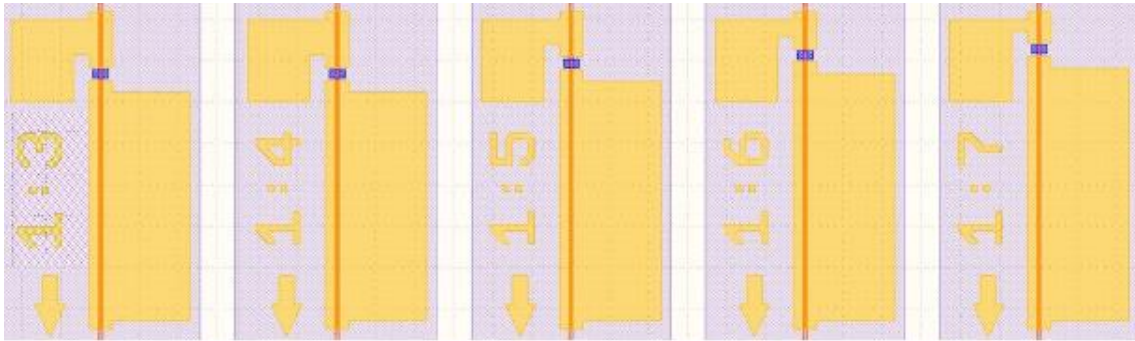
Figure 2.2 Layouts of designed devices using Klayout.

Figure 2.3 Flowchart of the MLL fabrication process.

1) Ridge Etching		— 1µm
2) Passivation		— 1µm
3) Open Window		— 1µm
3) P-metal Deposition		100µm
4) Gap Etching		— 1µm
5) N-metal Deposition		100µm
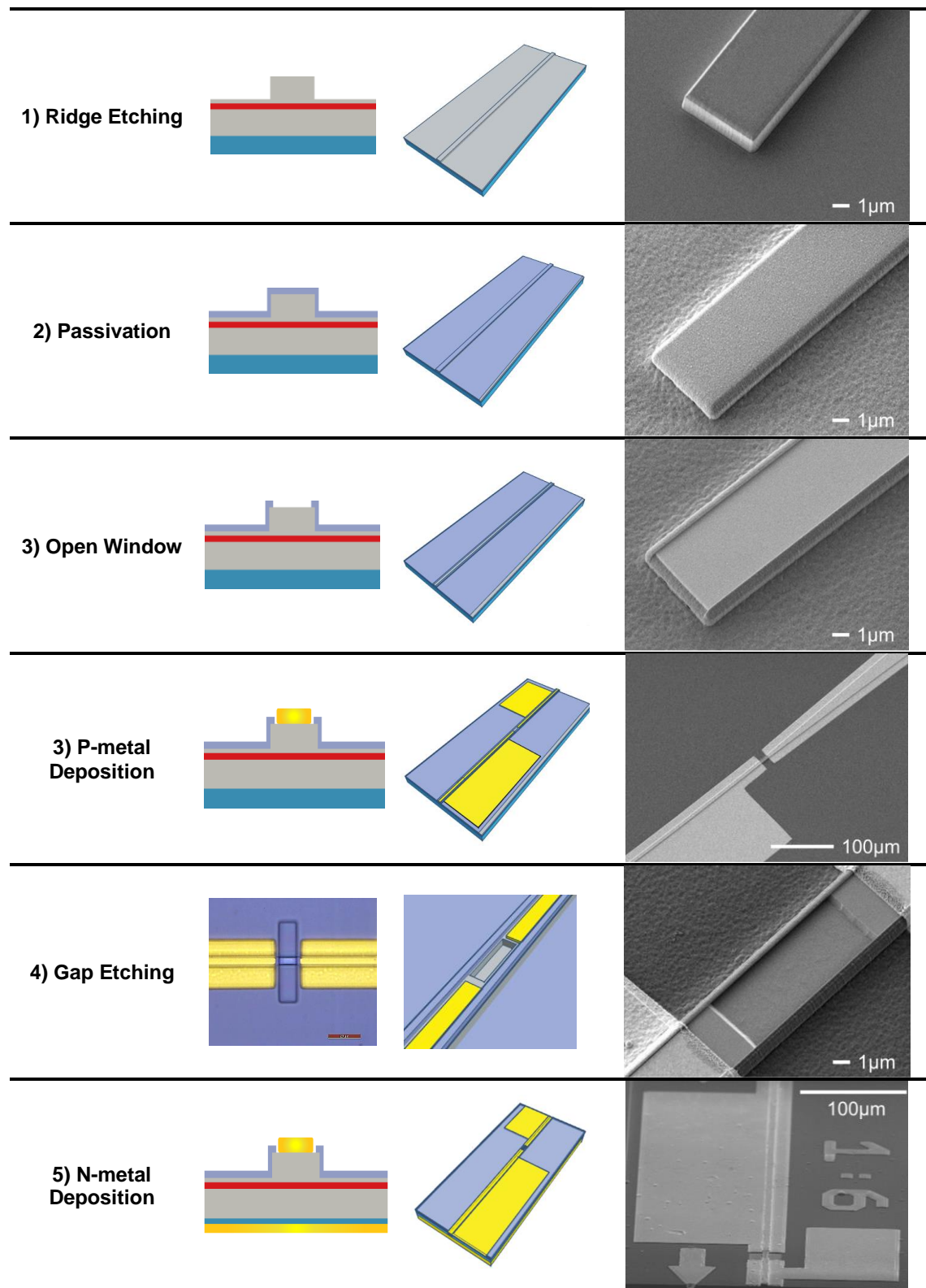
Figure 2.4 The schematic diagrams showing the cross-sectional (Left) and three-dimensional (Middle) views of the main fabrication steps. Right: the corresponding SEM images of each step.

2.2.1. Sample Cleaning

The sample cleaning process is the very first step for semiconductor fabrication. It aims to remove both chemical and particle impurities without damaging the substrate. Any contaminants on the sample surface may deteriorate device performance, leading to device failure and, ultimately, limiting the yield of device manufacturing [11]. In this work, the wafer was ultrasonically cleaned with acetone for 5 minutes, followed by an additional 5-minute soak in isopropyl alcohol (IPA). Albeit the acetone solvent can effectively remove the organic dirt particles and semiconductor dust, it leaves a residue on the sample surface because of the rapid evaporation. IPA, as an excellent rinse agent, could dissolve the residue and avoid stained surfaces. Afterwards, the sample was dipped into deionised (DI) water, blown dry by a nitrogen gun, and inspected under a microscope. This cleaning process was repeated until the cleanliness of ≤ 4 particles per field of view on 50x magnification is achieved. Finally, a dehydration bake for 3 minutes at 150 °C was applied to remove all moisture from the substrate.

2.2.2. Lithography

In semiconductor lasers, the designed structure is commonly obtained via a direct pattern transfer technique called lithography. There are different types of lithography, such as conventional photolithography, electron beam lithography (EBL), ion beam lithography (IBL), X-ray lithography and laser direct writing lithography (LDWL). Conventional photolithography, with the ability of parallel process, has been widely used in the large-scale semiconductor industry. However, this contact printing method inevitably requires the use of photomasks, which significantly reduces the operational flexibility [12, 13]. As an alternative optical lithography technique, LDWL utilises a focused laser beam to directly transfer the pattern on a substrate surface. It is a non-contact, maskless and flexible patterning technique [14]. In this work, all lithography steps were carried out in the LDWL system (Heidelberg DWL66+).

The general process of LDWL is illustrated in Fig. 2.5. Before the lithography

session, a light-sensitive polymer named photoresist will be spun coated on the sample surface. In general, the photoresist can be divided into two tones: positive and negative, which show exactly opposite characterisations in response to radiation exposure. For a positive photoresist, the photosensitive compound in the exposed area will transform into a more soluble portion due to the photochemical reaction. On the contrary, the exposed region in the negative photoresist tends to become more insoluble in the developing solution. Normally, the selection of a certain type of photoresist is aimed to minimise the laser direct writing time. For example, a positive photoresist is typically desired in 'p-/n- metallisation' and 'open window' steps while a negative photoresist is more preferred for defining laser ridges. Here, only positive photoresists are involved in the whole fabrication process due to the absence of negative photoresists in our laboratory.
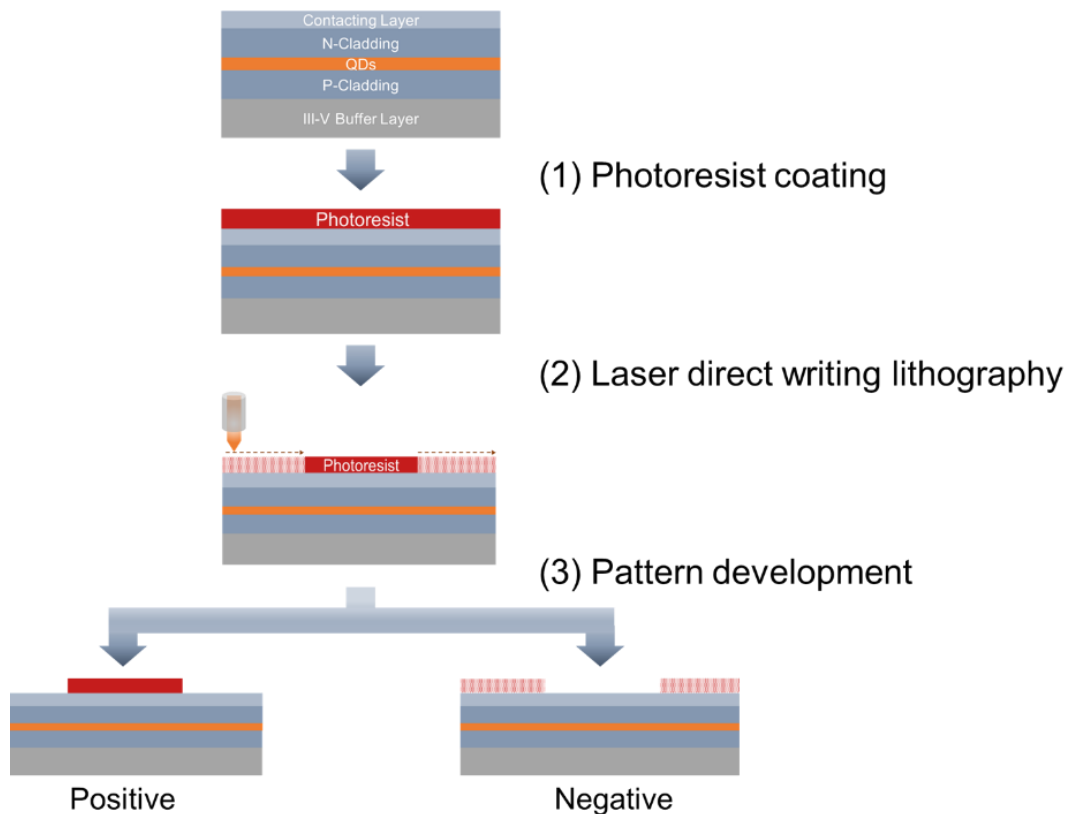
Figure 2.5 Standard process for LDWL with positive and negative photoresist.

In most cases, a uniform resist film (SPR220-3.0) with great adhesion will be spin-coated on the sample surface for pattern developments. However, this changes in

the case of 'photolithography for metallisation', where a bi-layer lift-off method is introduced. As depicted in Fig. 2.6, the resist LOR10B—a sacrificial release layer—is used as an underlayer in combination with the SPR220-3.0. Because the LOR10B is a non-photosensitive but more soluble resist, an undercut structure will be formed after development. This is critical for allowing the acetone to reach and dissolve the resists during the lift-off process. Consequently, the metal deposited on the top of the photoresist could be completely removed via acetone immersion. Figure 2.7 shows the microscope images of developed samples for both coating methods, where the double lines in Fig. 2.7 (b) indicate a significant undercut structure. The cross-sectional high-resolution SEM image of this undercut structure is displayed in Fig. 2.7 (c).
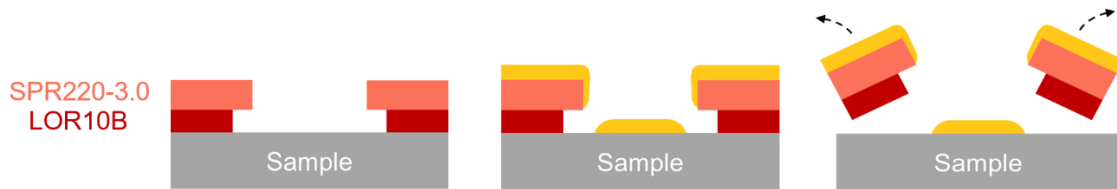
Figure 2.6 Schematic diagram of bi-layer lift-off process.
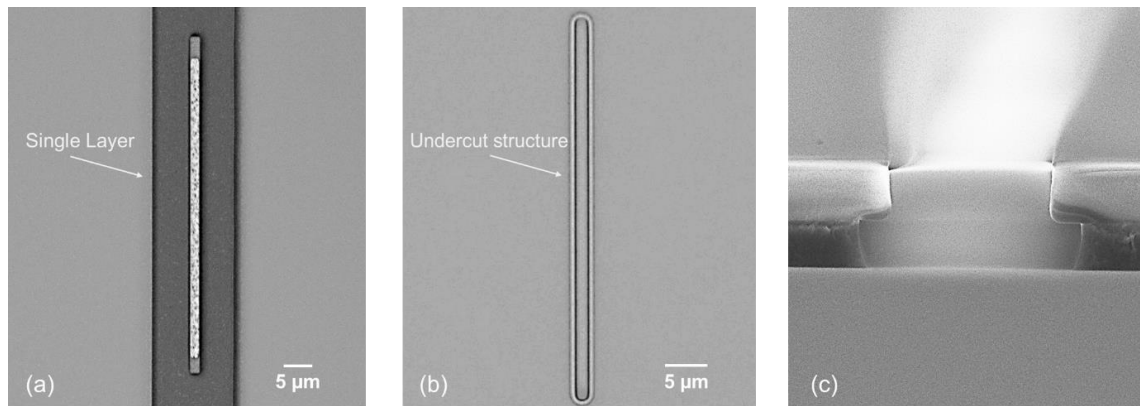
Figure 2.7 Microscope images of developed sample coated with (a) single layer of SPR220-3.0; (b) bi-layer method. (c) SEM image of formed undercut structure in (b).

2.2.3. Etching

After the lithography session, the patterned features will be defined via either wet or dry etching process. If the etching process involves using chemical solvents (i.e., the etchants) to remove the material, it is called wet etching. Basically, the etchants

consist of an oxidizing agent (e.g., H_2O_2), an agent for dissolving the oxides (e.g., H_2SO_4, HCl, HF, and H_3PO_4), and a solvent (e.g., DI water) [15]. By dipping the sample into a liquid-based etchant, the exposed wafer area will be dissolved via chemical reactions, which forms a soluble by-product, while the unexposed area will be protected by an insoluble photoresist that is resistant to etching.

The dry etching process (also known as the plasma etching), on the other hand, refers to the use of etchant gases. In this case, the etching takes place in a vacuum chamber filled with selected gases (e.g., BCl_3, CHF_3, CF_4, Cl_2, Ar, and O_2). A strong RF electromagnetic field is applied to accelerate the collision between electrons and neutral gas molecules, which prompts an ionization of gases and thus generates a plasma [16-18]. As illustrated in Fig. 2.8, the ions will diffuse towards the sample surface until adsorption occurs. Then, the chemical reaction between the radicals will produce some volatile gaseous by-products, which will disperse into the flowing gas and be further expelled through the vacuum system [17, 19, 20]. Currently, almost all dry etching procedures combine the chemical reaction with the physical bombardment of the ions to enhance the etching results [21-24]. To avoid photoresist degradation during the plasma exposure, a more durable dielectric mask, such as SiO_2, is generally preferred.
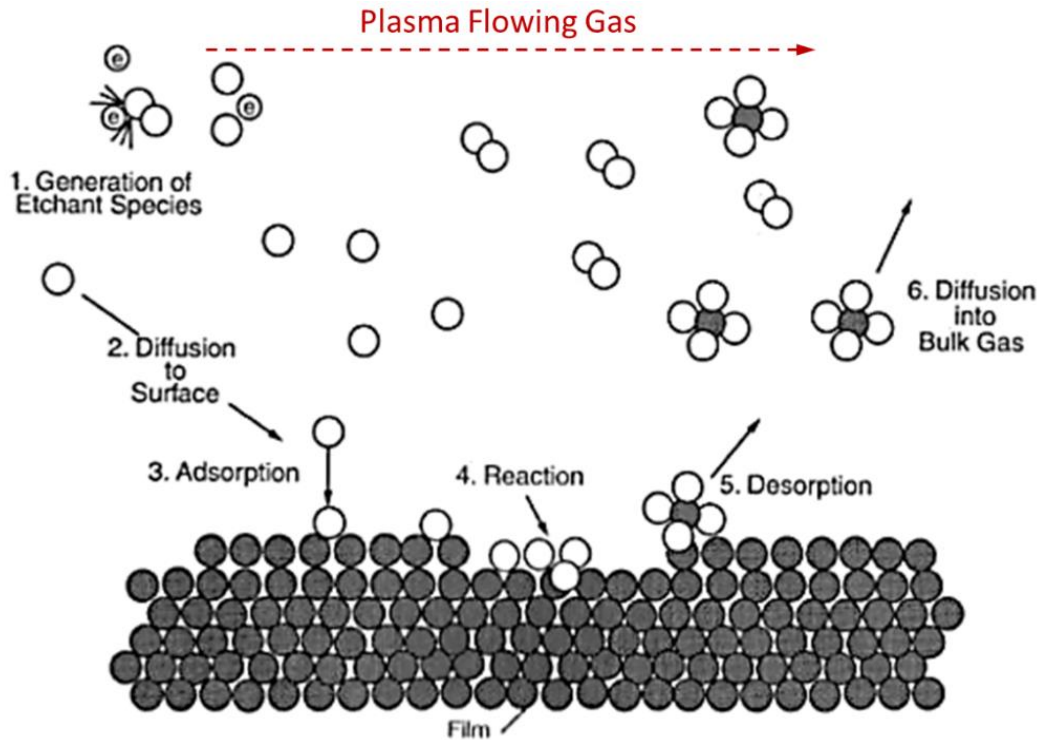
Figure 2.8 Schematic for dry etching process [25].

Normally, in a complete fabrication flow, numerous etching steps are involved. Therefore, as an extremely important fabrication step, both wet and dry etching mechanisms have been widely studied. The general comparisons between those two major types of etching are summarised in Table 2.2. Despite the chemical handling hazards, wet etching is fairly cheap since no specialised equipment is required. Besides, a bunch of options are available due to the characterised nature of various chemical solutions, depending on the specific material to be etched. Meanwhile, it benefits from the simple implementation, high material selectivity, and high etching rate. However, the wet chemical etching tends to be isotropic in nature, which means that the etch rates are equal in all spatial directions [26]. If it is not well controlled, undercutting of the mask may lead to a narrowing neck of the mesa. A comparison of general features of wet and dry etching for GaAs is provided in Fig. 2.9. In addition, the isotropic wet etching could have worse effects on small features (< 5 μm), where the whole ridge may be etched away. Fig. 2.10 (a) shows Dektak surface profiles of 3 μm-width and 15 μm-width ridges before

and after wet etching. During the etching process, both ridges are covered by a photoresist. Unlike the 15 μm-width ridges, after 5 mins etching in citric acid solution (Citric: H_2O_2: H_2O = 10: 1: 10), for the 3 μm-width ridges, the ridges disappeared (shown in Fig. 2.10 (b)) and the floating masks can be seen in the micrograph image in Fig. 2.10 (c). Apart from this, the etching rate is particularly susceptible to acid concentration, etching temperature, as well as etchant freshness [27]. Hence, even the same recipe might deliver various results in different wet etching processes. For those reasons, we employ isotropic wet etching only for etching the gap between the gain section and the SA section, as the main claim for this step is electrical isolation with no specific requirements of the etched profile. It should be mentioned that our choice of "Citric: H_2O_2: H_2O = 10: 1: 10" as the wet etchant results from its high selectivity for GaAs over AlGaAs [28-30].

Table 2.2 Comparisons between wet and dry etching.

	Wet Etching	Dry Etching
Method	Chemical	Physical and/or Chemical
Environment	Atmosphere	Vacuum Chamber
Advantages	1) Easy to implement 2) Good material selectivity 3) High etching rate	1) Repeatable 2) High resolution (< 100 nm) 3) Precise process control
Disadvantages	1) Poor resolution (~ 1 μm) 2) Poor process control 3) Chemical handling hazards	1) Expensive 2) Low throughout 3) Poor selectivity
Etch Profile	Isotropic	Anisotropic
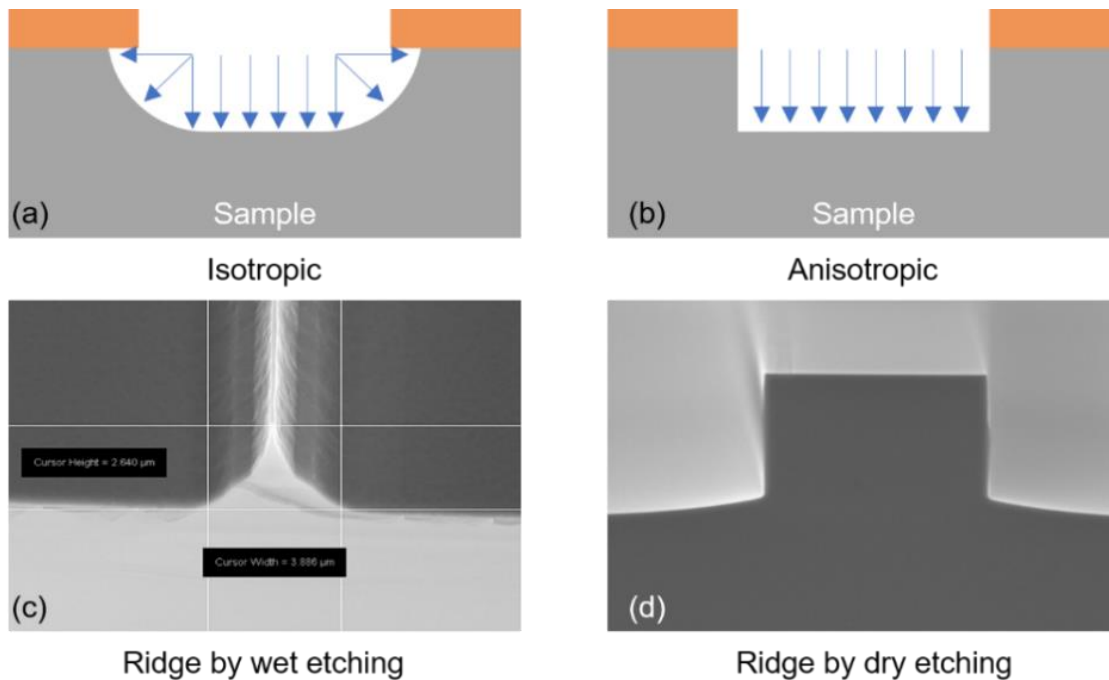
Figure 2.9 (a) Isotropic profile, (b) Anisotropic profile. SEM images of etched ridge profile by (c) wet etching and (d) dry etching.
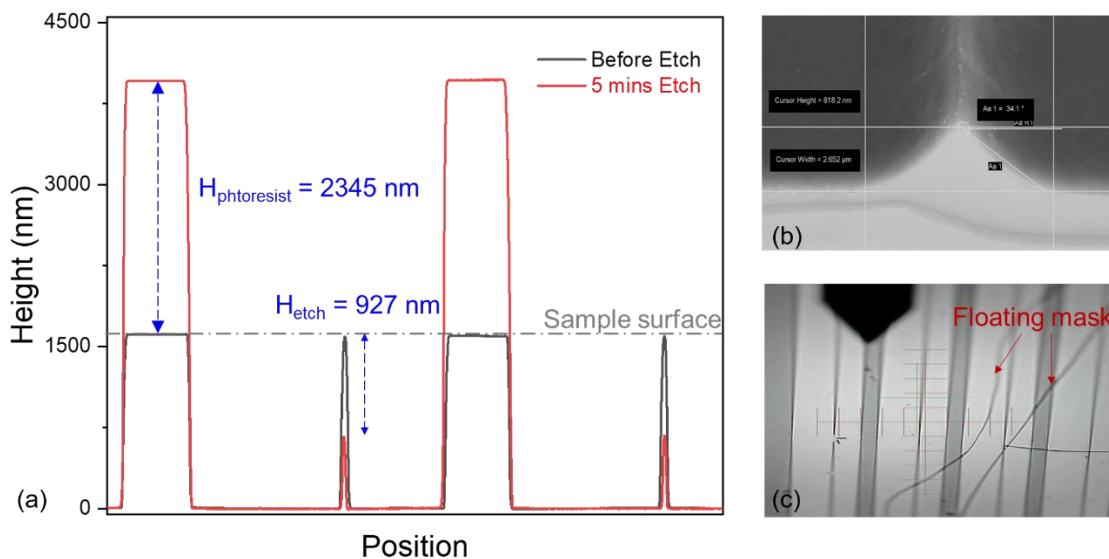
Figure 2.10 Dektak profiles of patterned samples before etching and after 5 mins wet etch. (b) SEM image of etched narrow ridge structure. (c) Microscopy image of sample surface after wet etching.

By contrast, dry etching eliminates the need for handling dangerous chemicals and is much more repeatable compared with wet etching. In principle, near-vertical sidewalls could be realised by choosing a set of etchant gases in an optimised

condition [31]. Here, two most common plasma-based etching techniques named the reactive-ion etching (RIE) and the inductively coupled plasma (ICP) etching are employed. Although the working mechanisms behind those two techniques are similar, they differ in equipment construction. Figure 2.11 (a) illustrates the simplified schematic of a conventional parallel plate RIE system, where an RF (13.56 MHz) voltage is applied to one of the plates while the other is grounded. In such a time-varying electric field, those two plates act as electrodes and form a capacitor, and the reactive gases will be ionized by electrons whenever they flow into the chamber [19, 20, 32]. During the electromagnetic field oscillation, electrons in the plasma tend to travel fast and impact both the chamber walls and the substrate holder (down plate). Those negative charges will be absorbed by the electrically grounded chamber walls, while accumulated in the DC isolated holder. At the same moment, the massive ions cannot travel far, and hence their high concentration will build up an ion sheath [33]. Consequently, a potential difference of up to a few hundred volts is developed between the substrate holder and the ion sheath, pulling the ions towards the substrate with significant mechanical energy. This physical effect combined with the chemical reaction allows the exposed area to be etched efficiently. Although the RIE system aims to minimize lateral etching, the inevitable particle collisions will lead to a wide angular ion distribution, thereby forming a more isotropic etched profile than ICP etcher [34]. It may also be noticed that plasma density in the RIE system is approximately proportional to RF power, so as the ion bombardment energy [35, 36]. Albeit a high-density plasma (HDP) is always desired in the dry etching process, the high ion bombardment energy may cause physical damage to the wafer surface. Therefore, in our works, RIE (Oxford PlasmaPro 80 RIE) is mainly used to etch hard masks and dielectric material with fluorine-based gases. The optimal etch recipe for SiO_2 is given in Table 2.3.

The main difference between the ICP etcher and RIE etcher is the independent 13.56 MHz RF power source for plasma generation. Although the ICP system is more complicated internally, it enables greater process flexibility. As shown in Fig. 2.11 (b), the plasma discharge region in the ICP system is circled by a few turns of

induction copper coils exposed to a time-varying high-level RF source. The induced electromagnetic field tends to circulate the electrons, which enhances the collisions between electrons and ions and ultimately fulfils the ionizations [37]. The generated ions will be attracted to the sample holder by an electric field, similar to the RIE method. Thanks to the separate RF sources in an ICP system, the etching process becomes much more controllable; namely, the plasma density and the momentum of ions could be tuned unrelatedly. For this reason, an HDP at low pressure could be obtained, preventing the rough sidewalls as well as the etch grass formation [33, 38]. This is particularly important in patterning high-aspect-ratio features [39]. In this work, our ICP (Oxford Plasmalab 100 ICP) etcher is equipped with Chlorine-based gases for semiconductor etching. The etching parameters are listed in Table 2.4.
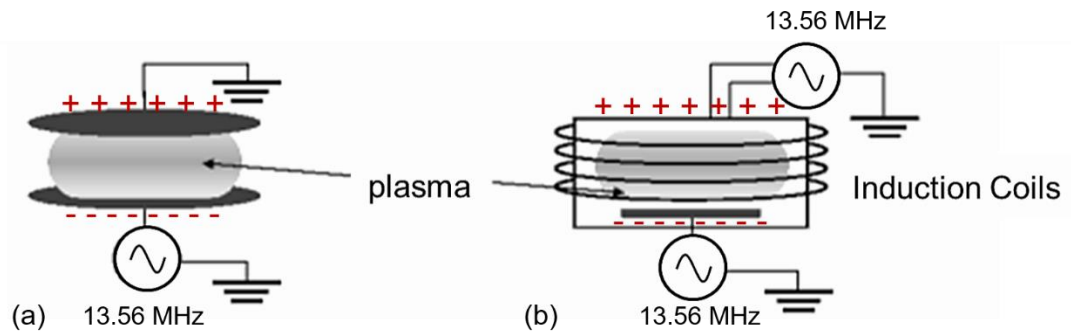
Figure 2.11 Simplified schematic diagram of (a) RIE system and (b) ICP system.

Table 2.3 Parameters for SiO₂ etching in PlamaPro 80 RIE.

	CHF_3 (sccm)	Ar (sccm)	Pressure (mTorr)	RF Power (W)	DC bias (V)	Chamber Temperature (°C)	Etch Rate (nm/min)
SiO_2	90	10	100	200	440	15	30

Table 2.4 Parameters for GaAs/AlGaAs etching in Plasmalab 100 ICP.

	BCl_3 (sccm)	Cl_2 (sccm)	Ar (sccm)	Pressure (mTorr)	RF Power (W)	DC bias (V)	Chamber Temperature (°C)	Etch Rate (nm/min)
GaAs/AlGaAs	10	6	4	6	50	170	10	16.8

2.2.4. Passivation

Surface passivation has been considered as a crucial processing step for the fabrication of a well-performed semiconductor laser. Immediately after the etching procedure, the etched ridge will be passivated by a layer of dielectric material (e.g., SiO_2 or SiN_x) that can prevent long-term degradation problems and provide electrical isolation. Here, a 500 nm SiO_2 passivation layer (shown in Fig. 2.12) was deposited by an inductively coupled plasma-enhanced chemical vapour deposition (ICPECVD) at a temperature as low as 80°C. Compared with conventional plasma-enhanced chemical vapour deposition (PECVD), ICPECVD benefits from a higher density of generated plasma, a lower operating temperature, and a denser deposited layer [40]. Despite its flexible operation system, the combination of gas ratios and plasma power must be carefully selected to achieve ideal deposition layers [41]. In our case, the typical $SiH_4/O_2/Ar$ mixture is applied to provide the oxidant and the sputtering agent [42, 43]. The optimised SiO_2 growth recipe is given in Table 2.5.
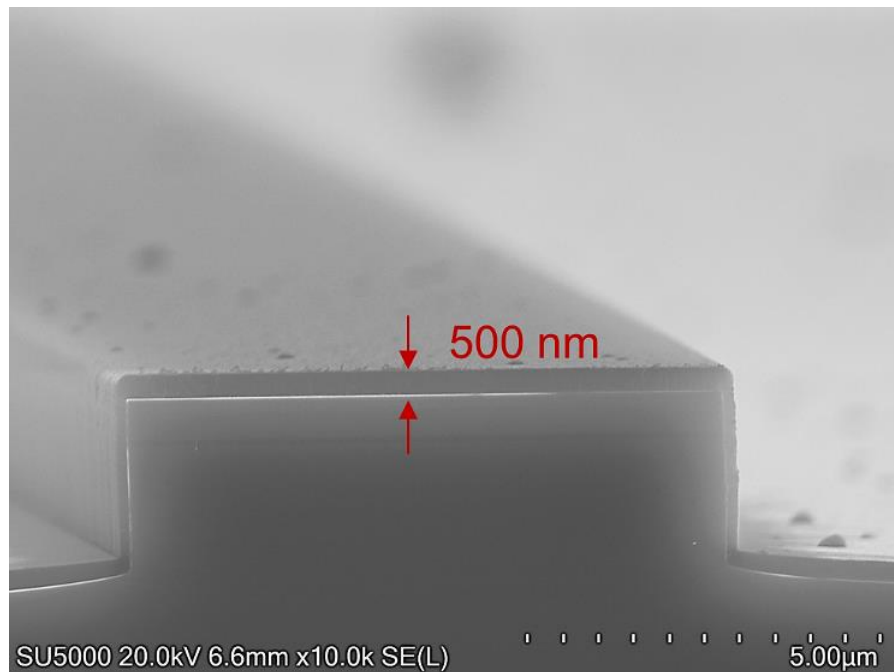
Figure 2.12 SEM image of an etched ridge with 500 nm deposited SiO_2 layer.

Table 2.5 Parameters for SiO$_2$ deposition in SENTECH SI 500D ICPECVD.

	SiH$_4$ (sccm)	O$_2$ (sccm)	Ar (sccm)	Pressure (mTorr)	ICP Power (W)	Chamber Temperature (°C)	Growth Rate (nm/min)
SiO$_2$	6.8	13	126	0.9	350	80	25.8

2.2.5. Metallisation

Basically, intimate contact between a metal and a semiconductor will form a Schottky barrier at the interface, whose height will significantly influence the carrier mobility [44]. Commonly, a low barrier height can bring fast carrier mobility, i.e., a low contact resistance. As a high contact resistance may result in excessive heating and potentially damage the electrical devices, an extremely low metal-semiconductor contact resistance is a prerequisite for high-performance semiconductor laser diodes. Ideally, a negligible contact resistance should be achieved to give a so-called ohmic contact formation, resulting in a quasi-linear current-voltage relationship [25]. Generally, there are two transport mechanisms of carrier flow across the barrier: the thermionic emission in which an electron overcomes the barrier height with a thermal energy and the field emission with a tunnelling effect in a narrow barrier [45, 46]. The latter predominates the current transmission in our case. To enhance the tunnelling effect, highly doped p-type and n-type GaAs contact layers with a corresponding doping level of 2×10^{19} cm^{-3} and 1×10^{18} cm^{-3} were grown, respectively.

Based on previous studies of ohmic contact performance on InGaAs/GaAs-based layers [47-50], a Ti/Pt/Ti/Au (20/20/20/200 nm) metallisation scheme was applied on the p-GaAs contact layer. The Ti is a recommended interlayer for promoting adhesion strength between different materials [51, 52]. The usage of the Pt layer can effectively prevent the mutual diffusion between Au and GaAs layers during the thermal annealing process [53]. The final deposited Au layer is essential to provide a good conductivity without oxide formation, enhancing the device reliability and facilitating bonding or probing of the devices [54]. Once the deposition of the Au layer is finished, the ohmic contact to the p-GaAs surface is

made by using the rapid thermal annealing (RTA) technique at 425°C for 60 seconds. It's worth mentioning that disconnection of p-metal film around the sidewall of ridges might occur due to the absence of planarisation step. To avoid the metallisation failure caused by the depth of the defined ridge, an angle-tilted second p-type metal deposition was introduced after the Ti/Pt/Ti/Au multilayer. As presented in Fig. 2.13 (a), our sample is first fixed on a specially designed 45° pre-tilt holder, where a Ti/Au (20/400nm) layer stack can be deposited. Then, relocate the deposition side to another direction, followed by another Ti/Au layer with a thickness of 20/400 nm. At the end, the sample is transferred back to a flat holder and a Ti/Au layer (20/600 nm) is deposited vertically. The SEM image after this 'three-step' angle-tilted deposition is shown in Fig 2.13 (b), where three metal layers can be clearly seen. No additional RTP process is required.
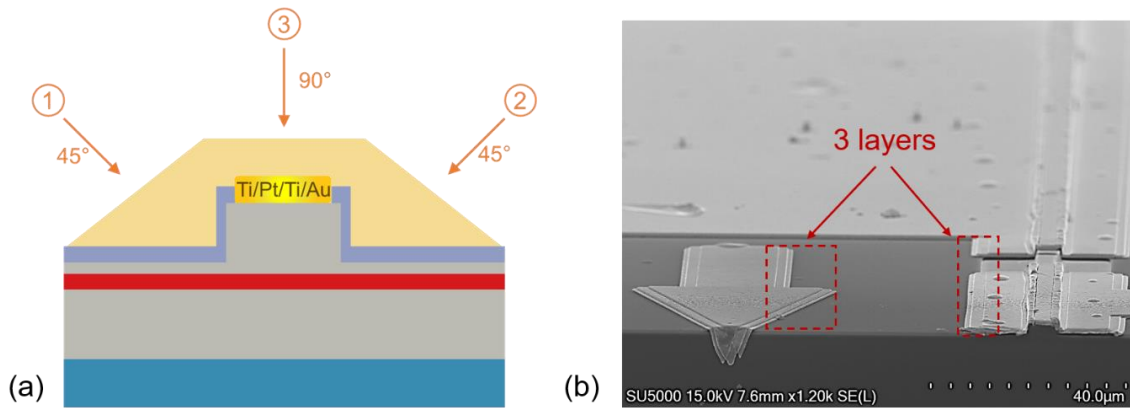
Figure 2.13 (a) Schematic diagram of angle-tilted second p-type metal deposition. (b) SEM image showing the three deposited p-type metal layers.

Before n-contact metallisation, a mechanical lapping procedure is employed to thin and polish the sample to around 120 μm, enhancing thermal management of the device. The entire backside of the sample is evaporated with a standard Ni/Ge/Au/Ti/Au multilayer in a thickness of 25/32.5/65/20/200 nm, respectively. The Ni layer can improve the adhesion between n-GaAs and AuGe, and the diffusion of the Ge and Au allows a formation of NixGeAs at the GaAs interface to provide a low contact resistance [55-58]. The Ti layer acts as another adhesion layer, while the final thick Au layer enables a better electrical contact [59-61]. The

n-type ohmic contact is achieved by a 350°C thermal annealing for 60 seconds.

In this work, prior to each deposition step, the sample was de-oxidized in a dilute ammonia solution (NH_4OH: H_2O at a ratio of 1: 19) for 30 seconds. And all metal deposition processes were completed in an electron beam (E-beam) evaporator (Peva-600E).

2.3. Experimental Setup

The experimental setups for characterising two-section InAs/GaAs QD passively MLLs are described in this section, including the basic *L-I-V* curves, the fundamental mode-locking characteristics (like optical spectrum, RF spectrum and autocorrelations), the noise figures (such as RIN and phase noise), and the transmission evaluations (e.g., eye diagrams and bit-error rates (BERs)). All basic *L-I-V* measurements were carried out in the Room 704 of the UCL Robert Building. Almost all mode-locking characteristics and the noise analysis were conducted in the J Lab of the UCL Robert Building, except the mapping of mode-locking region which was performed in the ONG Lab of the UCL Robert Building. Special thanks to Dr Lalitha Ponnampalam and Dr Zichuan Zhou, whom have been extremely supportive during my work in the J Lab and the ONG Lab, respectively. All transmission evaluations were established in the NOEIC, Wuhan, China, under the help of Dr Hongguang Zhang, Mr Jie Yan, and Mr Dingyi Wu.

Before the characteristic session, the fabricated devices are mounted p-side up on an indium-plated copper heat sink and gold-wire-bonded to enable all measurements (as shown in Fig. 2.14). Three DC probe needles are used for current injection, voltage bias, and grounding. A microscope camera is adopted for positioning the DC probe needles. Besides, a thermoelectric temperature controller (TEC), model ILX Lightwave LDT-5910, is used during the measurements for thermal management purposes. Two GBIP-controllable power sources (Keithley 2400) are used to provide precise injection current (I_i) and reverse-bias voltage (V_{rev}).
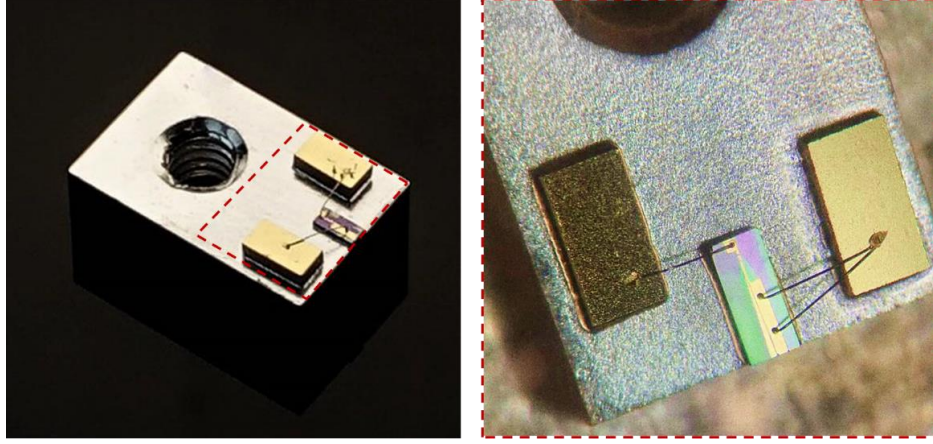
Figure 2.14 The photograph (left) and the microscope image (right) of two-section QD-MLL after mounting and bonding.

2.3.1 L-I-V curve

The L-I-V measurement is the first to be carried out since it can provide direct evidence of whether the devices work properly and how well they perform. The simplified schematic of this setup is presented in Fig. 2.15, and an integrating sphere is used to collect light emitted from the laser facet. A LabView program is used to automatically control the current source and acquire corresponding output power for subsequent analysis.

Figure 2. 16 demonstrates a typical *L-I*, *V-I*, and wall-plug efficiency (WPE) curves of an electrically pumped two-section GaAs/InAs QD-MLL at room temperature. As I_i increases, the spontaneous emission dominants in the first place until a threshold current (I_{th}) is reached, after which the dominant mechanism within the laser cavity changes to the stimulated emission. This is evidenced in the dramatically increased output power (P_{out}) when the I_i is larger than the I_{th}. As a crucial parameter of laser device, the I_{th} is dependent on the geometry of the cavity. Therefore, it is preferred to use a size-independent parameter—the threshold current density (J_{th})—whenever comparing two different devices, and the equation for J_{th} is [62]:

$$J_{th} = \frac{I_{th}}{W_{ridge} * L_{cavity}} \qquad 2.1$$

where the W_{ridge} is the ridge width of the laser device and the L_{cavity} represents the cavity length. The slope efficiency (η) derived from the *L-I* curve is another important parameter that is commonly measured in units of watt per ampere (*W/A*), and expressed as [63]:

$$\eta = \frac{\Delta P_{out}}{\Delta I_{i1}} \qquad 2.2$$

While the slope efficiency indicates approximately how much power the lasers can produce for every ampere of I_i, the WPE represents the total electrical-to-optical power conversion rate. The WPE is a figure of merit measured in percentage, which is defined as the ratio of optical output power to consumed electrical input power at wall plug:

$$WPE\ (\%) = \frac{P_{out}}{I_i * V} * 100\% \qquad 2.3$$

where P_{out} and V are the corresponding output power and the voltage level at a certain injected level (I_i). It should be mentioned that the real-life losses in the power supply and the power required for the colling system are not considered. Meanwhile, the *I-V* curve shows a nearly linear relationship between voltage and the I_i and, hence, the series resistance (R_s) of laser device can be obtained by simply using the equation [25]:

$$R_s = \frac{\Delta V}{\Delta I_{i2}} \qquad 2.4$$

The parameter R_s offers a direct assessment of the quality of metallisation depositions. Overall, an optimised laser should be capable of providing a low I_{th}, small R_s, and high η simultaneously for a given injected power.
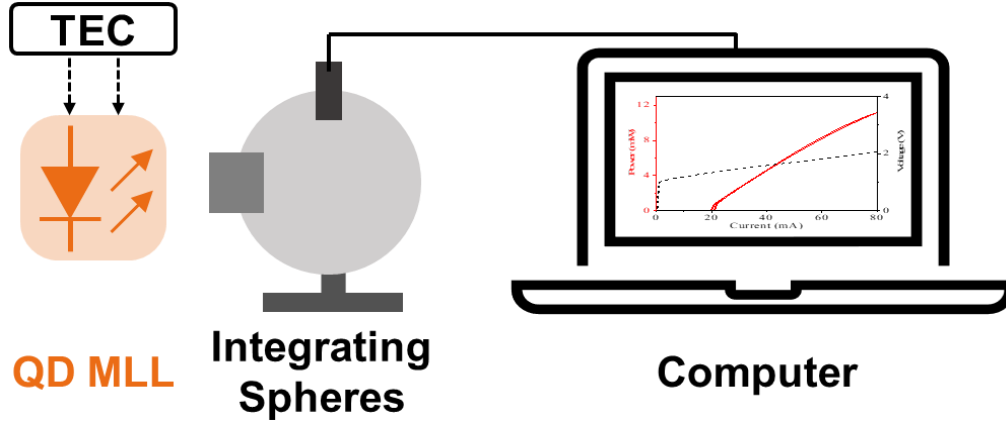
Figure 2.15 The schematic diagram of the L-I-V measurement setup.
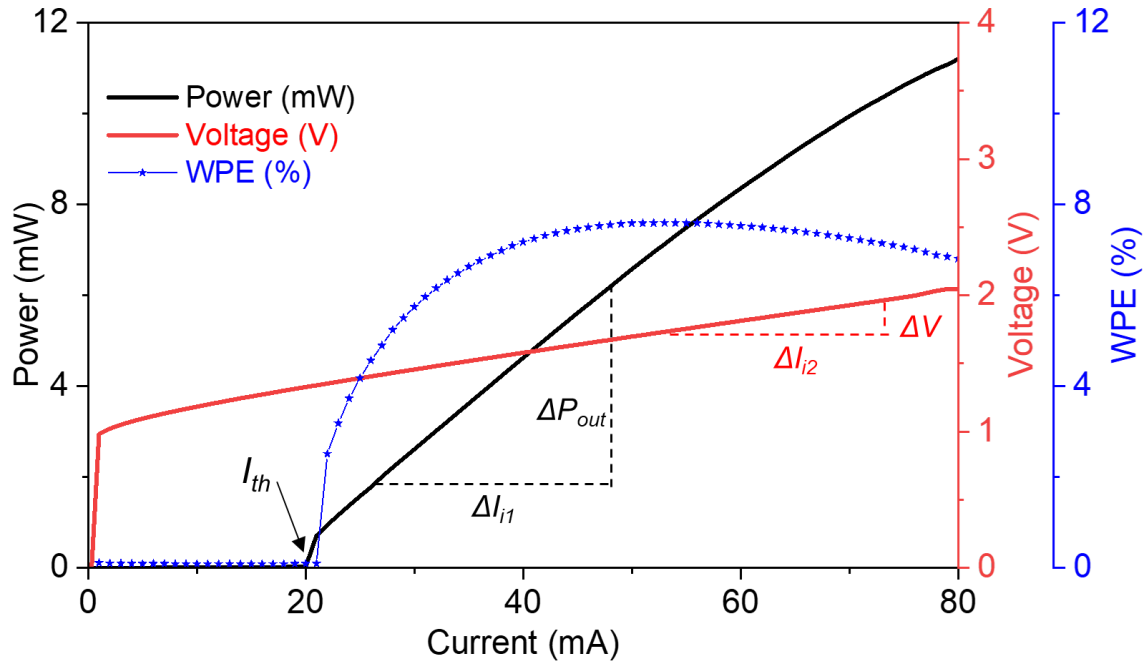
Figure 2.16 Typical C.W. light (black), voltage (red), and WPE (blue) vs current curves for a two-section GaAs/InAs QD-MLL at room temperature. The power and WPE values are measured from a single facet.

Moreover, a series of temperature-dependent *L-I* curves can be obtained by varying the TEC set point. Figure 2.17 (a) shows experimentally measured *L-I* curves of a narrow ridge GaAs laser at various heatsink temperatures ranging from 20 °C to 125 °C. Although it is widely accepted that the theoretical QD structure exhibits greater resistance to temperature effects compared with their QW or bulk counterparts (as discussed in Chapter 1) [7, 64]. It can be observed that the working temperature still poses considerable influence on semiconductor QD

lasers, where the I_{th} increases with elevated operating temperature while the η and the P_{out} drop significantly at the same time (detailed discussion of this phenomenon will be given in Chapter 3). The characteristic temperature of the laser device, denoted by the symbol T_0, is used to describe the thermal sensitivity of the device [65]. The value of T_0 is determined by plotting the J_{th} against temperature on a logarithmic as displayed in Fig. 2.17 (b). The slope of the linear fitted line yields the exact value of T_0 [62]:

$$T_0 = \frac{\Delta T}{\Delta\ ln(J_{th})}$$

2.5

A higher value of T_0 implies that the J_{th} increases at a slower rate with the temperature increment, i.e., the device is more thermally stable. It is desirable for most semiconductor devices in various applications to withstand degradation at high operating temperatures.
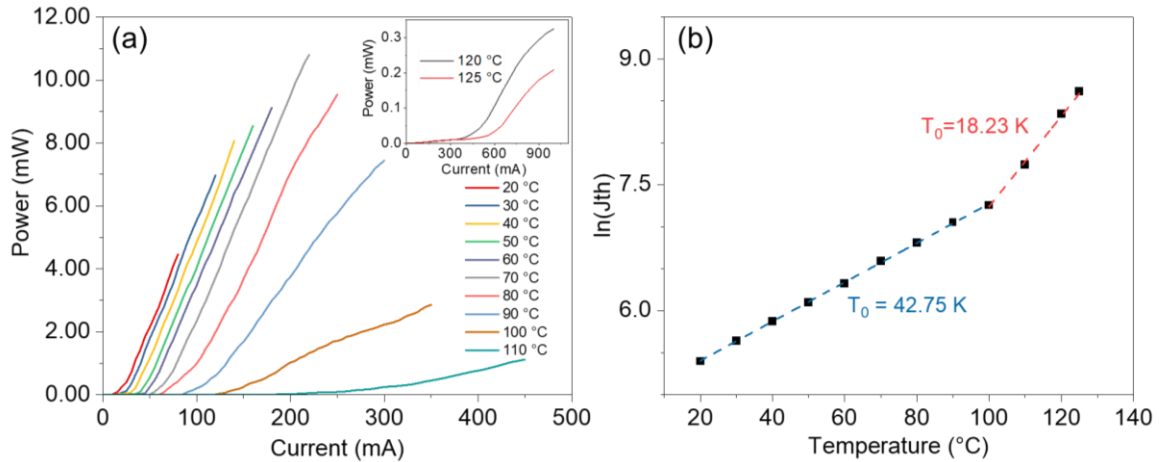
Figure 2.17 (a) The temperature-dependent L-I curves for a narrow ridge GaAs laser under pulsed-wave operation. (b) The plot of the natural logarithm of J_{th} against various temperatures with linear fitted lines (dash).

2.3.2 Mode-locking Characteristics

The fundamental mode-locking characteristics of two-section InAs/GaAs QD-MLLs are investigated using the setup shown in Fig. 2.18. Light coupling is achieved with an anti-reflection (AR) coated lensed fibre with a working distance of about 26 μm and a spot-size of 5 μm. The fibre is fixed on a manual x-y-z translation stage that

has pitch, roll, and yaw angular adjustments for maximum butt-coupling efficiency. An optical isolator is used immediately after the fibre to prevent undesired self-oscillation and reflections. The light source is then split with the standard fibre coupler with an optical power-split ratio of either 50/50 or 90/10 to enable synchronous measurements of multiple parameters, which is particularly important for mapping experiments.
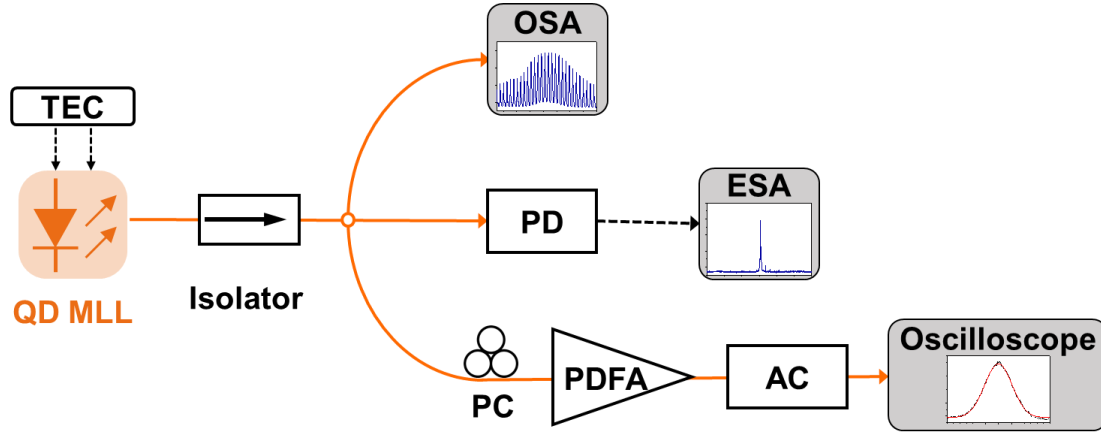
Figure 2.18 Experimental setup for mode-locking characteristics. OSA, optical spectrum analyser; PD, photodetector; ESA, electrical spectrum analyser; PC, polarisation controller; PDFA, praseodymium-doped fibre amplifier; AC, autocorrelator.

Optical spectra measurement

The emission spectra are recorded by the optical spectrum analyser (OSA), and two different equipment, depending on the required accuracy, are involved: the Yokogawa AQ6317B with a minimum resolution of 0.02 nm and the AP2087A with a minimum resolution of 0.04 pm.

Figure 2.19 (a) gives an example of the emission spectrum of a two-section QD-MLL with an 0.02 nm OSA resolution bandwidth. It visualises parameters like the centre-wavelength (λ_{centre}) and the 3dB optical bandwidth (also known as the FWHM). In the mode-locking regime, the locking between longitudinal modes substantially broadens the FWHM of the OSA spectrum [66]. Therefore, the observation of spectral changes allows us to roughly locate the mode-locking regime. The centre of the FWHM is defined as the λ_{centre}, which can be influenced

by the operation temperature and the mutual interference between the I_i and the V_{rev}. Generally, a red-shift of the λ_{centre} occur at a high operation temperature or with an increased I_i, and the discussion of those tendencies can be found in Chapters 3 and 4. The zoom-in OSA spectrum shown in Fig. 2.19 (b) enables a clearer sight of the mode-spacing ($\Delta\lambda$) between the adjacent modes. As already mentioned in Chapter 1, the $\Delta\lambda$ is directly decided by the L_{cavity}, which corresponds to the f_{rep} that will be later confirmed by the RF measurements. The number of combs within the 3dB bandwidth can be expressed as:

$$No. of\ combs = \frac{3dB\ bandwidth}{\Delta\lambda} \qquad 2.6$$

This is a crucial parameter to estimate the optical transmission capability of the devices [67, 68]. Another important parameter to evaluate the signal quality for optic communication is the optical signal-to-noise ratio (OSNR), which allows us to quantify the amplified spontaneous emission (ASE) noise-induced signal degradation in dynamic transmissions [69, 70]. Under the assumption of a 0.1 nm measurement bandwidth, the value of the OSNR in an optical channel can be approximately deduced using the following equations [71]:

$$P_{Ni} = \frac{P_{NL} + P_{NR}}{2} \qquad 2.7$$

$$P_{Signal} = P_{s+Ni} - P_{Ni} \qquad 2.8$$

$$OSNR = 10 * log\left(\frac{P_{Signal}}{P_{Ni}}\right) \qquad 2.9$$

$$OSNR(dB) = P_{Signal}(dBm) - P_{Ni}(dBm) \qquad 2.10$$

where P_{Ni} is the ASE noise level inside the optical channel, defining the mid-point between adjacent tones (P_{NL} and P_{NR}), and P_{Signal} is the signal power within the measured bandwidth. In optical transmission systems, the receivers require a sufficient level of OSNR to distinguish signals from the noise, and therefore the commonly accepted OSNR value should be greater than 15 dB [72].
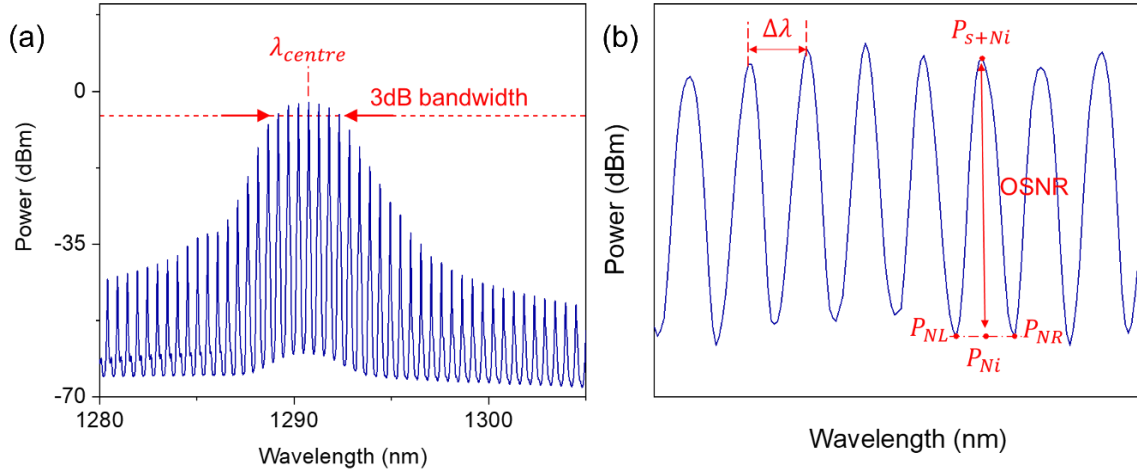
Figure 2.19 (a) Emission spectrum of a two-section QD-MLL with 0.02 nm resolution. (b) Zoom-in OSA spectrum of (a).

RF spectra measurement

To verify the f_{rep} of the device on an RF spectrum analyser, the output light from the laser must first be converted into an electric signal. In our work, a 50 GHz bandwidth photodetector (PD) (Finisar XPDV2320R) was chosen to connect to a 50 GHz RF spectrum analyser (Rohde & Schwarz FSW50) for revealing the precise value of f_{rep}.

Figure 2.20 presents typical RF spectra of a 25.54 GHz two-section QD-MLL in (a) 26.5 GHz span view (RBW: 1 MHz, VBW: 10 kHz.) and (b) 500 MHz span view (RBW: 1 kHz, VBW: 10 Hz). The fundamental RF tone at 25.54 GHz can be easily observed in Fig. 2.20 (a), but the higher-order frequency components of the device are beyond the measurement range of our RF spectral analyser and not detectable within our RF spectral measurements. Here, the signal strength at f_{rep} is defined as the P_{Signal}, and the unwanted background noise is defined as the P_{Noise}. Considering the noise fluctuations that occur during the entire measurement, the background noise level is quantified as the root-mean-square (RMS) value of low-frequency components (e.g., ranging from 2 Hz to 20 GHz).

$$P_{Noise} = P_{RMS(low-frequency)} = \sqrt{\frac{\sum_i^n (P_i)^2}{n-i}} \qquad 2.11$$

The RF signal-to-noise ratio (SNR), which indicates the difference between the signal strength and the background noise, can therefore be expressed as follows [73]:

$$SNR = 10\ log\left(\frac{P_{Signal}}{P_{Noise}}\right) \qquad 2.12$$

$$SNR\ (dB) = P_{Signal}(dBm) - P_{Noise}\ (dBm) \qquad 2.13$$

As an essential specification, the SNR at f_{rep} should maintain a minimum value of 25 dB to successfully distinguish the applied signals as legitimate information from any background noise on the spectrum [74, 75]. Moreover, the linewidth of the fundamental RF tone, also known as the RF FWHM, can be easily determined by fitting the measured data with the Lorentzian function (as shown in Fig. 2.20 (b)). The level of RF linewidth is associated with the RF phase noise and the timing jitter of the MLL. A narrow RF linewidth usually indicates a great phase correlation between the cavity modes [76-78].
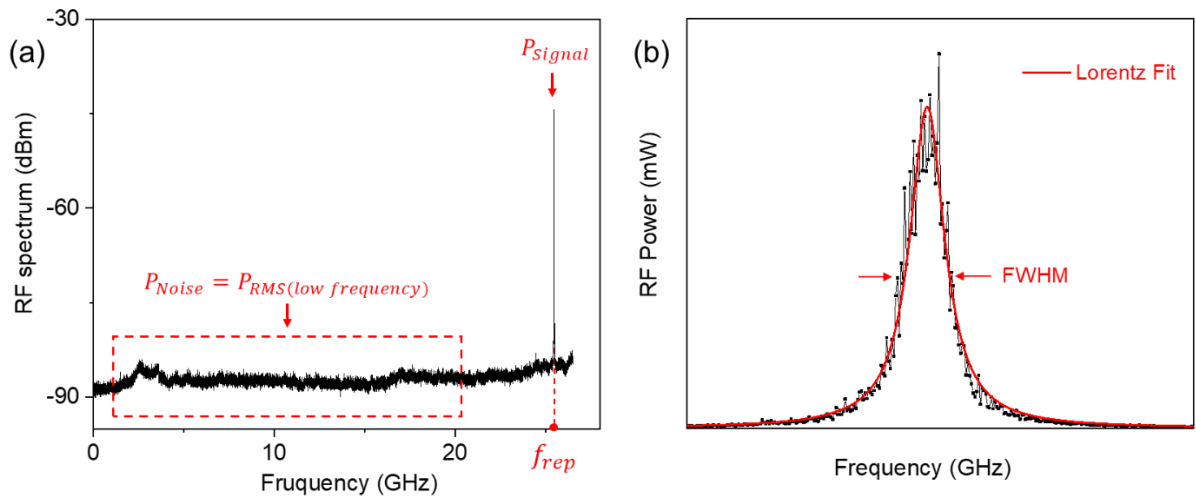
Figure 2.20 Measured RF spectra of a 25.54 GHz two-section QD-MLL in (a) 26.5 GHz span view and (b) 500MHz span view.

Autocorrelation measurement

Because of the slow response time (> 10 ps) of conventional electrical PDs, the most common second-order intensity autocorrelation method is employed in this work to determine the ultrashort pulse duration (τ_{pulse}) that lies within the range of picosecond (ps) to femtosecond (fs) [79, 80]. The working principle of an intensity autocorrelator (AC) (Femtochrome FR-103XL) is illustrated in Fig. 2.21. The incident pulse is divided into two identical pulses by a beam splitter first, one of which is returned from the corner mirror, and the other is delayed by rotating mirrors. The second-harmonic generation (SHG) signal is then generated by superimposing two pulses in an SHG crystal and systematically varying the temporal delay between them [81]. Finally, the SHG beam is detected by a highly sensitive photomultiplier (PMT) detector. The total amount of SHG detected is proportional to the product of the intensities of the two initial pulses, and therefore it is possible to deduce the τ_{pulse} of the incident pulse once the pulse shape is assumed (e.g., Gaussian or sech^2) [82-84].

As shown in Fig. 2.18, after the isolator, the output light is coupled into a polarisation controller (PC), a praseodymium-doped fibre amplifier (PDFA) (FiberLabs AMP-FL8611-16dB), and finally sent into an AC and monitored on an optical oscilloscope (Keysight DSOX3034T). The PC is used to modify the polarisation state of light before the AC, while the PDFA is used to maintain the carrier power at ~5 dBm level. The typically measured autocorrelation trace of a two-section GaAs/InAs QD-MLL is presented in Fig. 2.22, where the time interval between the pulses (ΔT_{ac}) corresponds to the cavity round-trip (T_{RT}). Hence, the calibration factor of the AC can be determined by the followed equation, with a unit of ps/ms.

$$F_{ac} = \frac{T_{RT}}{\Delta T_{ac}} = \frac{1}{f_{rep} * \Delta T_{ac}} \left(\frac{ps}{ms}\right) \qquad 2.14$$

The FWHM of the autocorrelation traces (i.e., the τ_{ac}) can be evaluated with nonlinear curve fitting under the assumption of certain pulse shapes like hyperbolic

secant, Lorentzian or Gaussian [85]. According to the chosen pulse shape, a pulse-shape factor ($\xi_{pulse-shape}$) should be applied when converting the measured τ_{ac} to the actual τ_{pulse} [85]. For a Gaussian pulse profile, the value of $\xi_{pulse-shape}$ equals to 0.707, and this value equals to 0.648 for a sech^2 pulse profile [86]. Consequently, the actual τ_{pulse} can be determined using the following formula:

$$\tau_{pulse} = \tau_{ac} * F_{ac} * \xi_{pulse-shape} \qquad 2.15$$

The TBP value under this condition is defined as the product of τ_{pulse} and its corresponding optical spectrum FWHM [87]:

$$TBP = \tau_{pulse} * FWHM_{OSA} \qquad 2.16$$

As already discussed in Chapter 1, the calculated TBP could reflect the chirp present in the pulse train, indicating the degree to which a pulse is transform-limited [88]
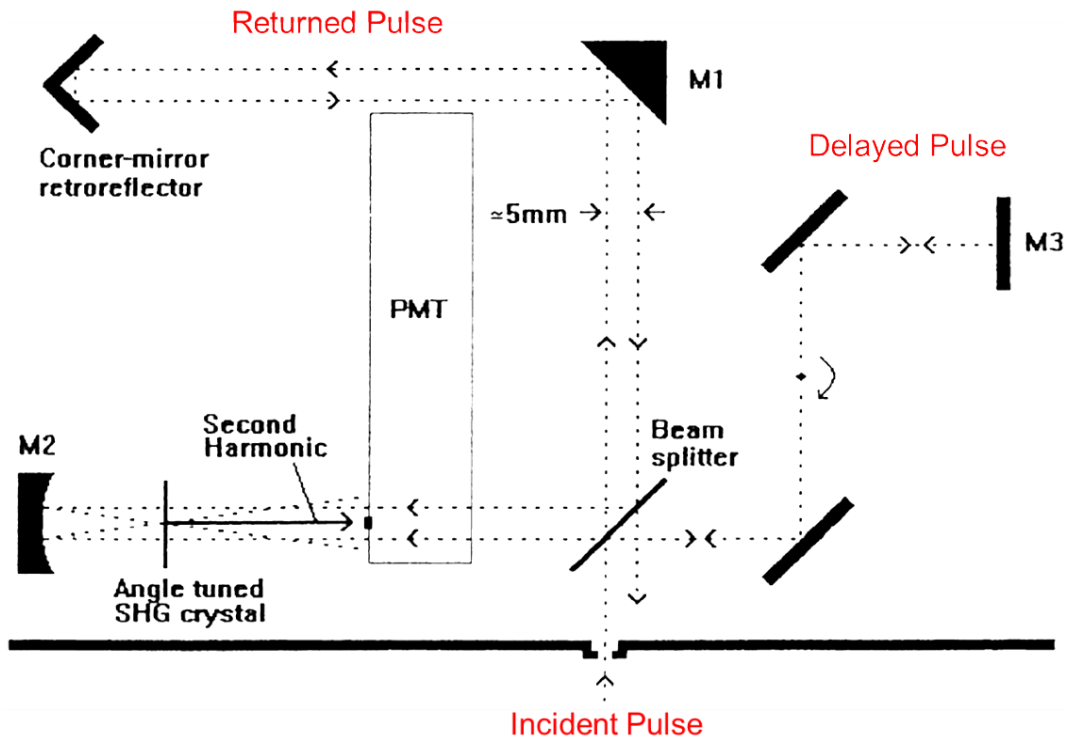
Figure 2.21 Top view schematic of AC FR-103XL [86].
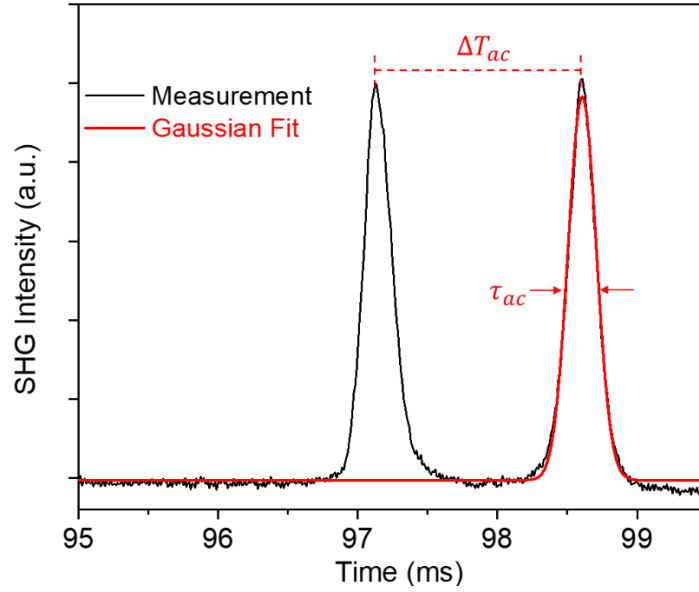
Figure 2.22 Autocorrelation trace measured for a 25.54 GHz two-section GaAs/InAs QD-MLL.

2.3.3 Noise Figure

The noise performance of an MLL is crucial for most applications, and it is particularly important for realizing high-speed data transmission systems [89]. The experimental setup for the two most common noise indicators is presented in this section: the phase noise and the RIN.
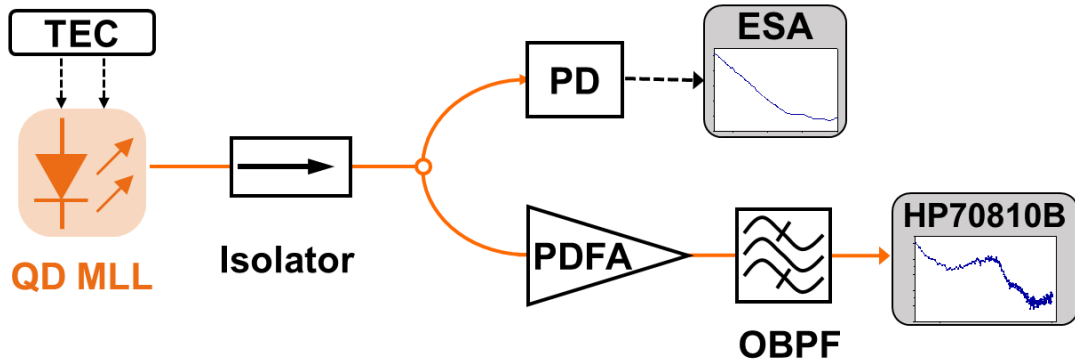
Figure 2.23 Experimental setup for noise characterisation.

Phase Noise

The phase noise is defined as the ratio of the noise arising in a 1-Hz bandwidth at a specified frequency offset, normally presenting as the single-sideband (SSB)

phase noise spectral density ($L_{(f)}$) in $\mathrm{dBc/Hz}$ [90, 91]. It refers to the short-term random fluctuations in the phase of an output signal in the frequency domain that is equivalent to the timing jitter or phase jitter in the time domain [92]. As can be found in Fig. 2.23, the experimental setup for assessing phase noise is identical to that used in RF spectrum measurement. The measured $L_{(f)}$ is usually plotted as a function of offset frequency with the frequency axis on a log scale (shown in Fig. 2.24). For a specific range of offset frequency (e.g., from f_i to f_x), the integrated phase noise can be presented as the area under the corresponding curve (A). The value of A can be obtained from Equation 2.17. Assuming that the noise profile is symmetrical, the rms value of timing jitter in radians can be deduced from the relationship shown in Equation 2.18, which can be further converted in seconds (Equation 2.19).

$$A\ (dBc) = \int_{f_i}^{f_x} L_{(f)} df = L_{(f_i)} + 10 * log(f_x - f_i) \qquad 2.17$$

$$RMS_{timing\ jitter}(rad) = \sqrt{2 * 10^{\left(\frac{A}{10}\right)}} \qquad 2.18$$

$$RMS_{timing\ jitter}(sec) = \frac{RMS_{timing\ jitter}(rad)}{2 * \pi * f_c} \qquad 2.19$$

where f_c is the carrier frequency of the oscillator. Normally, the fundamental harmonic is used for the phase noise evaluation, and hence the f_c can be treated as f_{rep} [93]. Moreover, the relatively flat section at high offset frequency represents the noise floor, indicating the unbounded random jitter. This is mainly attributed to the thermal noise, which is likely to be the major contributor to the overall jitter level [94-96].
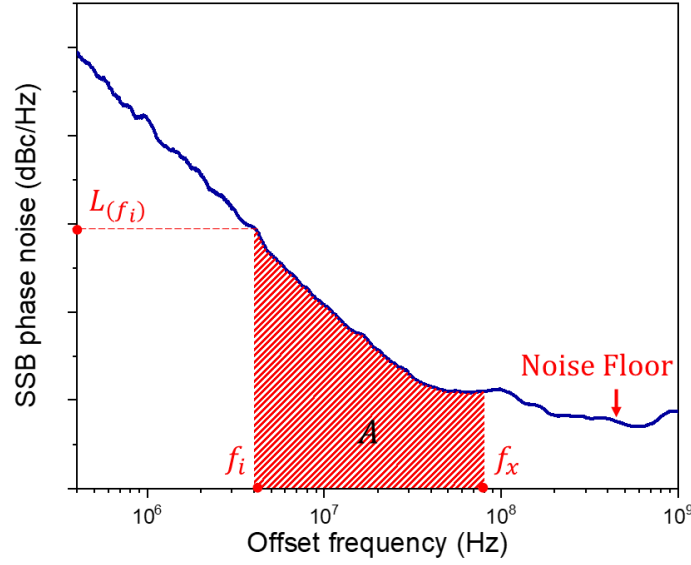
Figure 2.24 Typical SSB phase noise plot of a two-section GaAs/InAs QD-MLL.

Relative intensity noise (RIN)

The RIN describes the instability in the output power of a semiconductor laser, which is usually expressed as the ratio of the mean square fluctuations in optical power ($< \Delta P^2 >$) in a 1-Hz bandwidth to the square of the average optical power (P_0^2) [97-99].

$$RIN \ (dB/Hz) = \frac{< \Delta P^2 >}{P_0^2} \qquad 2.20$$

It has been widely adopted as an essential figure of merit to estimate the device performance in optical transmission networks since it can pose limitations on the SNR and the BER [100-102]. The setup for RIN measurement is performed in Fig. 2.23. After light passes through the optical isolator, a PDFA is used to amplify the output power from +5 dBm to around +20 dBm. This is crucial to compensate for the large loss (~ 10 dB) induced by the tunable optical bandpass filter (OBPF) with adjustable bandwidth (EXFO XTM-50). The employment of the OBPF allows us to precisely select individual tones and suppress the out-of-band amplified spontaneous emission (ASE) noise from the PDFA [103]. Then, the filtered comb is collected by a built-in PD installed in the HP70810B lightwave section. After the

PD, the generated photocurrent is split into two paths: one as the DC component to determine the average optical power, and the other as the AC component to detect the amplified noise spectrum by the electrical spectrum analyser (ESA) [104-106]. The RIN simplifies the ratio of AC to DC electrical powers [97]. It should be mentioned that in the RIN measurement of the whole lasing spectrum, neither OBPF nor PDFA is used.

Figure 2.25 exhibits a representative high-frequency RIN spectrum of a two-section GaAs/InAs QD-MLL, with a peak at the so-called relaxation oscillation frequency (f_{ro}) which falls off at higher frequencies until it convergences to the shot noise limit [107]. The well-defined f_{ro} results from the dynamic interaction of the intracavity power, the carrier lifetime, the resonator losses, and the laser gain, and this parameter allows us to deduce the maximum intrinsic modulation bandwidth of the laser device [97]. Attention should be paid to measuring total RIN which normally contains thermal noise (i_{th}), shot noise (i_{sh}) as well as the laser intensity noise (i_{laser}) [108]. The thermal noise comes from the Brownian movement of particles by the thermal energy while the shot noise is due to the quantum nature of light that incident on the photodetector. Hence, the actual laser RIN level is always lower than the measured value.
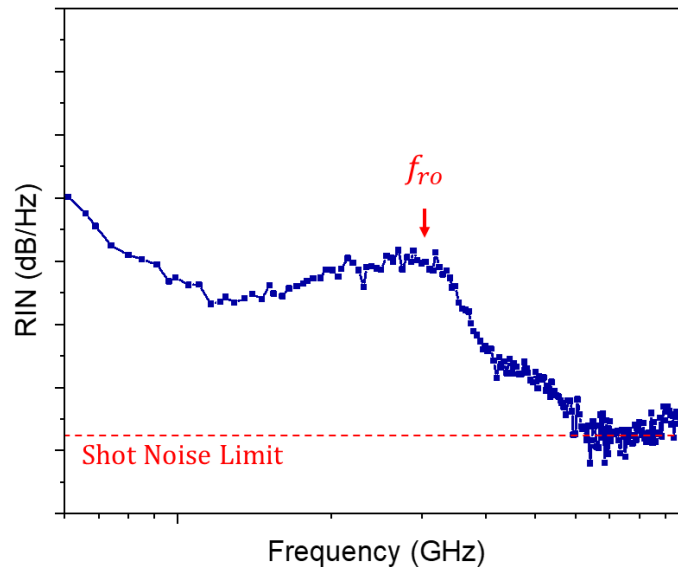
Figure 2.25 Typical high-frequency RIN spectrum of a two-section GaAs/InAs QD-MLL.

2.3.4 System-level transmission

To assess the optical transmission ability of our devices, a system-level experimental setup is implemented (shown in Fig. 2.26). The device is first packaged into a standard 14-pin butterfly-package on top of a TEC, which allows for achieving stable and reproducible results. Next, the desired wavelength channel is filtered out by an OBPF as an optical carrier. A PDFA is followed to boost the carrier power up to ~13 dBm. Normally, another OBPF is needed to remove the out-of-band ASE noise [67]. However, in our case, no additional OBPF is utilised due to the large loss induced by the OBPF. The amplified optical carrier signal is then launched into a 40 GHz lithium niobate Mach-Zehnder modulator (MZM) (iXblue MX1300-LN-40) for data modulation. Prior to the MZM, a polarisation controller (PC) is required to determine the polarisation direction of the input lightwave and enable maximum signal intensity. A pseudo-random bit sequence (PRBS) with PAM-4 or NRZ format is generated offline in MATLAB and loaded to a 120 GSa/s arbitrary waveform generator (AWG) (Keysight M8194A), after which the generated electrical signal is amplified by an RF amplifier (SHF 807C) with a 3-dB bandwidth of 55 GHz. Subsequently, the modulated optical signal is transmitted for back-to-back (B2B) configuration, over 5-km SSMF, and 2-m free-space, respectively. At the receiver side, a variable optical attenuator (VOA) is used to control the optical power received by a 50 GHz PD (Finisar XPDV2320R). The detected signal from the PD is later amplified by another RF amplifier and digitally captured by a real-time digital storage oscilloscope (DSO) with a sampling rate of 256 GSa/s (Keysight UXR0704A). Eventually, offline digital signal processing (DSP) is applied for signal recovery and BER calculation.

$$BER = \frac{Number\ of\ errors\ received}{Total\ number\ of\ transmitted\ bits} \qquad 2.21$$

At the transmitter DSP (Tx-DSP) side, nonlinear compensation (NLC) is firstly carried out to pre-compensate the modulation nonlinearity for the PAM-4 symbols while skipped for the NRZ signal [109]. After that, the generated high-baud-rate PRBS-15 is up-sampled and a root-raised-cosine (RRC) filter with a roll-off factor

of 0.6 is applied to the signal for pulse-shaping purposes. Finally, the down-sampled signal carries out a pre-compensation step, in which the whole system's end-to-end frequency response is compensated. At the receiver DSP side (Rx-DSP), the captured data are initially re-sampled to two samples per symbol and a matched RRC filter is executed to reduce the impact of white noise [68]. Thereafter, the data sequence is down-sampled to one sample per symbol and synchronised with the original bitstream that is loaded to the AWG. The potential carrier frequency offset between the transmitter and receiver is compensated in the clock recovery process. A 51-tap feed-forward equaliser (FFE) with the least mean squares (LMS) algorithm is applied to eliminate the inter-symbol-interference (ISI) and restore the signal in high-speed transmission. Finally, the output PAM-4/OOK signal is decoded for BER calculations.
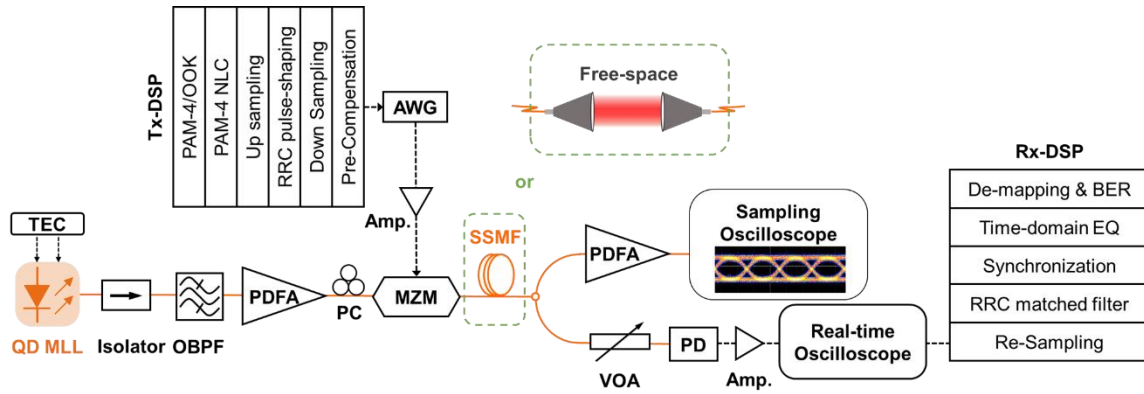
Figure 2.26 Schematic setup for system-level data transmission.

While the BER results quantify the transmission performance of received signals, optical eye diagrams resulting from the superposition of bit periods give a visualisation of actual optical waveforms [110]. In our work, the optical eye diagrams of the received signals were measured using the sampling oscilloscope (Keysight DCA-M N1092A) immediately after the modulator. The Q-factor obtained from the optical eye diagrams can be used to derive the corresponding BER values, as given by [111-113]:

$$BER = \frac{1}{2} erfc\left(\frac{Q}{\sqrt{2}}\right)$$

2.22

96

It should be noted that a second PDFA is added between the MZM and the sampling oscilloscope to enhance the signal with sufficient power (~ +5 dBm) and, hence, obtain good quality eye diagrams.

2.4 Reference

[1]   R. Pelzel, "A comparison of MOVPE and MBE growth technologies for III-V epitaxial structures," in *CS MANTECH Conference*, 2013: New Orleans Louisiana, USA, pp. 105-108.

[2]   A. Cho, "Recent developments in molecular beam epitaxy (MBE)," *Journal of Vacuum Science and Technology,* vol. 16, no. 2, pp. 275-284, 1979.

[3]   A. Cho, "Advances in molecular beam epitaxy (MBE)," *Journal of crystal growth,* vol. 111, no. 1-4, pp. 1-13, 1991.

[4]   K. Kosiel, "MBE—Technology for nanoelectronics," *Vacuum,* vol. 82, no. 10, pp. 951-955, 2008.

[5]   M. Cusack, P. Briddon, and M. a. Jaros, "Electronic structure of InAs/GaAs self-assembled quantum dots," *Physical Review B,* vol. 54, no. 4, p. R2300, 1996.

[6]   S. Adhikary *et al.*, "Investigation of strain in self-assembled multilayer InAs/GaAs quantum dot heterostructures," *Journal of crystal growth,* vol. 312, no. 5, pp. 724-729, 2010.

[7]   K. Nishi, K. Takemasa, M. Sugawara, and Y. Arakawa, "Development of quantum dot lasers for data-com and silicon photonics applications," *IEEE Journal of Selected Topics in Quantum Electronics,* vol. 23, no. 6, pp. 1-7, 2017.

[8]   J. Tatebayashi, M. Nishioka, and Y. Arakawa, "Over 1.5 µm light emission from InAs quantum dots embedded in InGaAs strain-reducing layer grown by metalorganic chemical vapor deposition," *Appl Phys Lett,* vol. 78, no. 22, pp. 3469-3471, 2001.

[9]   K. Nishi, H. Saito, S. Sugou, and J.-S. Lee, "A narrow photoluminescence linewidth of 21 meV at 1.35 µm from strain-reduced InAs quantum dots covered by In 0.2 Ga 0.8 As grown on GaAs substrates," *Appl Phys Lett,* vol. 74, no. 8, pp. 1111-1113, 1999.

[10]   A. Salhi *et al.*, "Linear increase of the modal gain in 1.3 µm InAs/GaAs quantum dot lasers containing up to seven-stacked QD layers," *Nanotechnology,* vol. 19, no. 27, p. 275401, 2008.

[11]   W. Kern, "Handbook of semiconductor wafer cleaning technology," *New Jersey: Noyes Publication,* pp. 111-196, 1993.

[12]   T. Ishihara and X. Luo, "Chapter 17 - Nanophotolithography based on surface plasmon interference," in *Handai Nanophotonics*, vol. 2, S. Kawata and H. Masuhara Eds.: Elsevier, 2006, pp. 305-312.

[13]   L. W. Liebmann, S. M. Mansfield, A. K. Wong, M. A. Lavin, W. C. Leipold, and T. G. Dunham, "TCAD development for lithography resolution enhancement," *IBM Journal of Research and Development,* vol. 45, no. 5, pp. 651-665, 2001.

[14]   Y. Zhang, C. Liu, and D. Whalley, "Direct-write techniques for maskless production of microelectronics: A review of current state-of-the-art technologies," in *2009 International Conference on Electronic Packaging Technology & High Density Packaging*, 2009: IEEE, pp. 497-503.

[15]   K. Nojiri, *Dry etching technology for semiconductors*. Springer, 2015.

[16]   H. Boenig, *Plasma science and technology*. Cornell University Press, 2019.

[17]   P. Chabert and N. Braithwaite, *Physics of radio-frequency plasmas*. Cambridge University Press, 2011.

[18]   V. M. Donnelly and A. Kornblit, "Plasma etching: Yesterday, today, and tomorrow," *Journal of Vacuum Science & Technology A: Vacuum, Surfaces, and Films,* vol. 31, no. 5, p. 050825, 2013.

[19]   M. A. Lieberman and A. J. Lichtenberg, *Principles of plasma discharges and materials processing*. John Wiley & Sons, 2005.

[20]   F. F. Chen and J. P. Chang, *Lecture notes on principles of plasma processing*. Springer Science & Business Media, 2003.

[21]   N. Negishi, H. Takesue, M. Sumiya, T. Yoshida, Y. Momonoi, and M. Izawa, "Deposition control for reduction of 193 nm photoresist degradation in dielectric etching," *Journal of Vacuum Science & Technology B: Microelectronics and Nanometer Structures Processing, Measurement, and Phenomena,* vol. 23, no. 1, pp. 217-223, 2005.

[22]   D. Nest *et al.*, "Synergistic effects of vacuum ultraviolet radiation, ion bombardment, and heating in 193 nm photoresist roughening and degradation," *Appl Phys Lett,* vol. 92, no. 15, p. 153113, 2008.

[23]   D. Tsvetanova *et al.*, "Degradation of 248 nm deep UV photoresist by ion implantation," *Journal of The Electrochemical Society,* vol. 158, no. 8, p. H785, 2011.

[24]   O. Joubert *et al.*, "Resist degradation under plasma exposure: Synergistic effects of ion bombardment," *Journal of applied physics,* vol. 69, no. 3, pp. 1697-1702, 1991.

[25]   S. M. Sze, Y. Li, and K. K. Ng, *Physics of semiconductor devices*. John wiley & sons, 2021.

[26]   P. H. Holloway and G. E. McGuire, *Handbook of compound semiconductors: growth, processing, characterization, and devices*. Cambridge University Press, 2008.

[27]   R. Kiran *et al.*, "Effect of Atmosphere on n-Type Hg1–xCdxTe Surface after Different Wet Etching Treatments: An Electrical and Structural Study," *Journal of Electronic Materials,* vol. 37, no. 9, pp. 1471-1479, 2008/09/01 2008, doi: 10.1007/s11664-008-0494-4.

[28]   J.-H. Kim, D. H. Lim, and G. M. Yang, "Selective etching of AlGaAs/GaAs structures using the solutions of citric acid/H 2 O 2 and de-ionized H 2 O/buffered oxide etch," *Journal of*

Vacuum Science & Technology B: Microelectronics and Nanometer Structures Processing, Measurement, and Phenomena, vol. 16, no. 2, pp. 558-560, 1998.

[29]   C. Juang, K. Kuhn, and R. Darling, "Selective etching of GaAs and Al0. 30Ga0. 70As with citric acid/hydrogen peroxide solutions," *Journal of Vacuum Science & Technology B: Microelectronics Processing and Phenomena,* vol. 8, no. 5, pp. 1122-1124, 1990.

[30]   G. C. DeSalvo, W. F. Tseng, and J. Comas, "Etch rates and selectivities of citric acid/hydrogen peroxide on GaAs, Al0. 3Ga0. 7As, In0. 2Ga0. 8As, In0. 53Ga0. 47As, In0. 52Al0. 48As, and InP," *Journal of The Electrochemical Society,* vol. 139, no. 3, p. 831, 1992.

[31]   H. Abe, M. Yoneda, and N. Fujiwara, "Developments of plasma etching technology for fabricating semiconductor devices," *Japanese Journal of Applied Physics,* vol. 47, no. 3R, p. 1435, 2008.

[32]   M. Sugawara, *Plasma etching: fundamentals and applications*. OUP Oxford, 1998.

[33]   M. Huff, "Recent Advances in Reactive Ion Etching and Applications of High-Aspect-Ratio Microfabrication," *Micromachines,* vol. 12, no. 8, p. 991, 2021.

[34]   H. Jansen, H. Gardeniers, M. de Boer, M. Elwenspoek, and J. Fluitman, "A survey on the reactive ion etching of silicon in microtechnology," *Journal of micromechanics and microengineering,* vol. 6, no. 1, p. 14, 1996.

[35]   V. Vahedi, C. Birdsall, M. Lieberman, G. DiPeso, and T. Rognlien, "Verification of frequency scaling laws for capacitive radio-frequency discharges using two-dimensional simulations," *Physics of Fluids B: Plasma Physics,* vol. 5, no. 7, pp. 2719-2729, 1993.

[36]   M. Moravej, X. Yang, M. Barankin, J. Penelon, S. Babayan, and R. Hicks, "Properties of an atmospheric pressure radio-frequency argon and nitrogen plasma," *Plasma Sources Science and Technology,* vol. 15, no. 2, p. 204, 2006.

[37]   T. Okumura, "Inductively coupled plasma sources and applications," *Physics Research International,* vol. 2010, 2010.

[38]   G. Oehrlein, J. Rembetski, and E. Payne, "Study of sidewall passivation and microscopic silicon roughness phenomena in chlorine-based reactive ion etching of silicon trenches," *Journal of Vacuum Science & Technology B: Microelectronics Processing and Phenomena,* vol. 8, no. 6, pp. 1199-1211, 1990.

[39]   B. Wu, A. Kumar, and S. Pamarthy, "High aspect ratio silicon etch: A review," *Journal of applied physics,* vol. 108, no. 5, p. 9, 2010.

[40]   J. Lee, K. Mackenzie, D. Johnson, J. Sasserath, S. Pearton, and F. Ren, "Low temperature silicon nitride and silicon dioxide film processing by inductively coupled plasma chemical vapor deposition," *Journal of The Electrochemical Society,* vol. 147, no. 4, p. 1481, 2000.

[41]   Y.-B. Park and S.-W. Rhee, "Low temperature silicon dioxide film deposition by remote plasma enhanced chemical vapor deposition: growth mechanism," *Surface and Coatings Technology,* vol. 179, no. 2-3, pp. 229-236, 2004.

[42]   S. Tinck and A. Bogaerts, "Modeling SiH4/O2/Ar inductively coupled plasmas used for filling of microtrenches in shallow trench isolation (STI)," *Plasma Processes and Polymers,* vol. 9, no. 5, pp. 522-539, 2012.

[43]   A. Boogaard *et al.*, "Characterization of SiO2 films deposited at low temperature by means of remote ICPECVD," *Surface and Coatings Technology,* vol. 201, no. 22-23, pp. 8976-8980, 2007.

[44]   E. H. Rhoderick, "Metal-semiconductor contacts," *IEE Proceedings I-Solid-State and Electron Devices,* vol. 129, no. 1, p. 1, 1982.

[45]   V. Rideout, "A review of the theory and technology for ohmic contacts to group III–V compound semiconductors," *Solid-State Electronics,* vol. 18, no. 6, pp. 541-550, 1975.

[46]   A. Yu, "Electron tunneling and contact resistance of metal-silicon contact barriers," *Solid-state electronics,* vol. 13, no. 2, pp. 239-247, 1970.

[47]   H. Hoff *et al.*, "Ohmic contacts to semiconducting diamond using a Ti/Pt/Au trilayer metallization scheme," *Diamond and related materials,* vol. 5, no. 12, pp. 1450-1456, 1996.

[48]   H. Okada, S.-i. Shikata, and H. Hayashi, "Electrical characteristics and reliability of Pt/Ti/Pt/Au ohmic contacts to p-type GaAs," *Japanese journal of applied physics,* vol. 30, no. 4A, p. L558, 1991.

[49]   G. Stareev, "Formation of extremely low resistance Ti/Pt/Au ohmic contacts to p-GaAs," *Appl Phys Lett,* vol. 62, no. 22, pp. 2801-2803, 1993.

[50]   L. Zhou, W. Lanford, A. Ping, I. Adesida, J. Yang, and A. Khan, "Low resistance Ti/Pt/Au ohmic contacts to p-type GaN," *Appl Phys Lett,* vol. 76, no. 23, pp. 3451-3453, 2000.

[51]   B. Sehgal, B. Bhattacharya, S. Vinayak, and R. Gulati, "Thermal reliability of n-GaAs/Ti/Pt/Au Schottky contacts with thin Ti films for reduced gate resistance," *Thin Solid Films,* vol. 330, no. 2, pp. 146-149, 1998.

[52]   M. Todeschini, A. Bastos da Silva Fanta, F. Jensen, J. B. Wagner, and A. Han, "Influence of Ti and Cr adhesion layers on ultrathin Au films," *ACS applied materials & interfaces,* vol. 9, no. 42, pp. 37374-37385, 2017.

[53]   C. Chang, S. Murarka, V. Kumar, and G. Quintana, "Interdiffusions in thin-film Au on Pt on GaAs (100) studied with Auger spectroscopy," *Journal of Applied Physics,* vol. 46, no. 10, pp. 4237-4243, 1975.

[54]   T. Kim and P. Holloway, "Ohmic contacts to GaAs epitaxial layers," *Critical Reviews in Solid State and Material Sciences,* vol. 22, no. 3, pp. 239-273, 1997.

[55]   S. Chua, S. Lee, R. Gopalakrishnan, K. Tan, and T. Chong, "Investigation of the dependence of the contact resistance on the external gold layer in AuNiGeAu/n-GaAs," *Thin solid films,* vol. 200, no. 2, pp. 211-217, 1991.

[56]   P. Karbownik *et al.*, "Low resistance ohmic contacts to n-GaAs for application in GaAs/AlGaAs quantum cascade lasers," *Optica Applicata,* vol. 39, no. 4, p. 655, 2009.

[57]   M. Murakami, "Development of refractory ohmic contact materials for gallium arsenide compound semiconductors," *Science and Technology of Advanced Materials,* vol. 3, no. 1, pp. 1-27, 2002.

[58]   F. Vidimari, "Improved ohmic properties of Au-Ge contacts to thin n-GaAs layers alloyed with an SiO 2 overlayer," *Electron Lett,* vol. 15, no. 21, pp. 674-676, 1979.

[59]   M. Ogawa, "Alloying behavior of Ni/Au-Ge films on GaAs," *Journal of applied physics,* vol. 51, no. 1, pp. 406-412, 1980.

[60]   W. L. Chen, J. Cowles, G. Haddad, G. Munns, K. Eisenbeiser, and J. East, "Ohmic contact study for quantum effect transistors and heterojunction bipolar transistors with InGaAs contact layers," *Journal of Vacuum Science & Technology B: Microelectronics and Nanometer Structures Processing, Measurement, and Phenomena,* vol. 10, no. 6, pp. 2354-2360, 1992.

[61]   E. Erofeev, S. Ishutkin, V. Kagadei, and K. Nosaeva, "Multilayer low-resistance Ge/Au/Ni/Ti/Au based ohmic contact to n-GaAs," in *The 5th European Microwave Integrated Circuits Conference*, 2010: IEEE, pp. 290-293.

[62]   K. S. Mobarhan, "Test and characterization of laser diodes: determination of principal parameters," *Newport Corporation,* 1995.

[63]   W. T. Silfvast, *Laser fundamentals*. Cambridge university press, 2004.

[64]   Y. Arakawa and H. Sakaki, "Multidimensional quantum well laser and temperature dependence of its threshold current," *Appl Phys Lett,* vol. 40, no. 11, pp. 939-941, 1982.

[65]   P. Bhattacharya and Z. Mi, "Quantum-dot optoelectronic devices," *Proceedings of the IEEE,* vol. 95, no. 9, pp. 1723-1740, 2007.

[66]   Z. Wang *et al.*, "A III-V-on-Si ultra-dense comb laser," *Light: Science & Applications,* vol. 6, no. 5, pp. e16260-e16260, 2017.

[67]   S. T. Liu *et al.*, "High-channel-count 20 GHz passively mode-locked quantum dot laser directly grown on Si with 4.1 Tbit/s transmission capacity," (in English), *Optica,* vol. 6, no. 2, pp. 128-134, Feb 20 2019, doi: 10.1364/Optica.6.000128.

[68]   G. Liu *et al.*, "Passively mode-locked quantum dash laser with an aggregate 5.376 Tbit/s PAM-4 transmission capacity," *Optics express,* vol. 28, no. 4, pp. 4587-4593, 2020.

[69]   J. Lee, H. Choi, S. Shin, and Y. C. Chung, "A review of the polarization-nulling technique for monitoring optical-signal-to-noise ratio in dynamic WDM networks," *Journal of Lightwave Technology,* vol. 24, no. 11, pp. 4162-4171, 2006.

[70]   R. Antil, S. B. Pinki, and S. Beniwal, "An overview of DWDM technology & network," *Int. J. Sci. Technol. Res,* vol. 1, no. 11, pp. 43-46, 2012.

[71]   "OSNR: What does this mean;Why do we need and How to take care of it?" https://mapyourtech.com/entries/general/osnr-what-does-this-mean-why-do-we-need-and-how-to-take-care-of-it- (accessed.

[72]   S. Tibuleac and M. Filer, "Transmission impairments in DWDM networks with reconfigurable optical add-drop multiplexers," *Journal of Lightwave Technology,* vol. 28, no. 4, pp. 557-568, 2010.

[73]   "Understanding Frequency Performance Specifications." https://www.ni.com/en-gb/support/documentation/supplemental/06/understanding-frequency-performance-specifications.html (accessed.

[74]   R. G. Vaughan, N. L. Scott, and D. R. White, "The theory of bandpass sampling," *IEEE Transactions on signal processing,* vol. 39, no. 9, pp. 1973-1984, 1991.

[75]   S. Pan *et al.*, "Quantum dot mode-locked frequency comb with ultra-stable 25.5 GHz spacing between 20° C and 120° C," *Photonics Research,* vol. 8, no. 12, pp. 1937-1942, 2020.

[76]   K. Merghem *et al.*, "Stability of optical frequency comb generated with InAs/InP quantum-dash-based passive mode-locked lasers," *IEEE Journal of Quantum Electronics,* vol. 50, no. 4, pp. 275-280, 2014.

[77]   F. Kéfélian, S. O'Donoghue, M. T. Todaro, J. G. McInerney, and G. Huyet, "RF linewidth in monolithic passively mode-locked semiconductor laser," *Ieee Photonic Tech L,* vol. 20, no. 16, pp. 1405-1407, 2008.

[78]   R. Rosales *et al.*, "High performance mode locking characteristics of single section quantum dash lasers," *Opt Express,* vol. 20, no. 8, pp. 8649-8657, 2012.

[79]   B. D. Boruah, "Zinc oxide ultraviolet photodetectors: rapid progress from conventional to self-powered photodetectors," *Nanoscale Advances,* vol. 1, no. 6, pp. 2059-2085, 2019.

[80]   Y. Zhang, L. Wang, K. Wang, K. S. Wong, and K. Wu, "Recent advances in the hardware of visible light communication," *IEEE Access,* vol. 7, pp. 91093-91104, 2019.

[81]   R. Paschotta, *Field guide to laser pulse generation*. SPIE press Bellingham, 2008.

[82] E. Ippen and C. Shank, "Techniques for measurement," in *Ultrashort light pulses*: Springer, 1984, pp. 83-122.

[83] F. Salin, P. Georges, G. Roger, and A. Brun, "Single-shot measurement of a 52-fs pulse," *Applied optics,* vol. 26, no. 21, pp. 4528-4531, 1987.

[84] R. Trebino *et al.*, "Measuring ultrashort laser pulses in the time-frequency domain using frequency-resolved optical gating," *Review of Scientific Instruments,* vol. 68, no. 9, pp. 3277-3295, 1997.

[85] K. Sala, G. Kenney-Wallace, and G. Hall, "CW autocorrelation measurements of picosecond laser pulses," *IEEE Journal of Quantum Electronics,* vol. 16, no. 9, pp. 990-996, 1980.

[86] "FR-103MN AUTOCORRELATOR INSTRUCTION MANUAL." https://www.femtochrome.com/fr-103mn.html (accessed.

[87] F. C. Paez, *Comparative study of passive modelocking configurations in semiconductor lasers*. University of Glasgow (United Kingdom), 1997.

[88] K. Merghem *et al.*, "Pulse generation at 346 GHz using a passively mode locked quantum-dash-based laser at 1.55 µm," *Applied Physics Letters,* vol. 94, no. 2, p. 021107, 2009.

[89] J. Kim and Y. Song, "Ultralow-noise mode-locked fiber lasers and frequency combs: principles, status, and applications," *Adv. Opt. Photon.,* vol. 8, no. 3, pp. 465-540, 2016.

[90] W. P. Robins, *Phase noise in signal sources: theory and applications*. IET, 1984.

[91] A. Hajimiri and T. H. Lee, "A general theory of phase noise in electrical oscillators," *IEEE journal of solid-state circuits,* vol. 33, no. 2, pp. 179-194, 1998.

[92] T. C. Weigandt, B. Kim, and P. R. Gray, "Analysis of timing jitter in CMOS ring oscillators," in *Proceedings of IEEE International Symposium on Circuits and Systems-ISCAS'94*, 1994, vol. 4: IEEE, pp. 27-30.

[93] K. Yvind, *Semiconductor mode-locked lasers for optical communication systems*. COM, Technical University of Denmark, 2003.

[94] A. Hajimiri, S. Limotyrakis, and T. H. Lee, "Jitter and phase noise in ring oscillators," *IEEE Journal of Solid-state circuits,* vol. 34, no. 6, pp. 790-804, 1999.

[95] W. F. Egan, "Frequency synthesis by phase lock," *New York,* 1981.

[96] N. Da Dalt and A. Sheikholeslami, *Understanding Jitter and Phase Noise: A Circuits and Systems Perspective*. Cambridge University Press, 2018.

[97] G. E. Obarski and P. D. Hale, "How to measure relative intensity noise in lasers," *Laser Focus World,* vol. 35, pp. 273-278, 1999.

[98] C. Fludger, V. Handerek, and R. Mears, "Pump to signal RIN transfer in Raman fiber amplifiers," *Journal of Lightwave Technology,* vol. 19, no. 8, p. 1140, 2001.

[99] L. A. Coldren, S. W. Corzine, and M. L. Mashanovitch, *Diode lasers and photonic integrated circuits*. John Wiley & Sons, 2012.

[100] G. P. Agrawal, *Fiber-optic communication systems*. John Wiley & Sons, 2012.

[101] M. Liao *et al.*, "Low-noise 1.3 μm InAs/GaAs quantum dot laser monolithically grown on silicon," *Photonics Research,* vol. 6, no. 11, pp. 1062-1066, 2018.

[102] K. I. Kallimani and M. O'mahony, "Relative intensity noise for laser diodes with arbitrary amounts of optical feedback," *Ieee J Quantum Elect,* vol. 34, no. 8, pp. 1438-1446, 1998.

[103] X. Xu *et al.*, "Broadband RF channelizer based on an integrated optical frequency Kerr comb source," *Journal of Lightwave Technology,* vol. 36, no. 19, pp. 4519-4526, 2018.

[104] "Agilent 71400C, Lightwave Signal Analyzer, Product Overview." https://assets.testequity.com/te1/Documents/pdf/hp71400c.pdf (accessed.

[105] "User's Guide, HP 70000 Series Modular, Spectrum Analyzer System, HP 70900B Local Oscillator, Source-Controlled Modules." [Online]. Available: http://userequip.com/files/specs/1394/HP%2070000,%2070900B%20Series%20User.pdf.

[106] M. Liao, "Monolithic III–V quantum-dot light sources on silicon for silicon photonics," UCL (University College London), 2020.

[107] J. Ohtsubo, *Semiconductor lasers: stability, instability and chaos*. Springer, 2012.

[108] S. Shin, U. Sharma, H. Tu, W. Jung, and S. A. Boppart, "Characterization and analysis of relative intensity noise in broadband optical sources for optical coherence tomography," *Ieee Photonic Tech L,* vol. 22, no. 14, pp. 1057-1059, 2010.

[109] H. Zhang *et al.*, "800 Gbit/s transmission over 1 km single-mode fiber using a four-channel silicon photonic transmitter," *Photonics Research,* vol. 8, no. 11, pp. 1776-1782, 2020.

[110] D. Knipp and A. P. B. T. Chakma, "Optical Signal to Noise Ratio (OSNR)," *International University Bremen. Course: Photonics and Optical Communication,* 2005.

[111] D. Behera, S. Varshney, S. Srivastava, and S. Tiwari, "Eye Diagram Basics: Reading and applying eye diagrams," *EDN Network,* 2011.

[112] N. S. Bergano, F. Kerfoot, and C. Davidsion, "Margin measurements in optical amplifier system," *Ieee Photonic Tech L,* vol. 5, no. 3, pp. 304-306, 1993.

[113]   W. Freude *et al.*, "Quality metrics for optical signals: Eye diagram, Q-factor, OSNR, EVM and BER," in *2012 14th International Conference on Transparent Optical Networks (ICTON)*, 2012: IEEE, pp. 1-4.

Chapter 3 InAs Quantum-Dot Mode-Locked Optical Frequency Combs

3.1 Introduction

As already discussed in Chapter 1, the QD material has long been thought advantageous in realising MLLs over their counterparts in terms of spectral bandwidth, pulse duration, noise performance, and peak power [1]. Passively QD MLLs, with the simplest structures, have been intensively studied for over 20 years and demonstrate superior mode-locking performance [2]. Since the pulse generation in a passively QD MLL is dominated by mutual interference between the gain and the SA regions, a number of research have been conducted around the world to investigate the effects of cavity geometry on pulse quality [3-6]. Various studies have shown that, for a two-section QD MLL, the pulse duration and the mode-locking area are correlated with the SA-to-gain length ratio. However, most previous research used a fixed cavity length when exploring the influence of SA-to-gain length ratios, which means that a change in SA section length will always be accompanied by a change in gain section length [4]. In more details, a longer SA section will inevitably shorten the length of gain section for a fixed laser cavity length, thereby resulting an overall increased amount of pulse shortening per cavity round-trip. In our case, the length of the SA section was intended to be fixed so that all absorbers could have similar carrier dynamics at the same reverse bias, which allows me to better compare the role played by the SA section in different SA-to-gain ratios.

This chapter systematically characteristic the performance of OFC generated by InAs/GaAs QD-based passive mode-locked lasers at room-temperature. In section 3.2, the design of the epitaxial structure for device fabrication will be presented first, followed by the description of proposed device geometry including both the ridged waveguide and the tapered structures. Subsequently, the impact of different cavity geometries on mode-locking performance is investigated in section 3.3.

Meanwhile, the key features such as the optical spectrum, electrical spectrum, noise figure, and time-domain characteristics are presented through the experimental study of a 25.5 GHz MLL. Finally, the conclusion is drawn in section 3.4.

3.2 Material and Device Design

The general epitaxial structure employed in this work has been aforementioned in section 2.1, where the InAs QD laser structure was grown on a Si-doped GaAs (001) substrate using MBE. The epitaxy starts with a 300 nm-thick n-type GaAs buffer layer followed by a combination of n-type $Al_{0.2}Ga_{0.8}As/Al_{0.4}Ga_{0.6}As/Al_{0.2}Ga_{0.8}As$ lower cladding layers with thickness of 20 nm/1400 nm/20 nm, respectively. Above the lower cladding layer is the active region, followed by another combination of $Al_{0.2}Ga_{0.8}As/Al_{0.4}Ga_{0.6}As/Al_{0.2}Ga_{0.8}As$ p-type upper cladding layers with thickness of 20 nm/1400 nm/20 nm, respectively, and finally, a 400 nm heavily doped p-type GaAs contact layer is capped [7]. According to our potential application scenarios of high-temperature operation (discussed in Chapter 4), the active region has been specially designed to obtain a desired high optical gain with emission wavelengths in the 1.3 μm range. The cross-sectional transmission electron microscopy (TEM) image of the active region is shown in Fig. 3.1 (a), where a total ten-layer stack of InAs QDs was used (twice as many layers as were previously used in [8]). Rather than utilising the DWELL structure, the InAs layer was directly deposited on the GaAs surface and the InAs islands occurred through S-K growth mode [9]. In an optimised growth condition, dot density as high as 5.9×10^{10} cm^{-2} could be achieved for each layer, which nearly doubles the previous dot density of 3×10^{10} cm^{-2} [7]. In addition, based on the high-resolution bright-field scanning TEM image of a single dot (shown in the inset of Fig. 3.1 (a)), the average size of an in-plane dot is about 20 nm in diameter and 7 nm in height. A special mention must be made of Dr Wei Li from the Beijing University of Technology, who provided all TEM characterisation in this thesis. The comparison of the room temperature photoluminescence (PL) spectra for the full QD laser epi wafer grown under previous conditions and the optimised growth condition is

presented in Fig. 3.1 (b). As seen, the FWHM value of the PL spectrum curve, affected by the inhomogeneous broadening (caused by the size and shape distribution of the QDs), is about 30 meV in this work. Such a narrow luminescence linewidth is comparable to our previous observation of 29 meV with a low dot density case. Therefore, we can conclude that the uniformity of QDs in our structure is well preserved without sacrificing dot density and multi-layer structures [10]. Simultaneously, the quantised-energy separation (*ΔE*) between the ground-state (GS) and the 1st excited-state (ES1) is improved to 88 meV in this work (68 meV in previous work). The enhanced energy separation is crucial in suppressing carrier overflow as well as preventing higher-order modes lasing at elevated temperatures [9, 11, 12]. This is quite advantageous for fulfilling the high-temperature operation of QD lasers as discussed in Chapter 4. The proposed layouts for two-section QD MLLs are schematically shown in Fig. 3.1 (c): the conventional uniform ridged waveguide structure (left) and the tapered structure (right). To evaluate the effects of different SA-to-gain ratios ($\frac{L_{SA}}{L_{Gain}}$), a set of fabricated devices with a fixed L_{SA} of 200 μm and $\frac{L_{SA}}{L_{Gain}}$ ranging from 1:3 to 1:7 has been studied in each structure. For the ridged waveguide structure, the laser tip has a dimension of a mesa width of 5 μm with various gain section lengths of $L_{Gain} = 600$ μm, 800 μm, 1000 μm, 1200 μm and 1400 μm. For the tapered structure, while the similar straight waveguide section with a fixed $L_{SA} = 200$ μm and a width of 5 μm acts as both a mode filter inhibiting lasing from high order transverse modes and an SA in the tapered structure [1], the tapered gain section has a full angle of 3.5°. Selective shallow wet etching is used to remove the heavily p-doped contact layer between the gain section and the absorber section, resulting in a measured isolation resistance of 8 kΩ. Both facets of all fabricated devices are left as-cleaved. The specific geometrical parameters involved are summarised in Table 3.1.
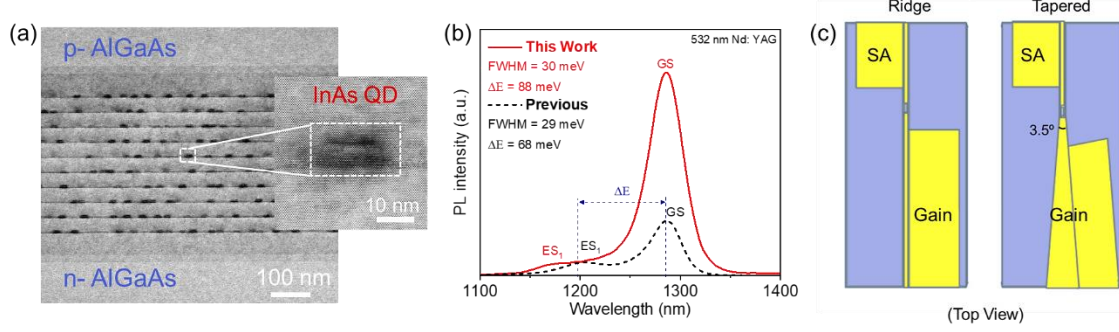
Figure 3.1 (a) TEM image of the InAs/GaAs QD active region. The inset shows the high-resolution bright-field scanning TEM image of a single dot. (b) Comparison of the room temperature PL spectra of samples grown under previous conditions and the optimized growth conditions employed in this work. (c) Schematic drawing of designed two-section MLLs with ridged waveguide structure (left) and tapered structure (right).

Table 3.1 Summary of device parameters for designed QD MLLs structures.

	$L_{SA} : L_{Gain}$				
	1:3	**1:4**	**1:5**	**1:6**	**1:7**
L_{SA} (μm)	200	200	200	200	200
L_{Gain} (μm)	600	800	1000	1200	1400
W_{SA} (μm)	5	5	5	5	5
W_{Gain_ridge} (μm)	5	5	5	5	5
$W_{Gain\_tapered}$ (μm)	41.6	53.8	66	78.2	90.5
A_{ridge} (cm^2)	4.075E-05	5.075E-05	6.075E-05	7.075E-05	8.075E-05
$A_{tapered}$ (cm^2)	1.506E-04	2.460E-04	3.658E-04	5.100E-04	6.793E-04

3.3 Results and Discussion

3.3.1 Light-Current Characteristics

The basic *L-I* characteristics at room-temperature were carried out first to reveal the bistable nature of those devices under investigation. As aforementioned in Chapter 2, the light power emitted from the gain facet is detected and plotted as a

function of injected current in the gain section with different V_{rev} applied to the SA section. As expected, the I_{th} increases while the η drops with increasing V_{rev}, suggesting an enhanced absorption loss in the SA section. For all fabricated samples, the non-linear saturation effect of the SA is observed, evidenced by the sudden power rise (also known as 'kink point') near the threshold current. This phenomenon becomes more pronounced at a higher reversed bias level. However, the performance of those devices varies dramatically in the forward/backward sweep of the injected current: some showed a strong hysteresis like described in [13-17], while others posed little or no hysteresis as reported in [18-20]. Figure 3.2 (a) displays a representative L-I curve of a ridged waveguide MLL with a L_{SA} : L_{Gain} = 1: 3 that exhibits a remarkable counter-clockwise hysteresis loop (red dashed box). The origin of such bistable operation results from the nonlinear saturation of the QD absorption that involved the state filling of the ground state and the electro-absorption arising from the quantum-confined Stark effect under the applied electrical field [21-23]. I have also observed that under higher reversed bias voltage, the hysteresis loop tends to shift to a higher laser current with a wider loop width, which can be ascribed to the large difference between the unsaturated and saturated loss of the absorber [16, 24]. In order to eliminate geometry-induced variations such as different SA-to-gain length ratios, the measured I_{th} for each configuration was converted into J_{th} and then plotted in Fig. 3.2(b). In general, the J_{th} decreases with increasing cavity length, and the divergence between the shortest (1: 3) and the longest devices (1: 7) is amplified by the V_{rev} increment. For example, when $V_{rev} = 0$ V, the values of J_{th} equal to 834 A/cm^{-2} and 260 A/cm-^{2} for 1: 3 and 1: 7 devices, respectively, and those values increase to 3141 A/cm^{-2} (1: 3) and 383 A/cm^{-2} (1: 7) at - 4 V reversed bias. It should be noticed that for a ratio equal to 1: 3, the device is unable to lase for V_{rev} above -4 V due to insufficient device gain. Moreover, for each ratio, the J_{th} increases exponentially with enhanced applied V_{rev} due to the increased absorber recovery time, which also indicates the presence of electro absorption within the devices [16, 25].
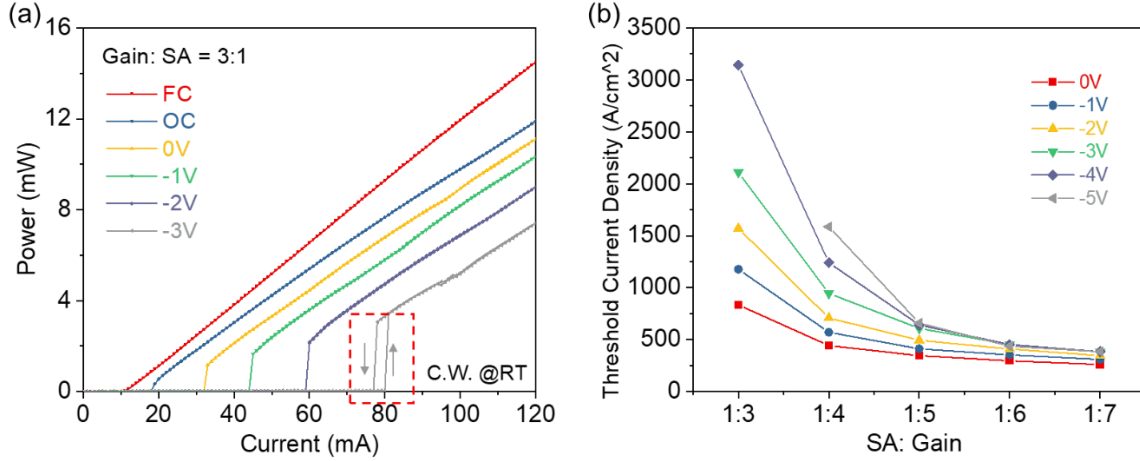
Figure 3.2 Typical RT L-I characteristics of two section QD MLLs with ridged waveguide structure: (a) L-I curves of an 815-μm-long device (L_{SA} : L_{Gain}= 1:3) for different SA reversed biases. (b) Measured J_{th} as a function of different gain-to-SA length ratios under various reverse-bias voltage.

The comparison of *L-I* characteristics between the ridged waveguide structure (dashed line) and the tapered structure (solid line) is exhibited in Fig. 3.3. According to the plot, the tapered structure has larger J_{th} and noteworthy greater slope efficiencies than those of the ridged waveguide structure for all designed ratios. The values of measured J_{th} and calculated slope efficiency for each configuration are tabulated in Table 3.2, where the slope efficiencies in tapered structure are nearly 3 to 6 times higher than those of the ridged waveguide structure. The reason is that in a flared gain section, the larger active volume results in a higher output power [14]. Meanwhile, the optical mode from a narrow region that gives a single lateral optical mode would gradually expand to a wider multimode region for higher pulse saturation energy [26]. Hence, the SA section could be easily saturated, leading to an improvement in mode-locking performance including a reduction in τ_p and an enhancement of peak power [26-29].
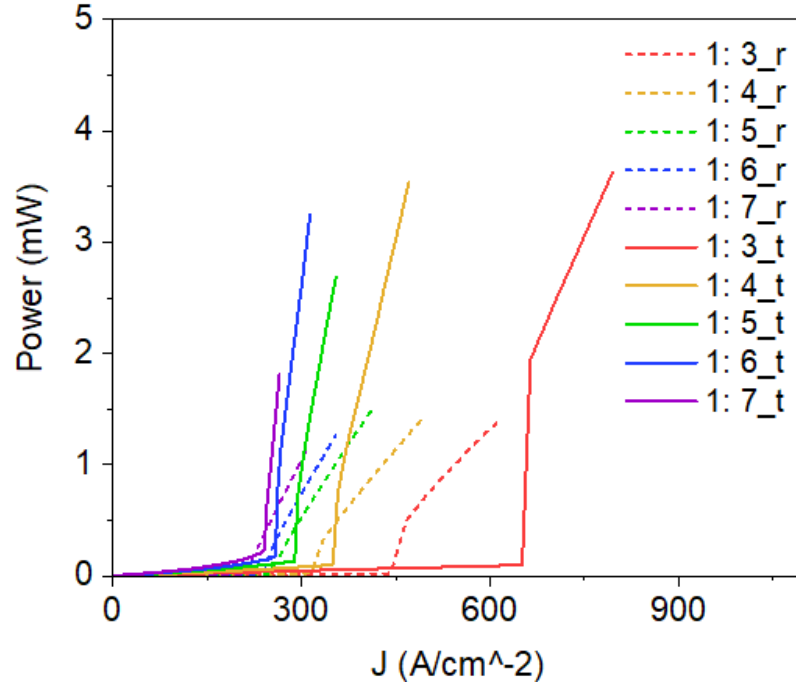
Figure 3.3 L-I characteristics of two section QD MLLs with ridged waveguide structure (dashed line) and tapered structure (solid line).

Table 3.2 Summary of measured J_{th} and calculated slope efficiency for each configuration in Fig. 3.3.

		$L_{SA} : L_{Gain}$				
		1:3	**1:4**	**1:5**	**1:6**	**1:7**
J_{th}	**Ridge**	441	315.235	246.87	241.091	211.142
(A/cm^{-2})	**Tapered**	650.713	349.58	288.97	258.282	241.048
Slope efficiency	**Ridge**	4.363	5.429	7.151	8.2	9.69
(mW/(mA/cm^{-2}))	**Tapered**	11.734	23.169	29.77	46.539	59.204

3.3.2 Mode-locking Performance

As already mentioned in Section 2.3, the mode-locking performance in our work is characterised by examining the optical spectra, RF spectra, autocorrelation traces and the noise figure. Here, a two-section ridged waveguide QD MLL with an SA-to-gain ratio equal to 1: 7 is used as a classical example for further illustration. In

our work, successful mode-locking is determined when its SNR of fundamental frequency tone is larger than 25 dB (RBW: 1 MHz, VBW: 10 kHz) and corresponding τ_p is narrower than 15 ps.

The mode-locking characteristics of this 25.5 GHz QD MLL at room-temperature are presented in Fig. 3.4. All measurements are taken under the conditions of $I_{gain} = 75.22\,\text{mA}$ and $V_{rev} = -2.9\,\text{V}$, where the shortest τ_p is obtained at this injected current level. Figure 3.4 (a) presents the measured optical spectrum whose centre lasing wavelength (~ 1294 nm) is ideally located at low-loss for telecom O-band. The 3 dB bandwidth of this coherent comb spectrum is 3.962 nm (4.956 nm for 6 dB), providing a maximum of potential 30 channels (37 lines within 6 dB) with an OSNR well above 25 nm (0.1 nm ASE noise bandwidth). While it is difficult to estimate the actual transition capacity of this laser source until a system-level WDM experiment employing an advanced modulation format with direct detection is performed, as a guideline, each comb line could be employed as an optical carrier for realising the high-speed optical transmission [30, 31]. Besides, the symmetric optical profile also suggests that a near-zero LEF of semiconductor QD lasers has been achieved [32, 33]. Fig. 3.4 (b) shows the autocorrelation trace captured by an oscilloscope, corresponding to the narrowest pulse of 4.906 ps at an $I_{gain} = 75.22\,\text{mA}$ and under assumption of a Gaussian pulse profile. The RF trace under this condition is depicted in Fig. 3.4 (c). The signal has a sharp fundamental RF tone at ~ 25.5 GHz with an SNR of 47.9 dB, and no low-frequency fluctuations are observed. Due to the technical limitation, the higher-order harmonics cannot be observed on the RF spectrum. The inset of Fig. 3.4 (c) gives a zoom-out view of the fundamental RF tone in a narrow span. The RF peak (f_{rep}) located at 25.504 GHz is in good agreement with the free spectral range (FSR) of this device. A narrow 3 dB linewidth of 32 kHz could be obtained when the trace is deconvolved using Lorentz fit. The corresponding single-sideband (SSB) phase noise is illustrated in Fig. 3.4 (d). The integrated timing jitter is 2.45 ps in the range of 100 kHz to 1 GHz, and 326 fs from 4 to 80 MHz of the ITU-T specific range. It should be mentioned that the driving condition used here was not optimised for the

narrowest RF linewidth, namely the lowest noise performance. The noise performance studies of QD-based MLLs have demonstrated exceptional narrow RF linewidths [34-37] as well as record values for mode-locking timing-jitter [30, 38-40], owing to the reduced ASE and lower confinement factor properties of QDs compared with its higher-dimensional comparts [1, 2].
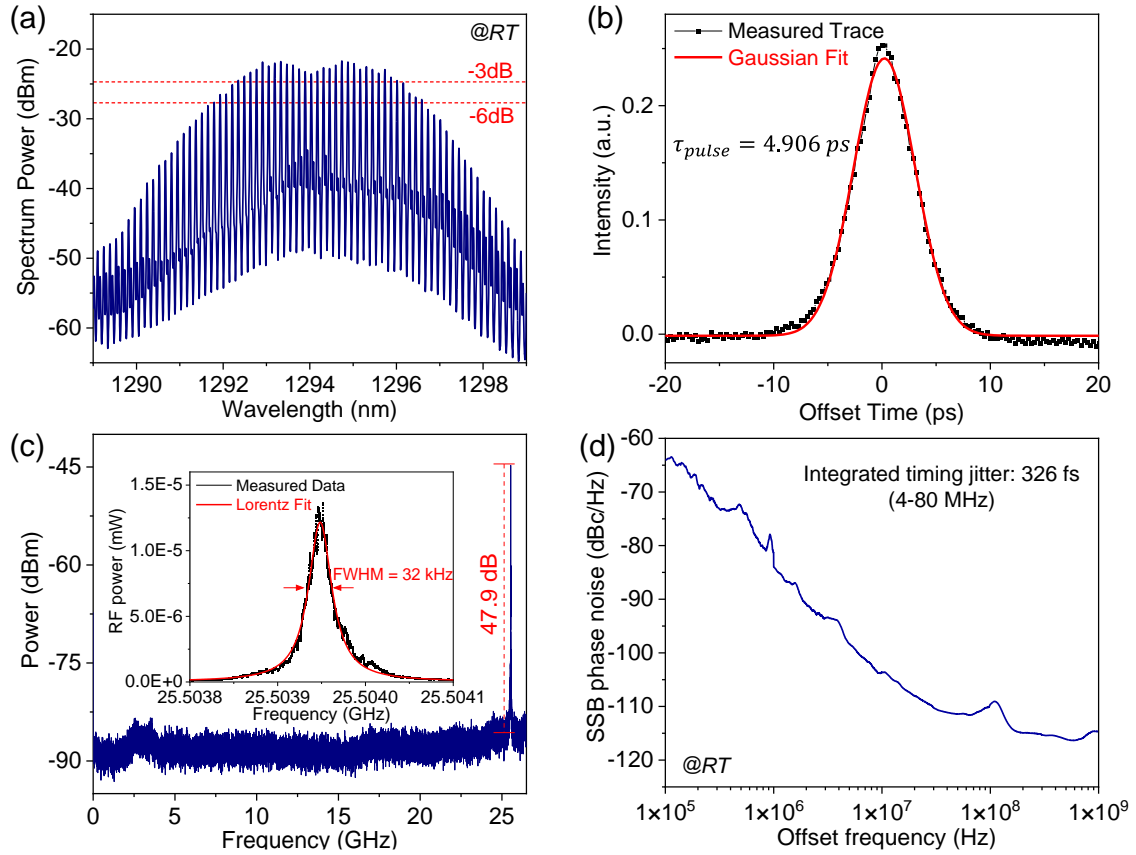
Figure 3.4 25.5 GHz two-section passively QD-MLL performance characterisation at room temperature under bias conditions of I_{gain} = 75.22 mA and V_{rev} = - 2.9 V: (a) Optical spectrum. (b) Autocorrelation trace with Gaussian pulse fitting. (c) RF spectrum in a 26.5 GHz span view (RBW: 1 MHz, VBW: 10 kHz). The inset shows the narrow span RF peak with Lorentz fit (RBW: 1 kHz, VBW: 100 Hz). (d) Corresponding single-sideband phase noise plot.

3.3.3 Effect of Driving Conditions

In a two-section passively MLL, the mode-locking characteristics are highly related to the mutual interference between the SA and the gain sections. For this reason, changes in the I_{gain} and the V_{rev} will lead to a considerable influence on mode-locking performance [1]. The devices in all designed ratios were examined to find

out the specific impact of those two variables, and the plotted results are attached as Appendix B. Even though the test results for each ratio show similar tendencies, I will discuss only the SA-to-gain ratio of 1: 4 as an example in this section, of which trend is highlighted in Fig. 3.5. For trends in V_{rev}, the I_{gain} was fixed at 110 mA, and for trends in I_{gain}, the V_{rev} was fixed at -2.5 V. The test range was found to yield stable mode-locking, beyond which the mode-locking smoothly disappears into a continuous wave emission or no-lasing regime. In general, the shortest τ_p tends to occur at high V_{rev} and low I_{gain}, and this is consistent with the observations reported by most research groups [5, 14, 17, 41]. When driving conditions deviate from such optimum points, the undesired pulse broadening as well as pulse chirping appears. At a fixed I_{gain} level, the increased V_{rev} leads to an exponential decrease of the SA recovery time, which results in a reduced time window over which the pulse experiences net gain, and this is the origin of the pulse-shortening mechanism [29, 42, 43]. Consequently, the τ_p decreases in an exponential-like manner with increasing V_{rev} due to the enhanced pulse-shortening mechanism (Fig. 3.5 (a)). The calculated TBP of our devices follows a similar trend as the τ_p, and it has been suggested that the lowest TBP values are often achieved for the shortest τ_p [41, 44]. Under certain injected current level, the TBP values vary from ~1 to ~4, which are far greater than the Fourier-transform-limited value (0.441 for Gaussian pulses), indicating that some residual frequency chirp being present in the pulses and the laser performance in the term of τ_p and P_{peak} could be further improved [18]. Unlike the phenomenon reported in ref [1], the optical spectral bandwidth in our case was strongly dependent on the driving conditions (Fig. 3.5 (b)), and even exhibited a periodic spectral bandwidth broadening in a smaller SA-to-gain length ratio (Appendix B, SA: Gain = 1: 7 and 1: 6). Besides, a significant blue-shift of the lasing wavelength was observed for increased V_{rev}. Those abnormal behaviours have also been witnessed by the group from Glasgow, and they believed that this is an indication of the onset of some kind of dynamics where the emission wavelength is close to the modal gain peak instead of the SA band-edge [45, 46]. In our case, such a spectral enlargement with a blue-shifted

emission wavelength was attributed to the dominant band-filling effect caused by large carrier densities attainable in this ten-QD layer stack [47-49].

For measurements carried out with a constant V_{rev}, the τ_p and TBP show an entirely different trend for changes in I_{gain}. As can be seen from Fig. 3.5 (c), the shortest τ_p (~ 3.88 ps) occurs at the lower-limit of the selected test range ($I_{gain} = 50\,\text{mA}$), associated with a nearly Fourier-transform-limited TBP (0.443). An increase in I_{gain} leads to a steady broadening in τ_p along with a higher TBP, which is in good agreement with previously published results [1, 14, 50, 51]. This is because the optical loss modulation in SA becomes less effective and disturbs efficient pulse-shaping mechanism. Consequently, a larger V_{rev} is often required to maintain stable mode-locking operation at a higher I_{gain} level [48]. Aside from pulse broadening, spectral broadening and red-shift in centre wavelength are also evidenced in Fig. 3.5 (d). From $I_{gain} = 50$ mA to $I_{gain} = 150$ mA, the device has experienced ~ 12 nm red-shift due mostly to band-gap shrinkage effect caused by the unavoidable Joule heating in the active region [18, 45].
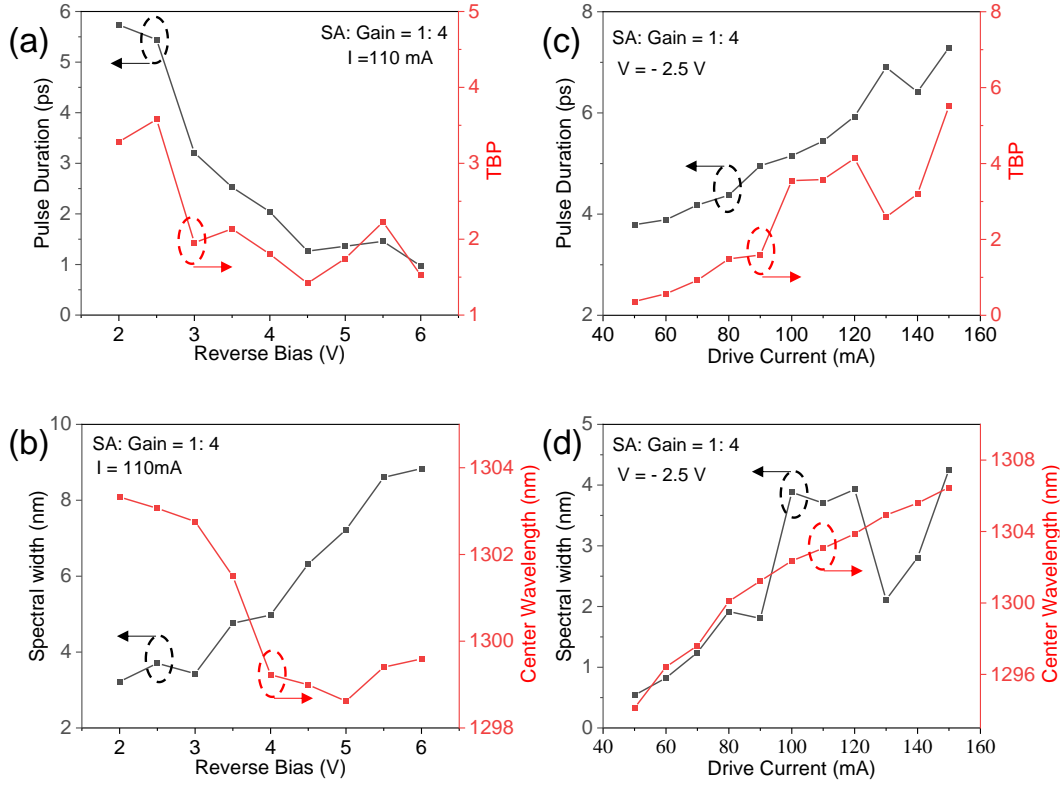
Figure 3.5 Pulse duration, TBP, spectral width, and centre wavelength with drive current and reverse bias for a 40.5 GHz two-section passively QD-MLL with SA: Gain = 1: 4.

Figure 3.6 compares the τ_p obtained from different QD MLL configurations, and an interesting finding is that, under the same driving conditions, a longer gain section could produce a relative broader pulse. The pulse stretch could be explained by considering the interplay between pulse shortening in the SA section and pulse broadening in the gain section [29]. For a fixed SA length, the device associated with a longer gain section length introduces additional saturable gain into the laser cavity, which results in an increased pulse broadening experienced by the pulse in each cavity round-trip. As a result, an overall increment in the minimum achievable τ_p has been witnessed in configurations with lower SA-to-gain length ratios [1, 24].
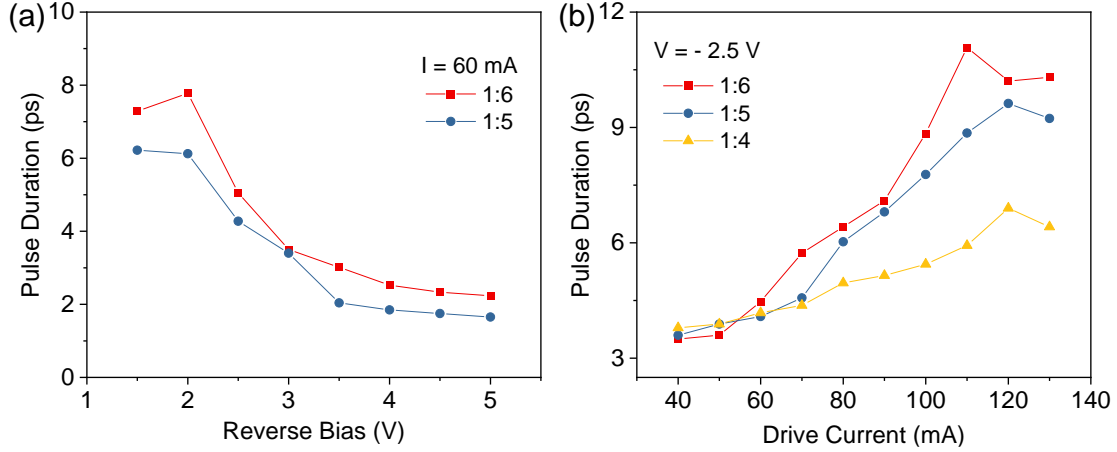
Figure 3.6 Pulse duration versus (a) reverse bias, and (b) drive current for QD MLLs with different SA-to-gain length configurations.

3.3.4 Regimes of Mode-locking

To avoid the complexity of τ_p mapping in our setup, the mode-locking regimes are denoted by the peak SNR of output RF signals [24]. Figure 3.7 shows the 2D mapping diagrams of the fundamental RF peak SNR values for the QD MLLs with different SA-to-gain length ratios. Here, colour scale is used to help us visualise the mode-locking quality of each laser device under various driving conditions. It is believed that stable mode-locking can only occur when the RF peak SNR is greater than or equal to 25 dB, therefore, all points with RF peak SNR less than 25 dB are rejected and shown in white. In general, except for the shortest devices, stable mode-locking occurs over a range of V_{rev} from -1 to -5 V and driving currents from I_{th} to beyond nearly five times the threshold. For a fixed V_{rev}, the best mode-locking performance generally occurs at the onset of lasing and then deteriorates as the I_{gain} increases.Similar investigations have been done by the research group from the University of Cambridge, who announced that for a fixed laser cavity length, the stable mode-locking occurs in a greater range for device with larger SA-to-gain length ratios [1]. However, this conclusion does not hold in our case since the total cavity lengths vary with the SA-to-gain length ratios. Therefore, a direct comparison of the mode-locking regime between different configurations is not convincing. Despite that, all mapping results suggest that the combination of

a lower I_{gain} and a higher V_{rev} is more preferred for stable mode-locking operation where a shorter τ_p usually occurrs. The reason behinds this phenomenon has been widely discussed in ref [1, 5, 30], mainly ascribed to the effective pulse-shaping dynamics within the QD materials. In comparison to the mapping results on the device with longer gain section (e.g., SA: Gain = 1: 7), a much smaller mode-locking region in shorter device can be observed. Taking the QD MLL with SA: Gain = 1: 3 as an example (Fig. 3.7 (a)), the device does not turn on at all when V_{rev} falls below –3.5 V, whereas other longer configurations could operate beyond -5V. This is because the short gain section cannot provide sufficient gain to compensate for the mirror and internal loss [5]. Furthermore, the heatmap suggests that the broadest mode-locking region with good quality locates in SA-to-gain length ratio equal to 1: 5 or 1: 6, indicating that there is a trade-off between the SA, gain and total cavity length [4]. Thus, careful optimisation of the SA and gain lengths is always necessary for achieving ideal mode-locking performance.
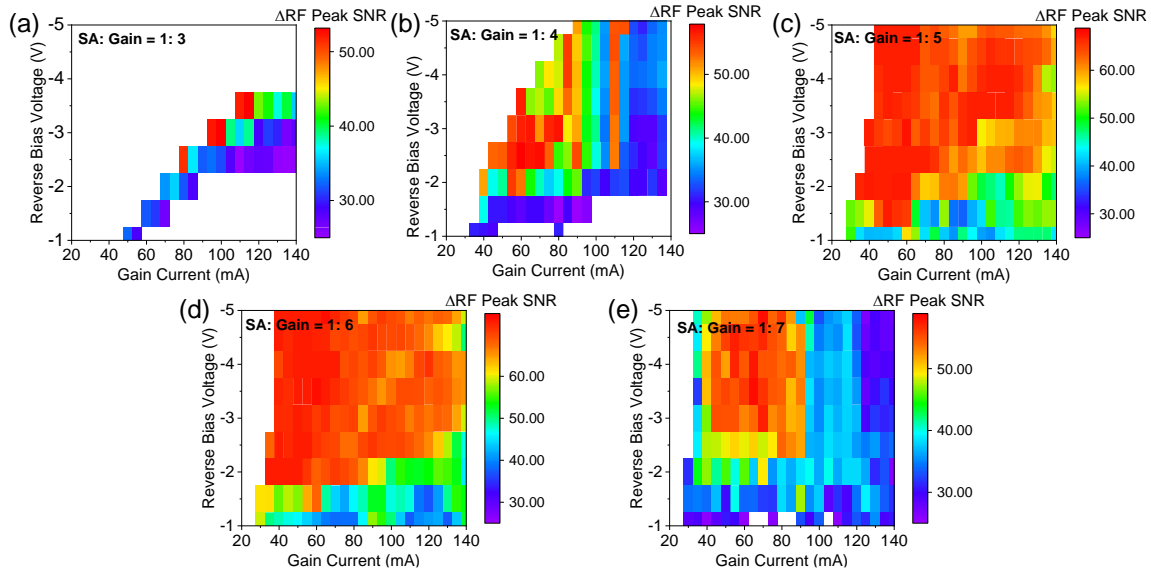
Figure 3.7 Fundamental RF peak SNR mapping as a function of I_{gain} and V_{rev} for QD MLLs with various SA-to-gain length configurations.

3.4 Conclusion

This chapter details the design of InAs/GaAs QD MLLs for both ridged waveguide structure and tapered waveguide structure. A comparison between the L-I curves

for both structures suggests that QD MLL with a tapered structure is more desired for high-power applications, and this is consistent with the statement in ref [14, 26]. Based on the findings by Alastair R. Rae *et al.*, the value of $\frac{L_{SA}}{L_{gain}}$ in my work is modified to locate within the range from 1:3 to 1:14 to avoid either an insufficient gain or an insufficient saturable absorption that led to mode-locking not occurring [4]. Unlike ref [3-6], I intentionally fixed the length of the SA section rather than the laser cavity length to experiment with various SA-to-gain length ratios. Even though my subsequent experiments revealed that my design was flawed as it is impossible to make direct comparisons between different cavity lengths, I still reached some similar conclusions to others.

Overall, a systematic investigation of the basic characteristics of laser devices with two-section ridged waveguide cavity geometries is presented. The effect of the SA-to-gain length ratios on the τ_p and mode-locking regimes over a wide range of driving conditions and cavity configurations have been discussed. Our findings prove that by carefully designing the laser cavity geometry, it is able to generate high-quality and Fourier-transform limited pulses from a QD laser diode with extremely simple geometry. This work shows that the QD MLL is feasible as a compact and efficient comb source in a range of potential applications.

3.5 Reference

[1]   M. G. Thompson, A. R. Rae, M. Xia, R. V. Penty, and I. H. White, "InGaAs quantum-dot mode-locked laser diodes," *IEEE Journal of Selected Topics in Quantum Electronics,* vol. 15, no. 3, pp. 661-672, 2009.

[2]   E. U. Rafailov, M. A. Cataluna, and W. Sibbett, "Mode-locked quantum-dot lasers," *Nature photonics,* vol. 1, no. 7, pp. 395-401, 2007.

[3]   S. T. Liu, J. C. Norman, D. Jung, M. J. Kennedy, A. C. Gossard, and J. E. Bowers, "9 GHz passively mode locked quantum dot lasers directly grown on Si," (in English), *Ieee Device Res Conf,* 2018. [Online]. Available: <Go to ISI>://WOS:000444728400026.

[4]   A. Rae, M. Thompson, A. Kovsh, R. Penty, and I. White, "InGaAs–GaAs quantum-dot mode-locked laser diodes: optimization of the laser geometry for subpicosecond pulse generation," *Ieee Photonic Tech L,* vol. 21, no. 5, pp. 307-309, 2009.

[5]   M. Kuntz *et al.*, "Direct modulation and mode locking of 1.3 μm quantum dot lasers," *New Journal of Physics,* vol. 6, no. 1, p. 181, 2004.

[6]   J. K. Mee, M. T. Crowley, R. Raghunathan, D. Murrell, and L. F. Lester, "Characteristics of Passively Mode-Locked Quantum Dot Lasers from 20 to 120 degrees C," (in English), *Physics and Simulation of Optoelectronic Devices Xxi,* vol. 8619, 2013, doi: 10.1117/12.2004567.

[7]   S. Pan *et al.*, "Quantum dot mode-locked frequency comb with ultra-stable 25.5 GHz spacing between 20° C and 120° C," *Photonics Research,* vol. 8, no. 12, pp. 1937-1942, 2020.

[8]   S. Chen *et al.*, "Electrically pumped continuous-wave III–V quantum dot lasers on silicon," *Nature Photonics,* vol. 10, no. 5, pp. 307-311, 2016.

[9]   K. Nishi, K. Takemasa, M. Sugawara, and Y. Arakawa, "Development of quantum dot lasers for data-com and silicon photonics applications," *IEEE Journal of Selected Topics in Quantum Electronics,* vol. 23, no. 6, pp. 1-7, 2017.

[10]   K. Nishi *et al.*, "Molecular beam epitaxial growths of high-optical-gain InAs quantum dots on GaAs for long-wavelength emission," *Journal of crystal growth,* vol. 378, pp. 459-462, 2013.

[11]   T. Kageyama *et al.*, "Extremely high temperature (220 C) continuous-wave operation of 1300-nm-range quantum-dot lasers," in *The European Conference on Lasers and Electro-Optics*, 2011: Optical Society of America, p. PDA_1.

[12]   T. Kageyama *et al.*, "Long-wavelength quantum dot FP and DFB lasers for high temperature applications," in *Novel In-Plane Semiconductor Lasers XI*, 2012, vol. 8277: SPIE, pp. 73-80.

[13]   X. Huang, A. Stintz, H. Li, L. Lester, J. Cheng, and K. Malloy, "Passive mode-locking in 1.3 μm two-section InAs quantum dot lasers," *Appl Phys Lett,* vol. 78, no. 19, pp. 2825-2827, 2001.

[14]   M. Thompson *et al.*, "Subpicosecond high-power mode locking using flared waveguide monolithic quantum-dot lasers," *Appl Phys Lett,* vol. 88, no. 13, p. 133119, 2006.

[15]   M. Thompson *et al.*, "Transform-limited optical pulses from 18 GHz monolithic modelocked quantum dot lasers operating at/spl sim/1.3/spl mu/m," *Electron Lett,* vol. 40, no. 5, pp. 346-347, 2004.

[16]   X. Huang *et al.*, "Bistable operation of a two-section 1.3/spl mu/m InAs quantum dot laser-absorption saturation and the quantum confined Stark effect," *Ieee J Quantum Elect,* vol. 37, no. 3, pp. 414-417, 2001.

[17]   L. Zhang *et al.*, "Low timing jitter, 5 GHz optical pulses from monolithic two-section passively mode-locked 1250/1310 nm Quantum Dot lasers for high speed optical interconnects," in *Optical Fiber Communication Conference*, 2005: Optical Society of America, p. OWM4.

[18]   E. U. Rafailov *et al.*, "High-power picosecond and femtosecond pulse generation from a two-section mode-locked quantum-dot laser," *Appl Phys Lett,* vol. 87, no. 8, p. 081107, 2005.

[19]   S. Pan *et al.*, "Ultra-stable 25.5 GHz quantum dot mode-locked frequency comb operating up to 120° C," in *CLEO: Science and Innovations*, 2021: Optical Society of America, p. SF2F. 3.

[20]   A. Gubenko *et al.*, "High-power monolithic passively modelocked quantum-dot laser," *Electron Lett,* vol. 41, no. 20, pp. 1124-1125, 2005.

[21]   S. Ping and L. Chao, "Bistability threshold inside hysteresis loop of nonlinear fiber Bragg gratings," *Optics Express,* vol. 13, no. 13, pp. 5127-5135, 2005.

[22] T. Matsumoto, M. Ohtsu, K. Matsuda, T. Saiki, H. Saito, and K. Nishi, "Low-temperature near-field nonlinear absorption spectroscopy of InGaAs single quantum dots," *Appl Phys Lett,* vol. 75, no. 21, pp. 3246-3248, 1999.

[23] S. Schmitt-Rink, D. Miller, and D. S. Chemla, "Theory of the linear and nonlinear optical properties of semiconductor microcrystallites," *Physical Review B,* vol. 35, no. 15, p. 8113, 1987.

[24] S. T. Liu, J. C. Norman, D. Jung, M. J. Kennedy, A. C. Gossard, and J. E. Bowers, "Monolithic 9 GHz passively mode locked quantum dot lasers directly grown on on-axis (001) Si," (in English), *Appl Phys Lett,* vol. 113, no. 4, Jul 23 2018, doi: 10.1063/1.5043200.

[25] J. K. Mee, R. Raghunathan, J. B. Wright, and L. F. Lester, "Device geometry considerations for ridge waveguide quantum dot mode-locked lasers," (in English), *J Phys D Appl Phys,* vol. 47, no. 23, Jun 11 2014, doi: 10.1088/0022-3727/47/23/233001.

[26] A. Mar, R. Helkey, W. Zou, D. B. Young, and J. E. Bowers, "High‑power mode‑locked semiconductor lasers using flared waveguides," *Appl Phys Lett,* vol. 66, no. 26, pp. 3558-3560, 1995.

[27] M. Rossetti, T. H. Xu, P. Bardella, and I. Montrosset, "Impact of Gain Saturation on Passive Mode Locking Regimes in Quantum Dot Lasers With Straight and Tapered Waveguides," (in English), *Ieee J Quantum Elect,* vol. 47, no. 11, pp. 1404-1413, Nov 2011, doi: 10.1109/Jqe.2011.2167131.

[28] D. I. Nikitichev *et al.*, "High peak power and sub-picosecond Fourier-limited pulse generation from passively mode-locked monolithic two-section gain-guided tapered InGaAs quantum-dot lasers," *Laser Physics,* vol. 22, no. 4, pp. 715-724, 2012.

[29] K. Williams, M. Thompson, and I. White, "Long-wavelength monolithic mode-locked diode lasers," *New Journal of Physics,* vol. 6, no. 1, p. 179, 2004.

[30] S. T. Liu *et al.*, "High-channel-count 20 GHz passively mode-locked quantum dot laser directly grown on Si with 4.1 Tbit/s transmission capacity," (in English), *Optica,* vol. 6, no. 2, pp. 128-134, Feb 20 2019, doi: 10.1364/Optica.6.000128.

[31] G. Liu *et al.*, "Passively mode-locked quantum dash laser with an aggregate 5.376 Tbit/s PAM-4 transmission capacity," *Optics express,* vol. 28, no. 4, pp. 4587-4593, 2020.

[32]   A. Sobiesierski and P. M. Smowton, "6.09 - Quantum-Dot Lasers: Physics and Applications," in *Comprehensive Semiconductor Science and Technology*, P. Bhattacharya, R. Fornari, and H. Kamimura Eds. Amsterdam: Elsevier, 2011, pp. 353-384.

[33]   S. Barbieri and S. Kumar, "13 - Terahertz (THz) quantum cascade lasers," in *Semiconductor Lasers*, A. Baranov and E. Tournié Eds.: Woodhead Publishing, 2013, pp. 514-550.

[34]   F. Kefelian, S. O'Donoghue, M. T. Todaro, J. G. McInerney, and G. Huyet, "RF linewidth in monolithic passively mode-locked semiconductor laser," (in English), *Ieee Photonic Tech L,* vol. 20, no. 13-16, pp. 1405-1407, Jul-Aug 2008, doi: 10.1109/Lpt.2008.926834.

[35]   D. Auth, S. T. Liu, J. Norman, J. E. Bowers, and S. Breuer, "Passively mode-locked semiconductor quantum dot on silicon laser with 400 Hz RF line width," (in English), *Optics Express,* vol. 27, no. 19, pp. 27256-27266, Sep 16 2019, doi: 10.1364/Oe.27.027256.

[36]   C.-Y. Lin, F. Grillot, N. Naderi, Y. Li, and L. Lester, "RF linewidth reduction in a quantum dot passively mode-locked laser subject to external optical feedback," *Appl Phys Lett,* vol. 96, no. 5, p. 051118, 2010.

[37]   Y. Ding, M. A. Cataluna, D. Nikitichev, I. Krestnikov, D. Livshits, and E. Rafailov, "Broad repetition-rate tunable quantum-dot external-cavity passively mode-locked laser with extremely narrow radio frequency linewidth," *Applied Physics Express,* vol. 4, no. 6, p. 062703, 2011.

[38]   G. Carpintero, M. G. Thompson, R. V. Penty, and I. H. White, "Low noise performance of passively mode-locked 10-GHz quantum-dot laser diode," *Ieee Photonic Tech L,* vol. 21, no. 6, pp. 389-391, 2009.

[39]   M. Thompson *et al.*, "Absorber length optimisation for sub-picosecond pulse generation and ultra-low jitter performance in passively mode-locked 1.3 μm quantum-dot laser diodes," in *Optical Fiber Communication Conference*, 2006: Optical Society of America, p. OThG3.

[40]   M. T. Todaro *et al.*, "Simultaneous achievement of narrow pulse width and low pulse-to-pulse timing jitter in 1.3 μm passively mode-locked quantum-dot lasers," *Opt Lett,* vol. 31, no. 21, pp. 3107-3109, 2006.

[41]   Y.-C. Xin, Y. Li, V. Kovanis, A. Gray, L. Zhang, and L. Lester, "Reconfigurable quantum dot monolithic multi-section passive mode-locked lasers," *Optics Express,* vol. 15, no. 12, pp. 7623-7633, 2007.

[42]   D. Malins, A. Gomez-Iglesias, S. White, W. Sibbett, A. Miller, and E. Rafailov, "Ultrafast electroabsorption dynamics in an InAs quantum dot saturable absorber at 1.3 μm," *Appl Phys Lett,* vol. 89, no. 17, p. 171111, 2006.

[43]   J. Karin *et al.*, "Ultrafast dynamics in field‑enhanced saturable absorbers," *Appl Phys Lett,* vol. 64, no. 6, pp. 676-678, 1994.

[44]   M. Kuntz, G. Fiol, M. Laemmlin, C. Meuer, and D. Bimberg, "High-speed mode-locked quantum-dot lasers and optical amplifiers," *Proceedings of the IEEE,* vol. 95, no. 9, pp. 1767-1778, 2007.

[45]   P. Stolarz *et al.*, "Spectral dynamical behavior in passively mode-locked semiconductor lasers," *Ieee Photonics J,* vol. 3, no. 6, pp. 1067-1082, 2011.

[46]   T. Hoshida, H. Liu, M. Tsuchiya, Y. Ogawa, and T. Kamiya, "Locking characteristics of a subharmonically hybrid mode-locked multisection semiconductor laser," *Ieee Photonic Tech L,* vol. 8, no. 12, pp. 1600-1602, 1996.

[47]   R. Rosales *et al.*, "InAs/InP quantum-dot passively mode-locked lasers for 1.55-μm applications," *IEEE Journal of Selected Topics in Quantum Electronics,* vol. 17, no. 5, pp. 1292-1301, 2011.

[48]   D. Kunimatsu, S. Arahira, Y. Kato, and Y. Ogawa, "Passively mode-locked laser diodes with bandgap-wavelength detuned saturable absorbers," *Ieee Photonic Tech L,* vol. 11, no. 11, pp. 1363-1365, 1999.

[49]   A. Ukhanov, A. Stintz, P. Eliseev, and K. Malloy, "Comparison of the carrier induced refractive index, gain, and linewidth enhancement factor in quantum dot and quantum well lasers," *Appl Phys Lett,* vol. 84, no. 7, pp. 1058-1060, 2004.

[50]   M. Kuntz *et al.*, "35 GHz mode-locking of 1.3 μm quantum dot lasers," *Appl Phys Lett,* vol. 85, no. 5, pp. 843-845, 2004.

[51]   J. Tourrenc *et al.*, "Cross-correlation timing jitter measurement of high power passively mode-locked two-section quantum-dot lasers," *Ieee Photonic Tech L,* vol. 18, no. 21, pp. 2317-2319, 2006.

Chapter 4 Quantum dot mode-locked frequency comb with ultra-stable 25.5 GHz spacing between 20°C and 120°C

4.1 Introduction

In the previous chapter, I examined the fundamental characteristics of our designed two-section InAs/GaAs QD MLLs at room temperature. The broad 3-dB optical bandwidth, large OSNR values, and multiple available tone spacing of tested devices suggest that our QD MLLs based comb sources could be used in various fields. Among all applications, our research group is particularly interested in employing the QD MLL based OFCs as light sources in optical communication systems, especially for those short and medium reach dense wavelength-division multiplexing (DWDM) communication systems, where the size, cost, and power consumption advantages of the integrated comb sources could be fully applied [1, 2].

In reality, the data communication requires a minimum tone spacing of 25 GHz to support high-speed transmission and the device should be enabled to operate stably in a temperature-varying environment (e.g., -20°C to 85 °C) [3, 4]. Although QD materials, thanks to their unique delta-function-like density of states, have successfully demonstrated intrinsic temperature resistance property [5, 6], the operation in QD MLL involves both thermal mechanisms and the mutual interdependence of the gain section and the SA section. For this reason, realising an ultra-stable QD MLL that works exclusively from the QD GS transition over a wide range of temperatures remains a challenge. Cataluna *et al.* pioneered the stability of mode-locking in 20 GHz InGaAs QD MLLs at elevated temperatures. Unfortunately, in their device, the RF SNR value drops when the operating temperature exceeds 70°C (15 dB at 80°C), which means that the mode-locking operation becomes unstable [7]. Later, the research group from the University of

New Mexico reported their achievement in stable mode-locking working from 20°C to 92°C through GS transition [8]. However, the mode-locking switching between the GS and the ES1 has been observed due to the carrier escape from the GS at increased temperature. Besides, the 8 mm-long cavities employed in their work limit the fundamental f_{rep} to 5 GHz that is not suitable for DWDM systems. Even though one may expect a wide mode-locking temperature from one QD MLL [8, 9] and obtain a high f_{rep} from another [10], the main difficulty is to simultaneously achieve stable mode spacing across a wide range of temperatures from a single two-section QD MLL with high fundamental f_{rep}. To build a more comprehensive understanding of our fabricated devices, in this chapter, the temperature-dependent performances of the QD MLLs used in Chapter 3 are evaluated. Meanwhile, the behaviours of the SA: Gain = 1: 7 devices with a mode spacing equal to 25.5 GHz are studied in more detail since a longer cavity length can theoretically obtain a better thermal stability [11].

4.2 Temperature-Dependent Results and Discussion

4.2.1 Light-Current Characteristics

Figure 4.1 (a) presents the effect of operating temperature on the *L-I* characteristics for a 25.5 GHz two-section ridged waveguide QD MLL when the V_{rev} is fixed at 0 V. It is obvious that the CW lasing was maintained until the test system reached the upper limit of the temperature controller (120°C). No thermal rollover phenomenon has been observed during the whole measurement. From 20°C to 120°C, the I_{th} of the device at V_{rev} = 0 V increased from 20 mA to 128 mA due to the enhanced intrinsic losses caused by carrier escape at elevated temperatures [12], which also led to the degradation of the η (from 0.132 W/A at 20°C to 0.099 W/A at 120°C). A subtle hysteresis loop started to appear when the working temperature exceeded 60°C, confirming that the losses associated with the SA section increase with increasing temperature [7]. For a better comparison of device performance at different temperatures, the dependence of J_{th} on V_{rev} and temperature is plotted in Fig. 4.1 (b). As depicted, the V_{rev} applied in the SA section

has a more significant effect on J_{th} for higher temperatures, and this is consistent with the observation reported by other researchers [7]. I also compare the thermal performance for both the ridged waveguide structure (solid line in Fig. 4.1 (b)) and the tapered structure (dashed line in Fig. 4.1 (b)) devices with the same SA-to-Gain length ratio. It is obvious that the devices with tapered structure exhibit a slightly higher J_{th} than the ridged waveguide structure due to the larger area of the gain section [13]. It should be mentioned that the tapered structure devices were not tested beyond 100°C due to the current source restriction (I_{max} = 1 A).
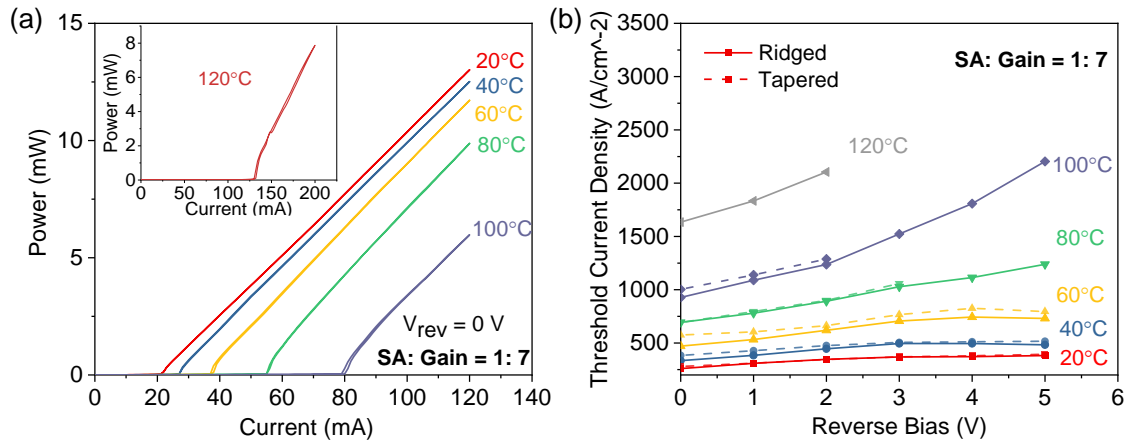

Figure 4.1 (a) Typical temperature-dependent L-I curves of a 25.5 GHz two-section QD MLL when $V_{rev} = 0$ V. (b) Threshold current density (J_{th}) as a function of V_{rev} for both the ridged waveguide structure and tapered structure at different temperatures.

Figure 4.2 presents the temperature dependence of the J_{th} for both structures. The calculated T_0 values of the ridged waveguide and tapered structures from the J_{th} changes were 55 and 63 K, respectively. I noticed that regardless of the J_{th} changes with the V_{rev}, T_0 remains almost identical in each structure, confirming that the value of T_0 is primarily dependent on the properties of the gain section [9]. Moreover, the higher value of T_0 extracted from the tapered structure implies that its I_{th} is less sensitive to temperature, and this improved heat dissipation of the tapered structure can be attributed to the larger area of the resonator [14]. Attention must be paid that for such a tapered device, the junction-side down mounting is normally required to solve the heat accumulation problem, which enables operation at a higher I_{gain} level. Moreover, a broader gain section

may also suffer from higher order mode effects [15]. Therefore, our investigations mainly focus on the ridged waveguide structure.
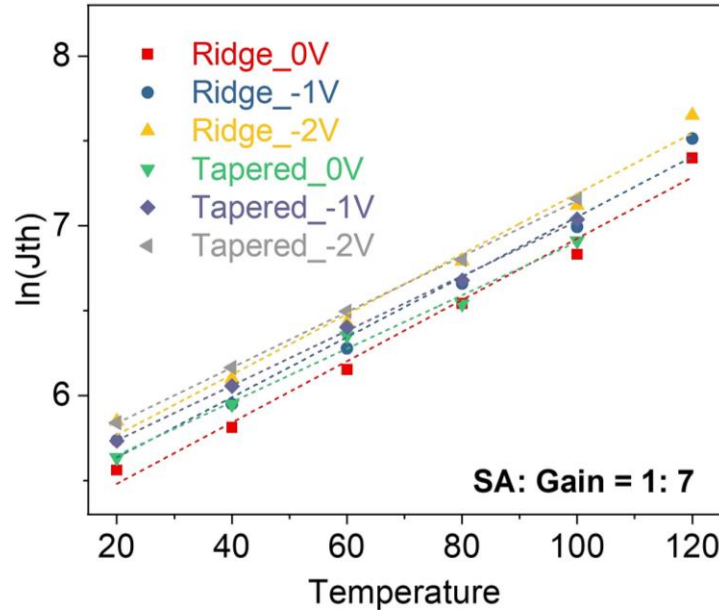

Figure 4.2 Plotting of J_{th} in natural logarithmic scale against various temperatures for both ridged waveguide structure and tapered structure.

Figure 4.3 (a - e) show the range of working temperature for the ridged waveguide QD MLLs with SA-to-gain length ratios varying from 1: 3 to 1: 7. The plot of the corresponding J_{th} versus temperature for all ratios at V_{rev} = 0 V is summarised in Fig. 4.3 (f) for the purpose of comparison. As expected, the longer device tends to operate in a wider temperature range with a broader range of driving conditions. Although the longest device (SA: Gain = 1: 7) can operate up to 120°C with ease, no lasing behaviour could be achieved in the shortest device (SA: Gain = 1: 3) when the temperature exceeds 60°C. This can be explained by the fact that the reduced threshold gain in the longer cavity is easier to be saturated than in the shorter ones [16]. Moreover, the calculated T_0 values for the SA-to-Gain length ratio ranging from 1: 3 to 1: 7 are 41 K, 43 K, 50 K, 54 K, and 55 K, respectively. These results further confirm that the device with a longer cavity length exhibits better thermal stability. Thus, the device configurations with a ratio of 1: 7 (i.e., the longest laser cavity) was selected as the most promising candidate for a detailed temperature characteristics study.
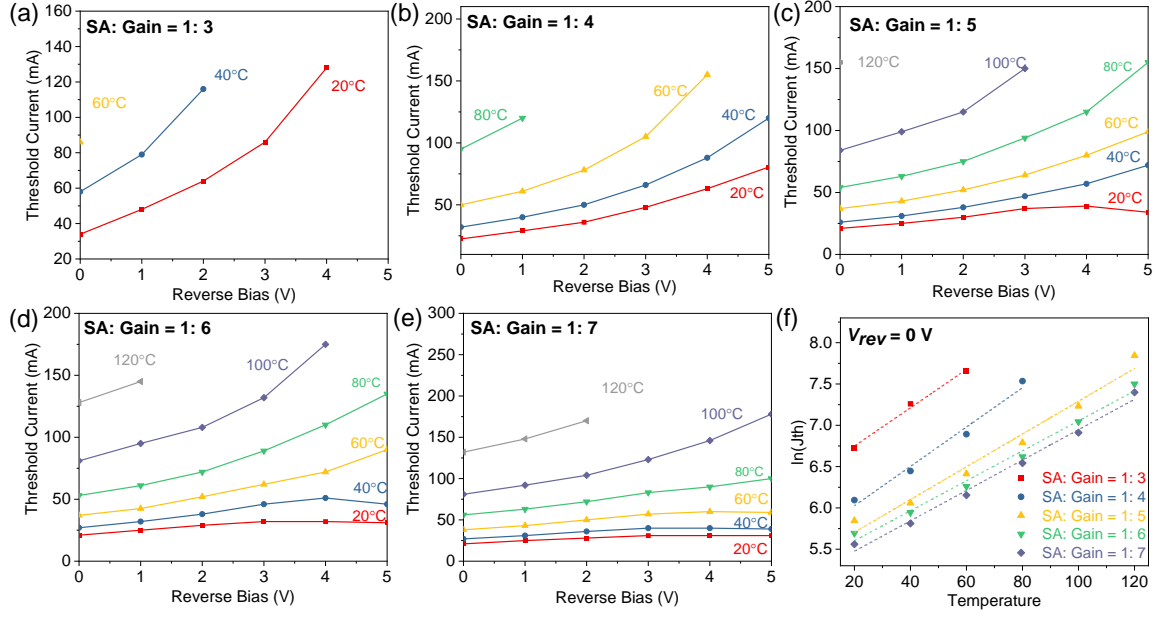
Figure 4.3 (a – e) Dependence of threshold current on V_{rev} and operating temperature for ridged waveguide QD MLLs with SA-to-gain length ratio vary from 1: 3 to 1: 7. (f) Plotting of Jth in natural logarithmic scale versus operating temperatures for different configurations when $V_{rev} = 0$ V.

4.2.2 RF Spectra Measurements

The RF spectra measurements were first carried out to determine the stable mode-locking regime. For better comparison, the V_{rev} was fixed at -2 V throughout the testing process, and the optimal driving currents were identified when the shortest τ_p occurs at the given temperature. After evaluations, the driving currents for heatsink temperatures at 20, 40, 60, 80, 100, and 120°C were 49, 60, 64.7, 85, 148.5, and 210 mA, respectively. As seen in Fig. 4.4 (a), the stable mode-locking operation has been achieved over an extended temperature range from 20°C to 120˚C, with a clear RF peak at ~ 25.5 GHz, absence of RF power at low frequencies, and the SNR well above 30 dB. Figure 4.4 (b) displays the zoom-in view of RF peaks presented in Fig. 4.4 (a), and the Fig. 4.4 (c) highlights the change of the f_{rep}. According to those graphs, it can be easily found that the mode spacing of our QD MLL suffers from a tiny variation (only 0.07 GHz) over the 100˚C temperature range. The main reason behind this phenomenon is the interplay between the thermal expansion of the laser cavity and the temperature-induced changes in the refractive index [7]. As already discussed in Chapter 1, the f_{rep}

reflects the round-trip cavity time that is ultimately determined by the cavity length and the refractive index. The temperature increment will lead to thermal expansion of the cavity length, subsequently resulting in a reduction in the mode spacing. On the other hand, the refractive index of the semiconductor material for a given wavelength decreases with increasing temperature, bringing an expansion in the tone spacing [17]. Not to mention that the red-shift of emission wavelength caused by increased temperature could further diminish the refractive index and accentuate the expansion of two adjacent modes [18]. The nearly unchanged value of f_{rep} suggests that the effect of temperature on thermal expansion of the laser cavity and the change of refractive index is well balanced, and such stable f_{rep} at various ambient temperatures is a desirable feature in optical communications. Besides, with the SA section biased at a constant level (-2 V in this case), the stable mode-locking over the whole temperature range was obtained by tuning the I_{gain} only, which yields an extra benefit of easy-operation and bias simplicity.
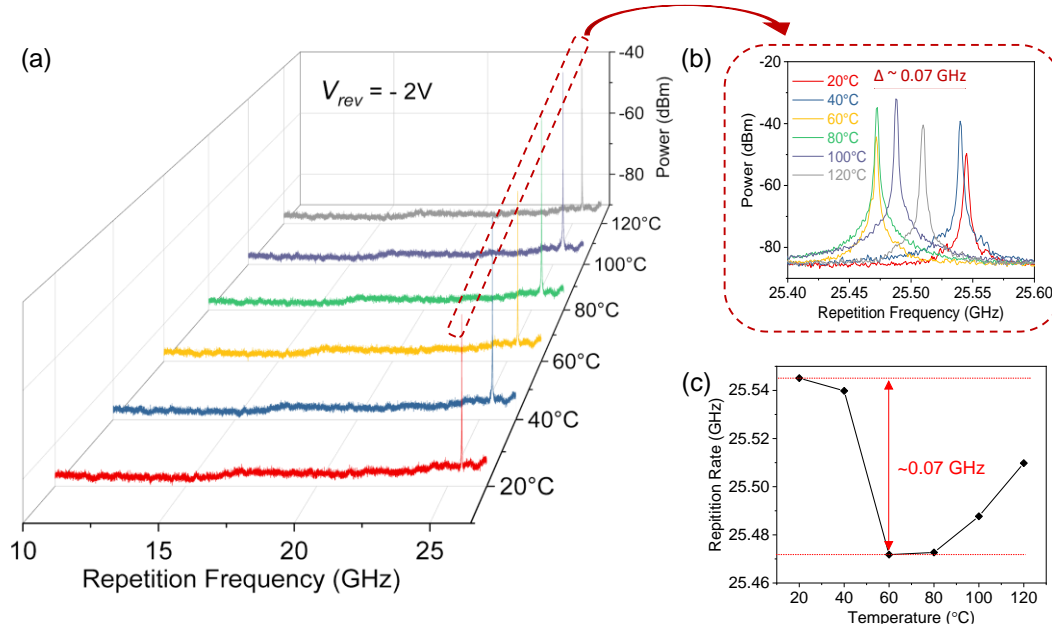

Figure 4.4 (a) Temperature-dependent RF spectra for the two-section ridged waveguide QD MLL with SA: Gain = 1: 7. The V_{rev} is fixed at -2 V and I_{gain} is 49, 60, 64.7, 85, 148.5, and 210 mA at 20, 40, 60, 80, 100, and 120°C, respectively. (b) Zoom-in RF spectra for (a). (c) Plot of the f_{rep} value as a function of operating temperature.

4.2.3 OSA Spectra Measurements

For a laser device, the GS lasing benefits from low I_{th}, low power consumption, and high WPE, and therefore, it is normally more preferred than the ES emission. However, in high-temperature operation, the GS gradually becomes saturated, and the thermally activated carriers may escape to the nearby ES1 due to the electronic state filing effect, resulting in a wavelength switch from the GS to the ES1 transition [19-22]. This phenomenon occurs more notably if the quantised energy separation (ΔE) between the GS and the ES1 was relatively small. Figure 4.5 (left) presents the measured optical spectra as a function of temperature under the same driving conditions used for corresponding RF spectra measurements. A successive red-shift of the emission wavelength with increasing temperature has been observed, revealing that the mode-locking operation of our device is exclusively from the GS thoroughly. To the best of our knowledge, this is the first demonstration of a QD-MLL emitting solely from its GS up to 120°C without any cooling system among all types of QD-MLLs. Such an excellent performance can be ascribed to the aforementioned specially-designed wafer layer structure. The ten stacked QD layers in the active region could prevent gain saturation, thereby allowing the GS lasing to be maintained at high temperature [23]. At the same time, the InAs QDs were directly grown on GaAs. This increases the confinement potential and generates an energy separation of 88 meV between the GS and the ES1, effectively suppressing the carrier overflow and improving the temperature performance [24]. The measured intensities at 20, 60, and 120°C have been re-plotted in the log scale, shown on the right-hand side of Fig. 4.5. It can be seen in more detail that the central emission wavelength of this laser device first locates at 1294.034 nm at 20°C, then moves to 1317.918 nm at 60°C, and further shifts to 1366.448 nm at 120°C. Once again, the GS lasing up 120°C can be confirmed by such a steady redshift in the absolute emission wavelength. Meanwhile, the 3-dB bandwidth is found to be almost temperature independent with average OSNR level well above 25 dB: from 3.81 nm at 20°C to 3.054 nm (21 lines) at 120°C. Using chirped QDs [25], QD intermixing [26], or hybrid quantum well/QD structures [27] could further improve the optical bandwidth. In addition, the symmetry of the

optical spectrum, created by the delta function-like density of states and the random size distribution of the dots [28], indicates a near-zero LEF at these temperatures [29]. Indeed, the absolute wavelength of the device changes with operating temperature (~ 0.7 nm/°C), which is unwanted for practical comb applications. It has been suggested that by carefully tailoring the QD structure together with the laser cavity length, i.e., achieving an optimum cavity design for a given gain function, it would be possible to realise an extremely small change in the wavelength of each comb line with temperature [30].
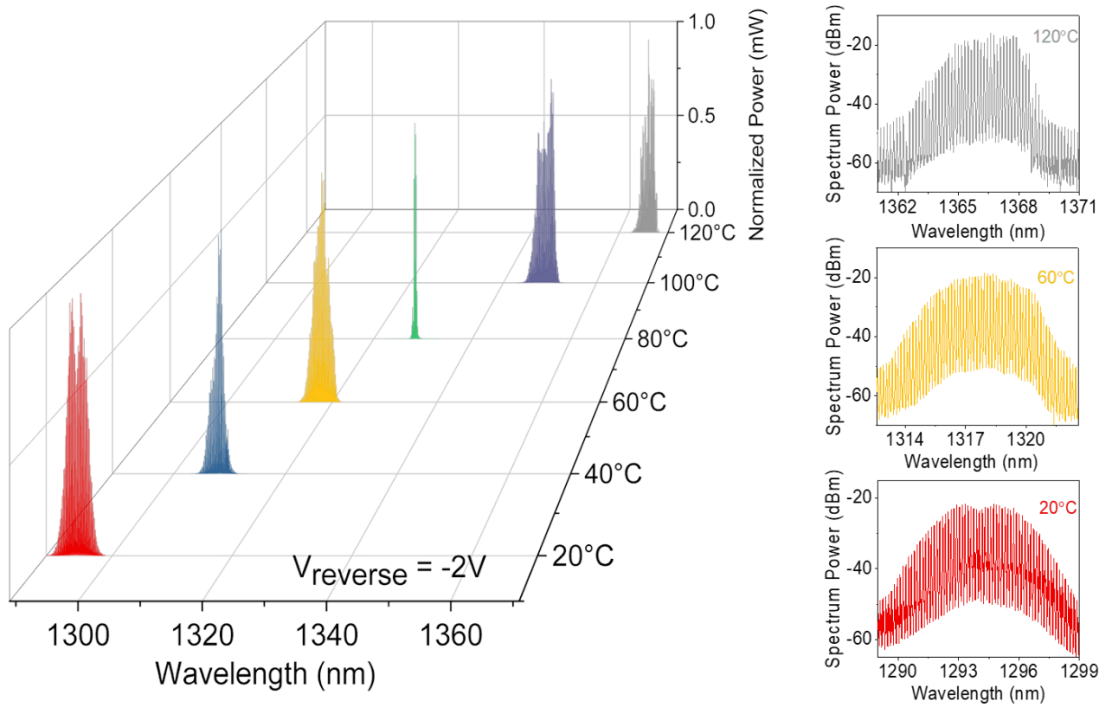

Figure 4.5 Left: measured optical spectra over temperature from 20°C to 120°C for the same operating conditions used in Fig. 4.4. Right: replotted optical spectra in log scale for 20°C, 60°C, and 120°C.

4.2.4 Regime of Mode-locking

Figure 4.6 displays a series of colour maps depicting the stable mode-locking regions for heatsink temperature from 20°C to 120°C. For the stable mode-locking performance, in general, the fundamental RF peak SNR larger than 25 dB and the corresponding τ_p narrower than 9 ps are required [3]. As seen, a wide mode-locking area was demonstrated at 20°C with the I_{gain} ranging from 30 to 120 mA

and the V_{rev} ranging from -1 to -7 V. Although a temperature-related shrinking of the achievable mode-locking range was witnessed, it is indeed possible to observe a fairly broad mode-locking region even at temperatures as high as 120°C. Moreover, the fundamental RF peak SNR for most of the recorded mode-locking states is larger than 30 dB, suggesting the good mode-locking quality across the entire temperature measurement range. It should be pointed out that as the range of driving conditions used for testing was underestimated, the actual mode-locking range at each temperature should be broader than indicated.
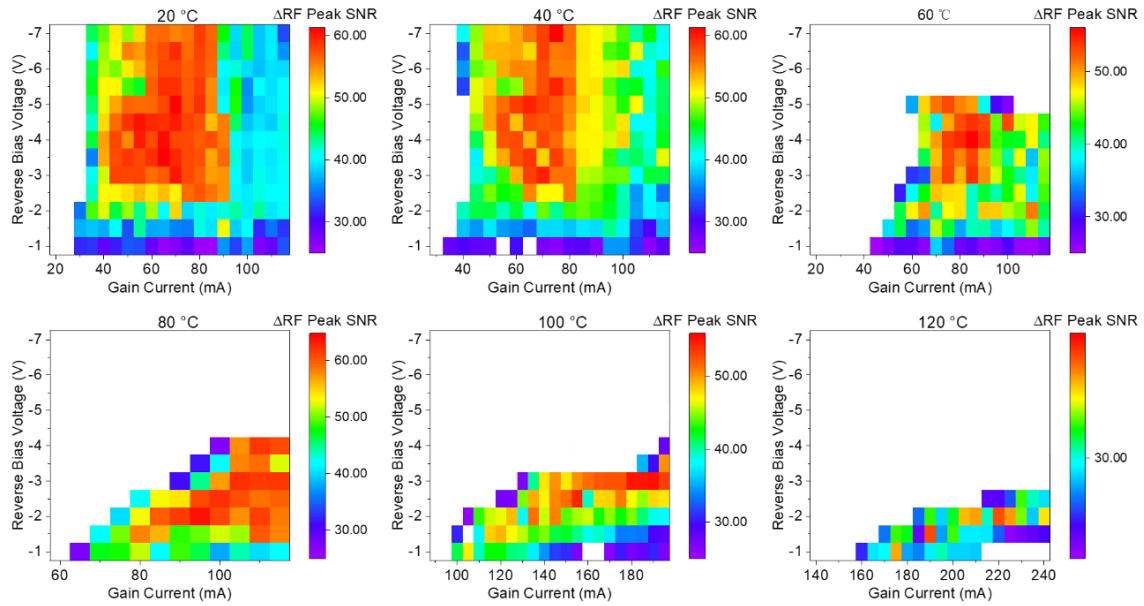

Figure 4.6 Fundamental RF peak SNR mapping as a function of I_{gain} and V_{rev} from 20°C to 120°C under mode-locking operation.

4.2.5 Noise Figure

To determine whether our QD MLL is a suitable OFC source for DWDM optical communications in wide temperature range, the OSA spectrum and RIN measurements at a high temperature of 100°C was conducted. The coherent comb spectrum at 100°C under the bias conditions of I_{gain} = 148.5 mA and V_{rev} = −2 V is shown in Fig. 4.7 (a), whose centre emission wavelength (~ 1349 nm) is well located inside the telecom O-band, and the corresponding fundamental RF peak SNR is ~ 48 dB under this condition. The square-like optical spectrum has a 3.884

nm 3-dB bandwidth (4.81 nm of 6-dB bandwidth), providing a maximum of 26 (31 tones within 6 dB) potential channels with an OSNR larger than 36 dB [0.1 nm ASE noise bandwidth]. The measured average absolute power for individual channels within the 3-dB bandwidth is around -18 dBm, which is comparable to previous observations measured at room temperature [31]. The measured RIN spectrum of the whole optical combs is displayed in Fig. 4.7 (b), from which the integrated average RIN value is less than -146 dBc/Hz between 0.5 GHz and 10 GHz. Although it is difficult to estimate the exact transmission capacity of this comb laser source until an advanced system-level WDM experiment is carried out, as a guideline, it is anticipated that the transmission capacity could exceed 1.664 Tbit/s if all 26 channels were employed as optical carriers and adopted the 32 Gbaud PAM-4 modulation [31-33].
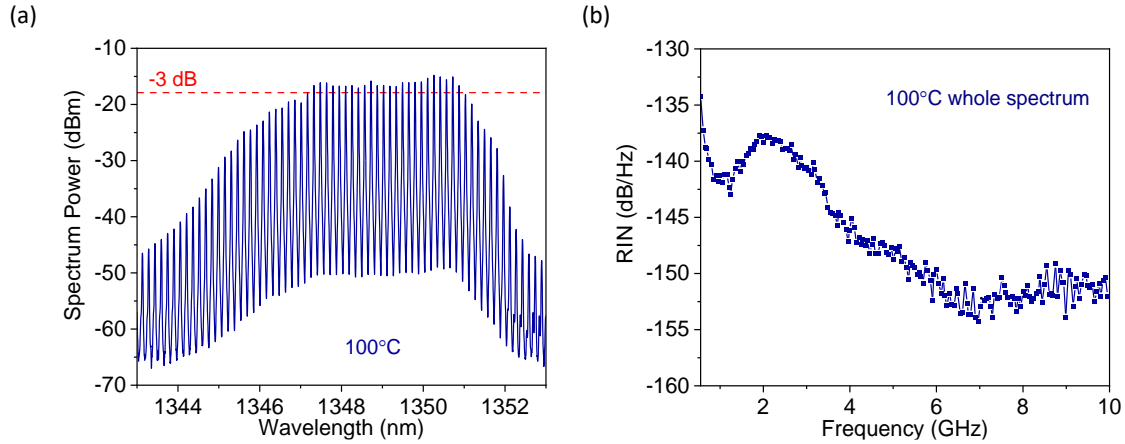

Figure 4.7 (a) Optical spectrum under bias conditions of I_{gain} = 148.5 mA and V_{rev} = − 2 V at 100℃. (b) RIN spectrum for the whole optical comb is shown in (a) from 0.5 to 10 GHz.

4.3 Conclusion

In this section, the temperature-dependent performance of various QD MLL configurations was studied. And I found that the laser device with a smaller SA-to-Gain length ratio (i.e., longer cavity length) could operate in a broader temperature range under wider driving conditions. The reason is that for a fixed SA section length, a longer gain section is harder to be saturated with injected photons. Also, the tapered device tends to have better thermal stability than the ridged waveguide

device owing to its greater heat dissipation capability, this is in great agreement with the findings in ref [34]. I also demonstrated a QD MLL based 25.5 GHz OFC source that could be potentially used in the DWDM systems at elevated temperature. Although plenty of excellent results have been reported in previous high-temperature studies on QD MLLs, their devices either exhibited unstable mode-locking operation over 70°C [7] or switched to the ES1 at 92°C [8]. More importantly, none of them can be employed in the DWDM applications since their fundamental repetition rates (20 and 5 GHz, respectively) don't meet the minimum requirement of the ITU-T recommendation (i.e., 25 GHz) [35]. The superior temperature characteristics of our devices are believed to be realised from the high QD density and the large ΔE between the GS and the ES1, resulting from the specially engineered epitaxial structure. Besides, the test results proved that with a constant V_{rev}, stable mode-locking can be achieved by simply changing the injected current in the gain section, and this adds an extra benefit to device operation. Furthermore, the QD MLL based comb source shows a broad optical bandwidth even at an elevated temperature of 100°C (with a 3-dB bandwidth of 3.884 nm, offering a maximum of 26 optical channels), and the OSNR value of each tone is more than 36 dB. The corresponding low integrated average RIN value of −146 dBc/Hz in the 0.5 - 10 GHz range indicates that this device is capable of multi-Tbit/s transmission. Our findings suggest that the two-section passively InAs QD MLLs could be a promising candidate of ultra-stable and easy-operating OFC sources for low-power-consumption, high-capacity, and low-cost optical data communications over wide operating temperature range.

4.4 Reference

[1]   P. Marin-Palomo *et al.*, "Microresonator-based solitons for massively parallel coherent optical communications," *Nature,* vol. 546, no. 7657, pp. 274-279, 2017.

[2]   L. Lundberg *et al.*, "Phase-coherent lightwave communications with frequency combs," *Nature communications,* vol. 11, no. 1, pp. 1-7, 2020.

[3]   S. Pan *et al.*, "Quantum dot mode-locked frequency comb with ultra-stable 25.5 GHz spacing between 20° C and 120° C," *Photonics Research,* vol. 8, no. 12, pp. 1937-1942, 2020.

[4]   R. Antil, S. B. Pinki, and S. Beniwal, "An overview of DWDM technology & network," *Int. J. Sci. Technol. Res,* vol. 1, no. 11, pp. 43-46, 2012.

[5]   Y. Arakawa and H. Sakaki, "Multidimensional quantum well laser and temperature dependence of its threshold current," *Appl Phys Lett,* vol. 40, no. 11, pp. 939-941, 1982.

[6]   K. Nishi, K. Takemasa, M. Sugawara, and Y. Arakawa, "Development of quantum dot lasers for data-com and silicon photonics applications," *IEEE Journal of Selected Topics in Quantum Electronics,* vol. 23, no. 6, pp. 1-7, 2017.

[7]   M. A. Cataluna, E. U. Rafailov, A. D. McRobbie, W. Sibbett, D. A. Livshits, and A. R. Kovsh, "Stable mode-locked operation up to 80 degrees C from an InGaAs quantum-dot laser," (in English), *Ieee Photonic Tech L,* vol. 18, no. 13-16, pp. 1500-1502, Jul-Aug 2006, doi: 10.1109/Lpt.2006.877589.

[8]   J. K. Mee *et al.*, "A passively mode-locked quantum-dot laser operating over a broad temperature range," (in English), *Appl Phys Lett,* vol. 101, no. 7, Aug 13 2012, doi: 10.1063/1.4746266.

[9]   M. A. Cataluna, E. U. Rafailov, A. McRobbie, W. Sibbett, D. A. Livshits, and A. Kovsh, "Stable mode-locked operation up to 80/spl deg/C from an InGaAs quantum-dot laser," *Ieee Photonic Tech L,* vol. 18, no. 14, pp. 1500-1502, 2006.

[10]   M. Laemmlin *et al.*, "Distortion-free optical amplification of 20-80 GHz modelocked laser pulses at 1.3/spl mu/m using quantum dots," *Electron Lett,* vol. 42, no. 12, pp. 697-699, 2006.

[11]   G. Park, O. B. Shchekin, and D. G. Deppe, "Temperature dependence of gain saturation in multilevel quantum dot lasers," *Ieee J Quantum Elect,* vol. 36, no. 9, pp. 1065-1071, 2000.

[12]   A. Patane, A. Polimeni, M. Henini, L. Eaves, P. Main, and G. Hill, "Thermal effects in quantum dot lasers," *Journal of applied physics,* vol. 85, no. 1, pp. 625-627, 1999.

[13]   B. Sumpf *et al.*, "High brightness 735 nm tapered lasers–optimisation of the laser geometry," *Optical and quantum electronics,* vol. 35, no. 4, pp. 521-532, 2003.

[14]   M. Kelemen *et al.*, "Tapered diode lasers at 976 nm with 8 W nearly diffraction limited output power," *Electron Lett,* vol. 41, no. 18, pp. 1011-1013, 2005.

[15]   A. Mar, R. Helkey, W. Zou, D. B. Young, and J. E. Bowers, "High‑power mode‑locked semiconductor lasers using flared waveguides," *Appl Phys Lett,* vol. 66, no. 26, pp. 3558-3560, 1995.

[16]   O. á. Shchekin and D. Deppe, "1.3 μm InAs quantum dot laser with T o= 161 K from 0 to 80 C," *Appl Phys Lett,* vol. 80, no. 18, pp. 3277-3279, 2002.

[17]   J. McCaulley, V. Donnelly, M. Vernon, and I. Taha, "Temperature dependence of the near-infrared refractive index of silicon, gallium arsenide, and indium phosphide," *Physical Review B,* vol. 49, no. 11, p. 7408, 1994.

[18]   D. Marple, "Refractive index of GaAs," *Journal of Applied Physics,* vol. 35, no. 4, pp. 1241-1242, 1964.

[19]   G. Park, D. Huffaker, Z. Zou, O. Shchekin, and D. Deppe, "Temperature dependence of lasing characteristics for long-wavelength (1.3-μm) GaAs-based quantum-dot lasers," *Ieee Photonic Tech L,* vol. 11, no. 3, pp. 301-303, 1999.

[20]   X. Huang, A. Stintz, C. Hains, G. Liu, J. Cheng, and K. Malloy, "Very low threshold current density room temperature continuous-wave lasing from a single-layer InAs quantum-dot laser," *Ieee Photonic Tech L,* vol. 12, no. 3, pp. 227-229, 2000.

[21]   R. Mirin, A. Gossard, and J. Bowers, "Room temperature lasing from InGaAs quantum dots," *Electron Lett,* vol. 32, no. 18, p. 1732, 1996.

[22]   A. Markus, J. Chen, C. Paranthoen, A. Fiore, C. Platz, and O. Gauthier-Lafaye, "Simultaneous two-state lasing in quantum-dot lasers," *Appl Phys Lett,* vol. 82, no. 12, pp. 1818-1820, 2003.

[23]   T. Kageyama *et al.*, "Long-wavelength quantum dot FP and DFB lasers for high temperature applications," in *Novel In-Plane Semiconductor Lasers XI*, 2012, vol. 8277: SPIE, pp. 73-80.

[24]   O. B. Shchekin, G. Park, D. L. Huffaker, and D. G. Deppe, "Discrete energy level separation and the threshold temperature dependence of quantum dot lasers," *Appl Phys Lett,* vol. 77, no. 4, pp. 466-468, 2000.

[25]   L. Li, M. Rossetti, A. Fiore, L. Occhi, and C. Velez, "Wide emission spectrum from superluminescent diodes with chirped quantum dot multilayers," *Electron Lett,* vol. 41, no. 1, pp. 41-43, 2005.

[26]   K. Zhou *et al.*, "Quantum dot selective area intermixing for broadband light sources," *Optics Express,* vol. 20, no. 24, pp. 26950-26957, 2012.

[27]   S. Chen *et al.*, "GaAs-based superluminescent light-emitting diodes with 290-nm emission bandwidth by using hybrid quantum well/quantum dot structures," *Nanoscale Research Letters,* vol. 10, no. 1, pp. 1-8, 2015.

[28]   T. Newell, D. Bossert, A. Stintz, B. Fuchs, K. Malloy, and L. Lester, "Gain and linewidth enhancement factor in InAs quantum-dot laser diodes," *Ieee Photonic Tech L,* vol. 11, no. 12, pp. 1527-1529, 1999.

[29]   P. K. Kondratko, S.-L. Chuang, G. Walter, T. Chung, and N. Holonyak Jr, "Observations of near-zero linewidth enhancement factor in a quantum-well coupled quantum-dot laser," *Appl Phys Lett,* vol. 83, no. 23, pp. 4818-4820, 2003.

[30]   F. Klopf, S. Deubert, J. Reithmaier, and A. Forchel, "Correlation between the gain profile and the temperature-induced shift in wavelength of quantum-dot lasers," *Appl Phys Lett,* vol. 81, no. 2, pp. 217-219, 2002.

[31]   S. T. Liu *et al.*, "High-channel-count 20 GHz passively mode-locked quantum dot laser directly grown on Si with 4.1 Tbit/s transmission capacity," (in English), *Optica,* vol. 6, no. 2, pp. 128-134, Feb 20 2019, doi: 10.1364/Optica.6.000128.

[32]   G. Liu et *al.*, "Passively mode-locked quantum dash laser with an aggregate 5.376 Tbit/s PAM-4 transmission capacity," *Optics express,* vol. 28, no. 4, pp. 4587-4593, 2020.

[33]   S. Pan *et al.*, "Multi-wavelength 128 Gbit s− 1 λ− 1 PAM4 optical transmission enabled by a 100 GHz quantum dot mode-locked optical frequency comb," *Journal of Physics D: Applied Physics,* vol. 55, no. 14, p. 144001, 2022.

[34]   Y.-L. Cao, P.-F. Xu, H.-M. Ji, T. Yang, and L.-H. Chen, "High brightness InAs/GaAs quantum dot tapered laser at 1.3 μm with high temperature stability," in *Semiconductor Lasers and Applications IV*, 2010, vol. 7844: SPIE, pp. 19-27.

[35]   I.-T. Recommendations. "Spectral grids for WDM applications: DWDM frequency grid." https://handle.itu.int/11.1002/1000/14498 (accessed.

Chapter 5 Multi-wavelength 128 Gbit s^{-1} λ^{-1} PAM4 optical transmission enabled by a 100 GHz quantum dot mode-locked OFC

5.1 Introduction

The past two decades have witnessed the exploding traffic volume, which motivated the study of fibre-optic and free-space optic (FSO) transmissions as it can increase the capacity of communication systems while decreasing deployment costs of existing photonic networks [1].

For fibre-optic communication, the DWDM technology is considered as one of the most promising solutions to meet the ever-increasing demand for bandwidth and future high-speed transmission systems [2]. The ITU-T G.694.1 has recommended a variety of spectral grids ranging from 12.5 to 100 GHz for DWDM applications [3]. Among all proposed spectral grids, the wider one ($\geq$ 100 GHz) is always more desired in the DWDM transmission systems since it may reduce the total number of required light sources. Unfortunately, achieving a high gain in an ultimate short cavity is particularly challenging for QD materials [4]. For this reason, almost all previous QD-based mode-locked OFCs obtaining large mode-spacing involved either a complicated system-level setup [5] or high-order harmonic mechanisms [6-8], as summarised in Table 5.1. Also, while the most high-performance QD-MLLs operate at the telecom C-band, those devices working at the telecom O-band are relatively immature. However, boosting the transmission capacity of existing photonic networks requires the employment of telecom O-band as the conventional C-band has been extensively exploited [9].

In addition, the traditional datacentre networks normally require miles of fibre-optic

cables for communication interconnects, which are complex, high-power consumption, and limited by latency problems [10, 11]. The employment of the FSO communication system could get rid of the bulky cabling systems and provide us with a better latency in a higher data rate communication system. Such a low latency is particularly important for realising future space-air-ground-ocean (SAGO) FSO communication networks [12]. Moreover, the QD-MLL based FSO transmission system opens the avenue for one-to-many communications, since the QD-MLL is highly integrative and can effectively replace many discrete laser devices in high-speed optical communication systems [13, 14]. Even though the FSO research is still evolving, especially for those on telecom O-band, extending the fibre transmission to the FSO transmission not only seems a natural step, but also one that is relatively straightforward to take.

Table 5.1 Summary of QD mode-locked OFC source with ultra-high repetition rate.

Telecom Band	Repetition Rate (GHz)	Material	Methods	Pulse Duration (ps)	-3dB Bandwidth (nm)	Year/Ref.
C-band	134	InGaAsP/InAs QDash	Single section	0.8	4.3	2006/ [15]
O-band	117	InGaAs QD	CPM - 3rd harmonic	2.14	-	2006/ [6]
	238		CPM - 6th harmonic	1.3	-	
C-band	92	InAs/InP QD	Single section	0.312	11.62	2008/ [16]
C-band	10-100	InAs/InP QD	Single section	0.295	17.9	2010/ [17]
	437		FBGs	0.810	-	
O-band	100	InGaAs/GaAs QD	Mode-selections	-	-	2010/ [18]
O-band	100	InGaAs/GaAs QD	Fabry-Perot Etalon	-	-	2011/ [5]
O-band	102	QD	CPM - 6th harmonic	-	-	2018/ [7]
O-band	100	Chirped QD	CPM - 5th harmonic	2.3	-	2019/ [8]
O-band	**94**	**InGaAs/GaAs QD**	**Two-Section**	**0.69**	**3.18**	**This Work**

* CPM: colliding pulse mode-locking, FBG: fibre Bragg grating.

In Chapter 4, I proved that our fabricated QD-MLLs have great thermal stability

and can be potentially utilised as optical carriers in data transmission systems. The aim of this chapter is to report the transmission ability of a multi-wavelength ~ 100 GHz Fourier-transform-limited OFC source generated by a passively two-section InAs QD-MLL with a floating SA section. In section 5.2, the state-of-the-art epitaxial structure and device design are presented. In section 5.3, the basic device characteristics including the *L-I-V* curve, mode-locking performance, device stability, and the RIN performance are covered. Based on the promising results shown in section 5.3, system-level data transmission experiments through both fibre and free-space are demonstrated and analysed in section 5.4. Finally, in section 5.5, all measured results are summed up, and the impact of our device on future high-speed optical data transmission systems is discussed.

5.2 Material growth and device design

As mentioned in Chapter 2, the wafer used in this project was also prepared by solid-state MBE on a GaAs substrate, with an emission wavelength in the 1.3 µm range. The specific epitaxial structure can be found in ref [19]. As a matter of fact, increasing the number of QD layers will gradually build up the internal strain within the crystal, degrading the quality of the InAs/GaAs QDs wafer [20]. To achieve the high modal gain required for ultra-short cavity length, eight self-organised QD layers comprise the active region. In each QD layer, the InAs QDs were directly grown on the GaAs surface and capped by the InGaAs strain-reducing layer. As the compressive stress is partially relaxed inside the QDs, light emission at a longer wavelength can be expected [21-23]. Figure 5.1 (a) shows the room temperature PL spectrum of the eight-stacked QDs. The lasing wavelength and the FWHM of the PL spectrum were ~ 1.3 µm and 28 meV, respectively. The PL linewidth is strongly influenced by the distribution of dot sizes; such a small value means that a great dot uniformity has been accomplished. The inset of Fig. 5.1 (a) shows the cross-section TEM images of the QD active region and the zoomed-in view of a single dot. As seen, the typical dimensions of truncated pyramidal shaped QDs are 20-25 nm in base length and 6-8 nm in height.

Figure 5.1 (b) presents the schematic diagram of the QD-MLL under investigation. A 5-µm-wide ridge was designed to maintain a single-transverse-mode operation [24]. Based on the previously obtained group effective index of 3.7, the cavity length was set to be 405 µm to realise ~ 100 GHz mode-spacing, of which the SA section accounted for 14% (56.7 µm). Such design of an ultimately short cavity laser allows us to achieve a comparably high differential loss in the SA section while achieving a relatively small differential gain in the gain section, resulting in a large gain-to-SA saturation energy ratio [25]. This is crucial in realising stable mode-locking with a floating SA section. An electrical isolation resistance of ~ 2.5 kΩ was achieved between the SA and gain sections via citric wet etching. Later, the facet close to the SA section was coated with a 95% high-reflective coating, whereas the facet near the gain section remained uncoated.
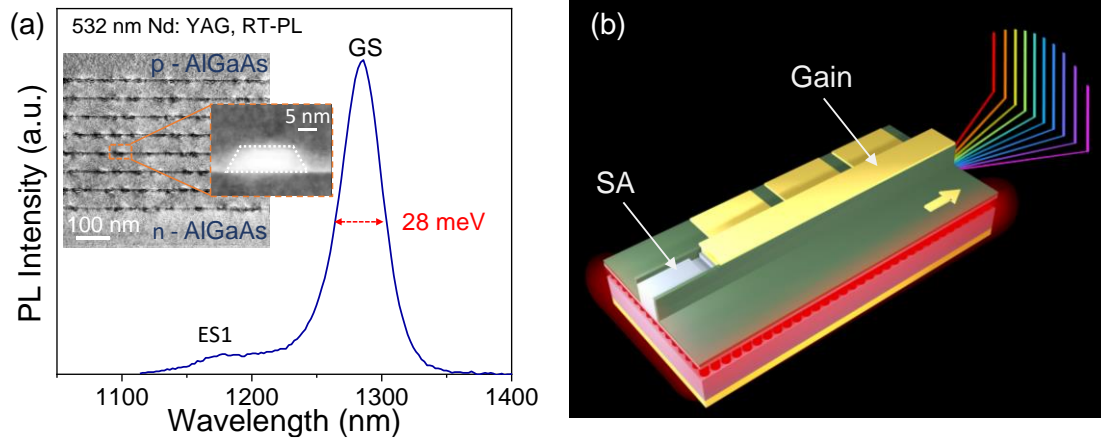

Figure 5.1 (a) The PL spectrum of the sample at room temperature. (Inset: The bright-field scanning TEM image of the QD active region and a single dot (zoom-in)). (b) Schematic diagram of the 100 GHz passively two-section QD-MLL with the floating SA section [19].

5.3 Passive mode-locking performance

The *L-I-V* curve for the fabricated QD-MLL at room temperature is presented in Fig 5.2 (a). To prevent device damage under a high-power density condition, the injected current is limited to 80 mA. As can be observed, the device has a 20-mA threshold current and 17.7% slope efficiency. An inconspicuous hysteresis loop occurs near the I_{th}, indicating the bistability nature of the device even when the SA

section was left floating [25]. Normally, the semiconductor lasers with ultra-short cavity lengths suffer from poor heat dissipation, which leads to excessive heating and eventually causes the device to shut off [26, 27]. Hence, with the help of Mr Jie Yan from the NOEIC in Wuhan, China, the fabricated devices were packaged in a high-speed 14-pin package with a TEC controller to minimise the temperature impacts on device performance (shown in Fig. 5.2 (c) & (d)). The heat-sink temperature was fixed at 20°C for all measurements. In this work, the mode-locking phenomenon was obtained without applying V_{rev} to the SA section (i.e., the minimal absorption will not affect the self-mode-locking mechanism), and hence, those devices operated similarly to a single-section self-mode-locked laser [28, 29]. Though the butterfly package can easily yield repeatable results for the same driving condition, it brings an unwanted power penalty caused by the coupling loss between the QD-MLL and the lensed fibre. As exhibited in Fig. 5.2 (b), the energy loss before and after the butterfly package is 3 dB. Although the value of I_{th} stays almost same, the slope efficiency drops from 17.7% to 9.1% after packaging. Meanwhile, the maximum WPE from one facet degrades from ~8% to ~4%. Therefore, the ideal performance of our devices should be much better than the test results presented in the following sections.
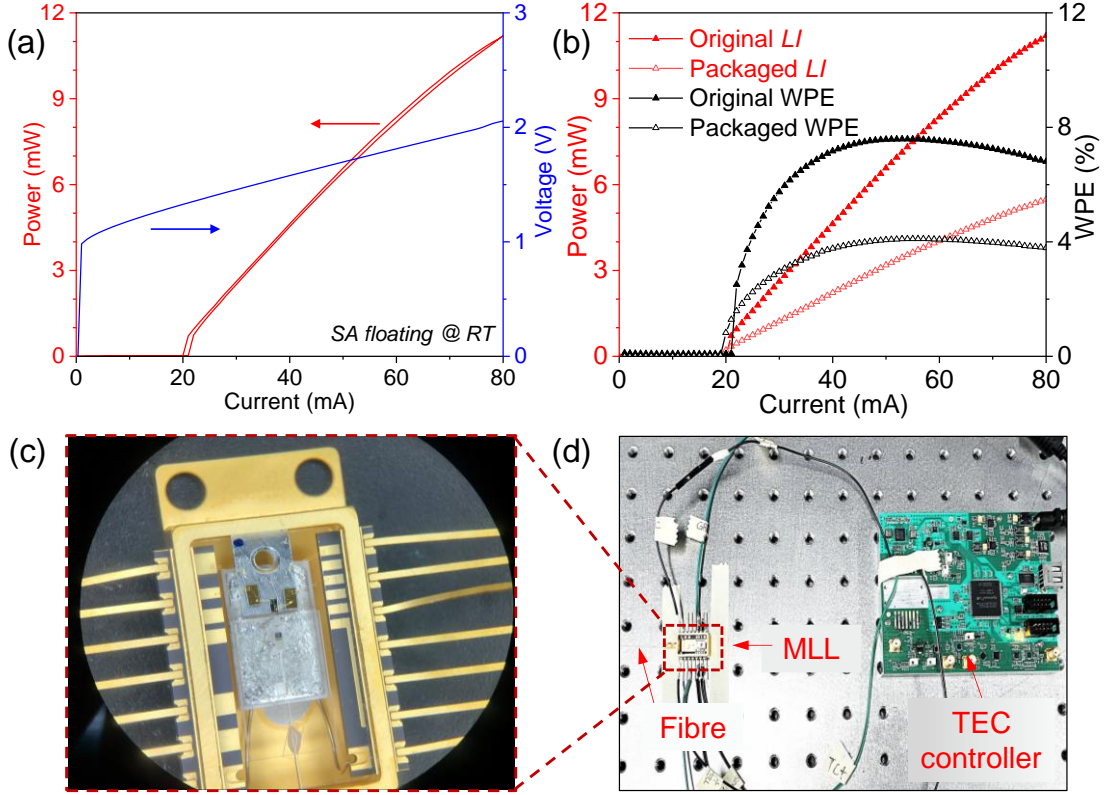
Figure 5.2 (a) The RT C.W. L-I-V curve for two-section QD-MLL with the SA left floating. (b) L-I and WPE comparisons of the device before (closed markers) and after packaging (open markers). (c) Microscope image of the two-section QD-MLL in butterfly package. (d) Photo image showing the connections between the packaged device and the TEC controller for temperature-control purposes.

Due to the fact that finding an ESA with a detection range over 100 GHz was difficult, the f_{rep} of our device was derived from the mode-spacing between adjacent tones. I used a 0.04-pm-resolution OSA (apex, AP2087A) for precise evaluations. The high-resolution optical spectrum of three tones located near the central wavelength at 66 mA is shown in Fig. 5.3 (a). Because of the 30-μm cleave error, a mode-spacing of 0.5248 nm is obtained, corresponding to a fundamental f_{rep} of 94.6 GHz. To the best of our knowledge, this is the largest fundamental mode-spacing ever achieved by a passively two-section QD-MLL in a telecom O-band. The autocorrelation signal displayed in Fig. 5.3 (b) confirms the stable mode-locking behaviour at I_{gain} = 66 mA. Without any external pulse-compression scheme, the measured pedestal-free pulse profile agrees reasonably well with the fitted Gaussian pulse shape, showing a τ_p of 648 fs.
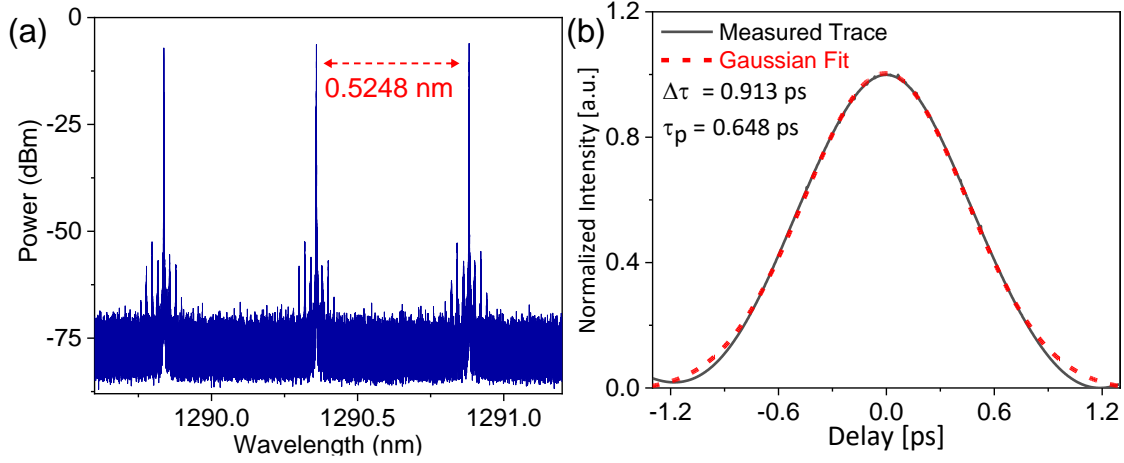
Figure 5.3 (a) High-resolution OSA spectrum for adjacent tones (resolution: 0.04 pm). (b) Measured intensity autocorrelation trace with Gaussian pulse fitting.

The mode-locking performances of the packaged 100 GHz two-section QD-MLL are highlighted in Fig. 5.4. While the trend observed in the OSA spectrum for I_{gain} increment is visualised in Fig. 5.4 (a), Figure 5.4 (b) and (c) summarise the relevant parameters under different driving conditions. As expected, a continuously red-shift of centre wavelength (from 1288 to 1293 nm) has been witnessed when I_{gain} increased from 20 to 80 mA (Fig. 5.4 (b)), confirming the sustained GS lasing of the laser device. Moreover, at a higher current level, the OSA spectrum shows a tendency to become a multi-peak structure with an extra peak occurring in the high-frequency side, which may result from the enhanced self-phase modulation caused by increasing carrier density [30]. As a result, the OSA spectral width expands steadily from 1.6 to 4.3 nm during the test range. As already discussed in the previous chapters, I believe that such a current-induced red-shift of emission wavelength could be reduced by adjusting the QDs structure [31, 32]. Figure 5.4 (c) shows the τ_p derived at each current level and the corresponding calculated TBP values. In most cases, the τ_p is sensitive to the driving conditions, and the narrowest pulse is usually observed at high V_{rev} and low I_{gain} [25, 33-35]. Unusually, some research groups have reported the shortest τ_p generated under the condition of high V_{rev} and I_{gain} well beyond the I_{th} [36, 37]. However, neither of these trends applies to our case, where a continuous pulse shortening mechanism

only relies on I_{gain} increment, without the need for a voltage source. One possible explanation is the change in the short-pulse generation mechanism within the two-section lasers [38, 39]. I obtain the shortest τ_p of ~ 474 fs at the largest current value in the test range. Meanwhile, the small fluctuation of the calculated TBP with an average value of 0.472 indicates that the generated pulses were almost Fourier-transform-limited over the entire mode-locking regime.
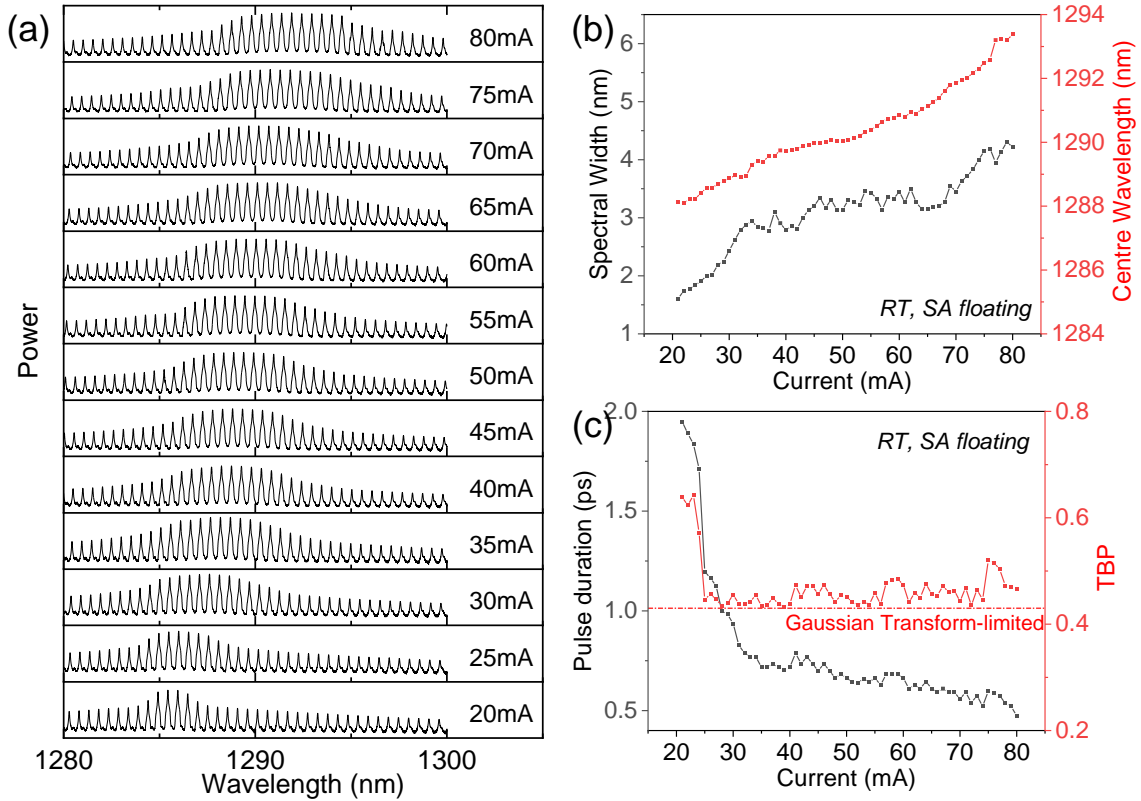

Figure 5.4 RT characteristics of two-section QD-MLL with floating SA section and the I_{gain} ranging from 20 to 80 mA. (a) OSA spectra with a resolution of 0.02 nm. (b) Spectral width and the centre wavelength as a function of I_{gain}. (c) τ_p and the corresponding calculated TBP value at different current injection levels.

Figure 5.5 depicts the specific QD-MLL performance at room temperature under I_{gain} = 66 mA, chosen as it is neither too large to introduce severe thermal effect, nor too small to produce insufficient output power. The stability of output power of this OFC source is revealed in Fig. 5.5 (a). During the 1-hour test, the average output power was kept around +7.17 dBm with a small variation of 0.06 dB. The OSA spectrum under this condition is shown in Fig. 5.5 (b), where a centre

wavelength of 1290.755 nm and a reasonably broad 3-dB bandwidth (~ 3.46 nm) can be found. The inset image of Fig. 5.5 (b) clearly shows that the 3-dB bandwidth consists of 7 optical carriers in order from the short-wavelength to the long-wavelength, namely tone 1: 1289.8 nm, tone 2: 1290.32 nm, tone 3: 1290.84 nm, tone 4: 1291.36 nm, tone 5: 1291.88 nm, tone 6: 1292.4 nm, and tone 7: 1292.92 nm. The OSNR of those tones is well above 55 dB (0.1 nm ASE noise bandwidth), which is much higher than our previous results [40]. The corresponding RIN spectra of the laser device and the individual central modes are shown in Fig. 5.5 (c). As seen, an integrated average RIN value of -152.172 dB Hz^{-1} is obtained for the QD MLL range from 100 MHz to 10 GHz. The relaxation resonance frequency of the device is defined as its RIN peak, which is located at 3.76 GHz. Regarding the relatively low power of filtered individual tones, an external O-band PDFA was employed before the RIN measurements. With the help of the PDFA, the power of each filtered tone was pumped to ~ +5 dBm and the low-frequency mode partition noise was suppressed [41]. Consequently, the integrated average RIN values for each isolated mode all lie within the range of -134.955 ~ -139.179 dB Hz^{-1}. According to previous studies, such RIN values are sufficiently low and suitable for high-speed transmission systems with advanced modulation formats [34, 42, 43].
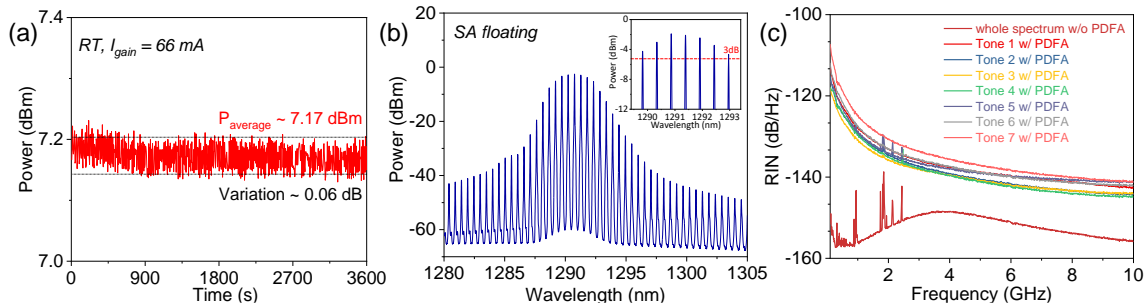

Figure 5.5 Device characteristics at I_{gain} = 66 mA. (a) The stability of output power of QD-MLL for 3600 s. (b) Optical combs at room temperature. (Inset: the zoom-in showing 7 tones within the 3-dB bandwidth). (c) The measured RIN of the whole spectrum and the certain filtered channel in (b).

5.4 Data transmission performance

To verify the suitability of our QD-MLLs in practical high-speed data transmission applications, system-level WDM experiments were carried out under the help of

Mr Dingyi Wu from the NOEIC. In section 5.4.1, the data transmission over B2B and 5 km SSMF fibre with either 64 Gbaud NRZ (64 Gbit s-1) or 64 Gbaud PAM-4 (128 Gbit s-1) modulation signals is performed. An analysis of individual channel uniformity and the signal degradation in the fibre-optic transmission is done by plotting measured BER curves against received optical powers. In our work, an algorithm developed by Dr Hongguang Zhang is used to extract accurate BER values from the collected data. In addition, to explore a wider range of application possibilities, a free-space optical (FSO) transmission was demonstrated in section 5.4.2.5.4.1 Fibre transmission

Figure 5.6 shows the experimental setup for the data transmission over fibre. Every wavelength channel of the OFC generated by the packaged QD-MLL was selected as an optical carrier by an OBPF. The power of filtered tone was amplified to > 10 dBm by an O-band PDFA. As already stated in Chapter 2, due to the large insertion loss of the filter, the 2nd OBPF usually placed after the PDFA was omitted. The polarisation state of the transmitted light in single-mode fibre was controlled by a PC, after which the maximum signal intensity could be obtained. The data modulation was achieved using a 40 GHz lithium niobate MZM driven by an AWG, in which a 2^{15}-1 PRBS with a length of 32767 bits was generated at 64 Gbaud in either PAM-4 or NRZ format. Then, the modulated optical signal propagated through B2B and 5 km SSMF. Immediately after transmission, an additional PDFA was used to ensure a measurable signal power level for the equipment afterwards. A more detailed description of the experimental setup has been illustrated in section 2.3.4. Table 5.2 summarises the power levels measured at the points marked in Fig 5.6, as well as the insertion loss associated with each step. As can be noted, the insertion losses caused by the OBPF (-14 dB) and the MZM (-10 dB) are of most concern, and the coupling loss of 3 dB due to packaging also cannot be ignored. Therefore, it can be deduced that with better packaging methods and more advanced laboratory equipment, improved transmission performance can be expected.
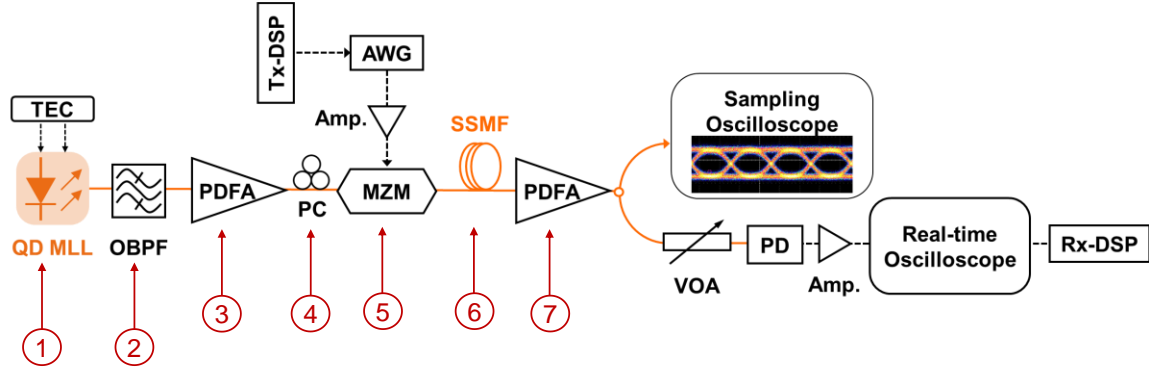
Figure 5.6 Experimental setup for data transmission over fibre.

Table 5.2 Summary of insertion loss in the optical-fibre transmission setup.

Measured Point	1	2	3	4	5	6	7
Power (dBm)	+7	-7	+14	+13.5	+3	+2	+5
Loss/Gain (dB)	-3	-14	+22	-0.5	-10	-1	+3

The transmission ability of our QD-MLL is estimated through the BER performance of the seven tones located within the 3-dB bandwidth under I_{gain} = 66 mA (refer to Fig. 5.5 (b)). And the plot of evaluated BER results is used to indicate the differences in performance between channels implemented in diverse modulation formats during the B2B operation. It should be mentioned that the hard-decision forward error correction (HD-FEC) and the soft-decision forward error correction (SD-FEC) in our case represent the 7% overhead and the 20% overhead coding limits for data recovery, respectively [34]. This corresponds to an HD-FEC BER threshold of 3.8×10^{-3} and an SD-FEC BER limit of 2.2×10^{-2} [44]. Within the limits of FEC algorithms, therefore, the data transmission can be considered as error-free [45]. As readily observed in Fig. 5.7, the transmission performance of each tone varies in accordance with the RIN of each mode. Similar behaviours can be found for all involved channels except the two tones located near the edges (tone 1 and tone 7). The plots reveal that the NRZ modulation format is superior to the PAM-4 format in terms of 64 Gbaud B2B transmission system of QD-MLL, mainly due to its lower SNR requirement [46]. The receiver sensitivity for tone 2-6 at BER = 3.8×10^{-3} varies from -1 dBm to -2 dBm with PAM4 signal and differs

from -11.5 dBm to -12 dBm for the NRZ modulation. Therefore, compared with the PMA-4 modulation, the NRZ modulation provides better receiver sensitivity of nearly 10 dB for B2B transmission. Moreover, the curves in Fig. 5.7 show a reasonable consistency of performance between separate tones based on similar slope efficiencies and overlapped points. Figure 5.8 shows the 64 Gbaud PAM-4 corresponding to 128 Gbit/s signal transmission for tone 2 and tone 4 over B2B and 5 km SSMF transmission. The 1 dB power penalties for those two measured tones are primarily due to the impact of fibre chromatic dispersion [47]. No error floor is observed.
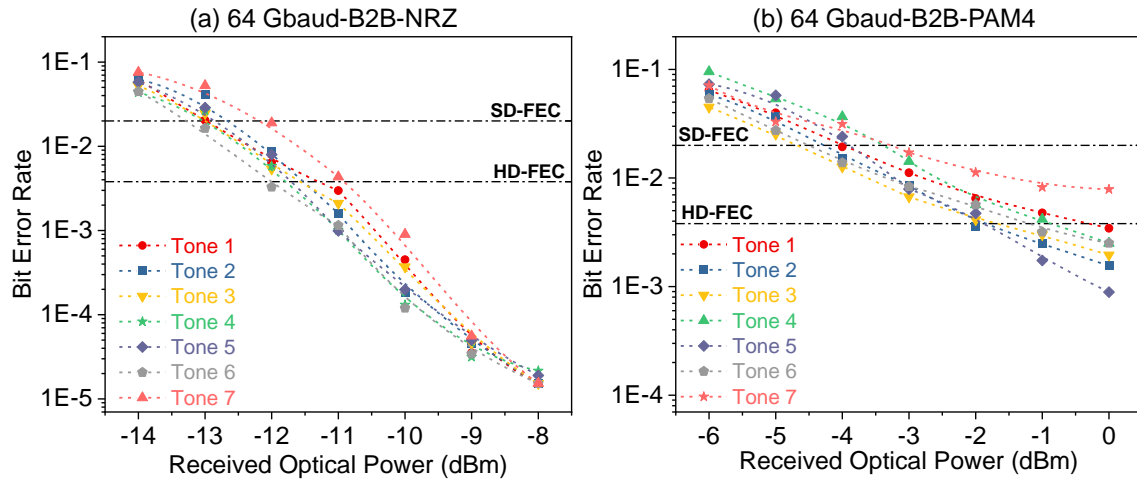
Figure 5.7 The BER characteristics of different combs in the B2B configuration with (a) 64 Gbaud NRZ modulation and (b) 64 Gbaud PAM-4 modulation.
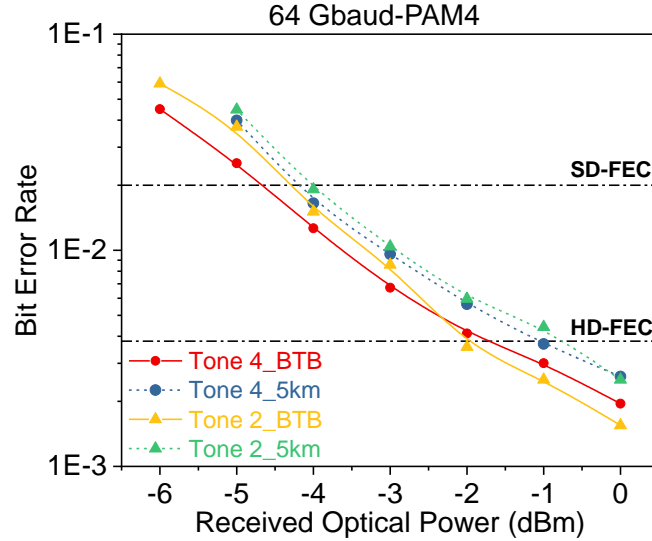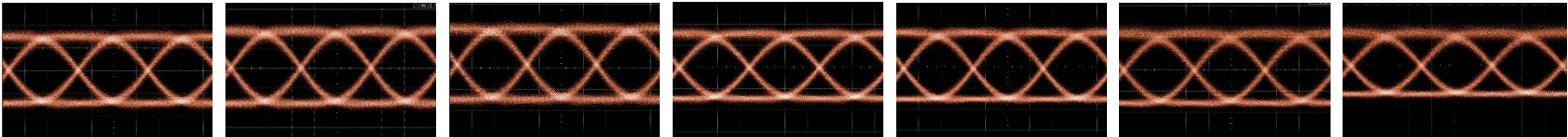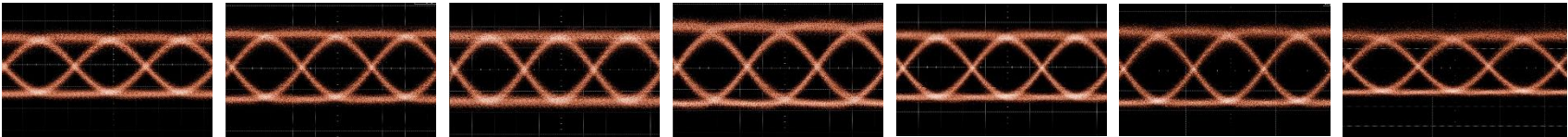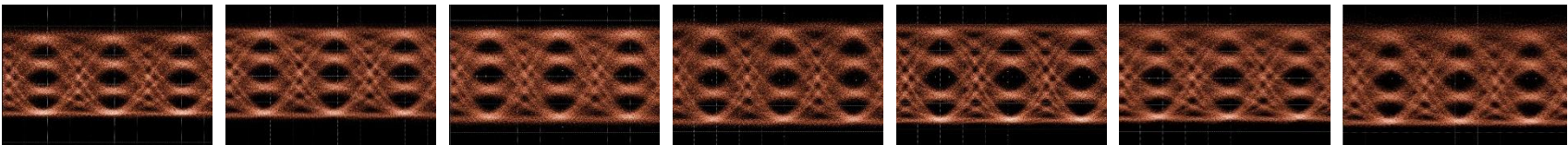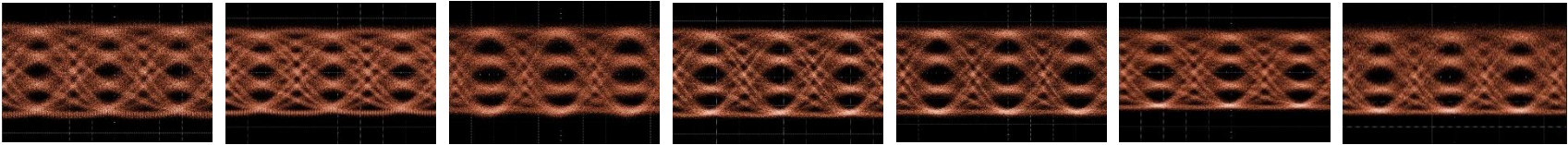
Figure 5.8 The measured BER versus received optical power for B2B and after 5 km SSMF transmission using Tone 2 and Tone 4.

Obviously, the signal suffers from impairments when it travels from a transmitter to a receiver. The optical eye diagram created by an oscilloscope could serve as a common indicator of signal quality in high-speed transmission, allowing us to quickly evaluate system performance and gain insight view of channel imperfections [48]. Table 5.3 displays the corresponding eye diagrams for the seven tones after B2B and 5 km SSMF transmission, in which all measured power is on the order of 0 dBm in the receiver. The NRZ and PAM-4 levels of the modulated signals are clear and can be well recognised, indicating a good uniformity between the selected tones. I also extract the Q-factor for NRZ modulation to describe the signal quality and predict the related BER level. For B2B transmission, the averaged Q-factor is around 10.4, corresponding to a BER value of 1×10^{-25}. After 5 km SSMF transmission, the noisier bit 1 level caused by inter-symbol interference (ISI) reduces the averaged Q-factor to 9.36 and the BER level increases to 4×10^{-21}. It is undeniable that the tones located at the edges tend to have blurrier optical eye diagrams, this is because their power is weaker than the others. Meanwhile, the PAM-4 modulation allows twice as much information to be transmitted per symbol cycle as the NRZ modulation for the same bitrate, making it more stringent on signal intensity. As a result, the overall eye diagrams of PMA-4 will not be as clear as the NRZ at the same modulation rate.

Table 5.3 Optical eye diagrams for different tones after B2B and 5 km SSMF transmission.

64 Gbaud NRZ	Tone 1	Tone 2	Tone 3	Tone 4	Tone 5	Tone 6	Tone 7
B2B							
Q-factor	10.29	10.71	10.28	10.56	11.85	9.78	9.32
5km							
Q-factor	9.08	9.64	9.32	9.28	10.56	8.95	8.68

64 Gbaud PAM-4	Tone 1	Tone 2	Tone 3	Tone 4	Tone 5	Tone 6	Tone 7
B2B							
5km							

5.4.2 Free-space transmission

This section presents the transmission system for FSO communications at the same driving condition used in section 5.4.1 (i.e., I_{gain} = 66 mA and the SA was left floating). The experimental setup for FSO transmission is presented in Fig. 5.9. The average optical power of around +7 dBm was obtained from the packaged QD-MLL, and the expected wavelengths were chosen by OPBF. The first O-band PDFA was used to enhance the output power to ~ +15 dBm, thus compensating for the significant insertion loss caused by the following MZM. Here, the NRZ and the PAM-4 formats were carried at various bit rates, from 30 Gbaud/s to 64 Gbaud/s. After the modulator, the optical beam of the selected wavelength was launched into free-space by a collimator (YXOC-T-1310-SS-5.0-APC) and propagated into a condenser lens (YXOC-C-1310-SS-5.0-APC) at a distance of 2 m. Considering the eye-safety issue, the measured optical power into free-space was limited to 0 dBm [49]. The second O-band PDFA was used immediately after the 2-m FSO transmission in order to provide ~ 10 dB gain to the received signal and ensure enough optical power for subsequent performance evaluations. The amplified signal was then adopted for optical eye-diagram captures and BER analysis. Once again, the Keysight DCA-M N1092A sampling oscilloscope was employed for eye-diagram measurements and the 256 GSa/s Keysight UXR0704A real-time oscilloscope was used to digitalise the detected data signal for the offline DSP process. A detailed description of all involved test equipment was covered in section 2.3.4.
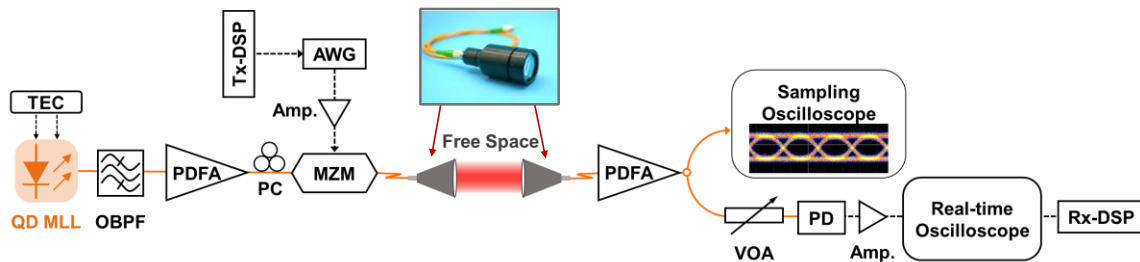

Figure 5.9 Experimental setup for free-space data transmission.

The high-resolution emission spectra of the QD-MLL before and after the 2-m FSO

transmission are obtained in Fig. 5.10 (a). On both OSA spectra, within their 3-dB bandwidth, seven equally distributed tones at wavelengths identical to the ones aforementioned can be observed. Although the OSNR values decrease after the 2-m free-space link due to extra distortion lights introduced to the received optical power, they are still well over 45 dB [50]. Meanwhile, the power of each tone is uniformly reduced by ~ 5 dB after FSO transmission for all wavelengths, indicating good stability of our experimental platform. The tones 2, 4 and 6 were selected as representatives to investigate the FSO transmission capabilities. Before quantifying the reliability of the entire communication system using BER analysis, the optical eye diagrams were first measured to provide a visual representation of the transmission quality for different formats at various modulation rates. Table 5.4 summarises all captured eye diagrams with a constant sampling time scale of 5 ps. As seen, with an increased bit rate, the cycle increases while the size of the eye-opening diminishes. Such a reduction in the eye-opening implies the potential increment of data errors [48]. Meanwhile, the increased number of eye amplitude power levels in the PAM-4 format leads to a significant decrease in level separation, introducing a considerable deterioration in transmission quality [49]. As a result, the PAM-4 eye-diagrams tend to be blurrier than the NRZ eye-diagrams for the same data rate.

The comparison of BER performance after B2B and 2-m FSO transmission is exhibited in Fig. 5.10 (b). For the 64 Gbaud NRZ signal, performances below HD-FEC were achieved with an average received power of -11.25 dBm for 2-m FSO transmission and -11.75 dBm for B2B configuration. This means that the power penalty for each tone is tolerable and is around 0.5 dB. Here, the degradation of the BER value is mainly caused by the decline of OSNR and the divergent focal spot size [51]. Despite only three frequency combs being demonstrated, all seven tones can be implemented by this scheme.
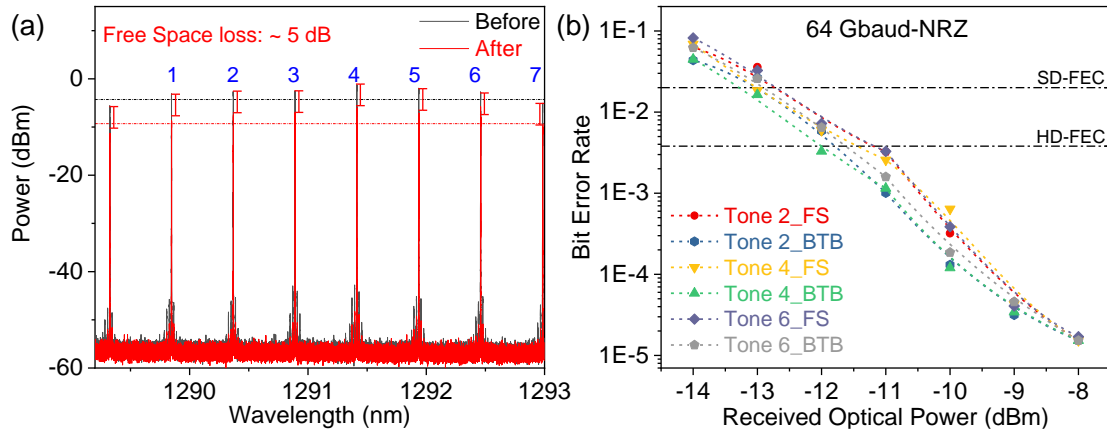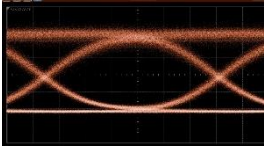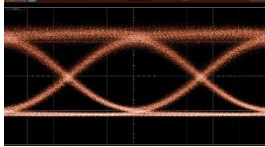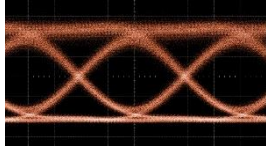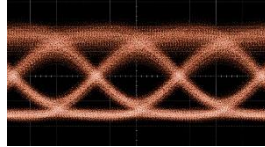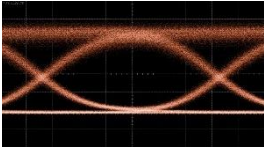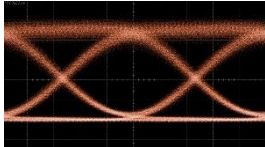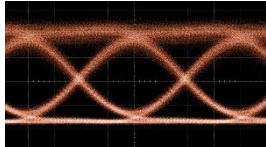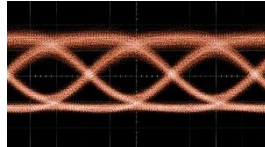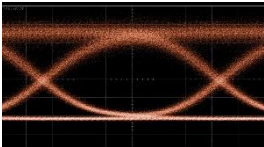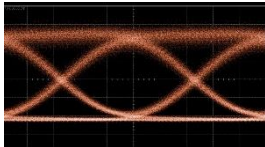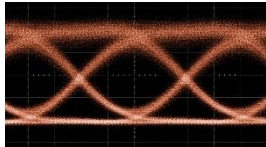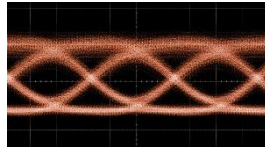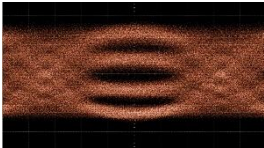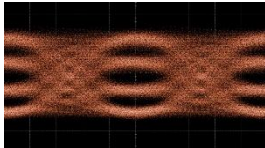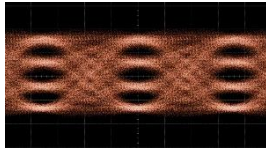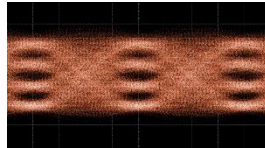
Figure 5.10 (a) High-resolution OSA spectra showing the output power of individual tone before and after the 2-m free-space transmission. (b) The BER performance of filtered tone after B2B and 2-m free-space transmission.

Table 5.4 Optical eye diagrams for different tones after 2-m FSO transmission.

NRZ	30 Gbaud	40 Gbaud	56 Gbaud	64 Gbaud
Tone 2				
Tone 4				
Tone 6				

PAM-4	30 Gbaud	40 Gbaud	56 Gbaud	64 Gbaud
Tone 4				

5.5 Conclusion

In this chapter, a high-performance wide-spaced OFC source generated by a passively two-section InAs QD-MLL has been successfully demonstrated. As a consensus in the field of optoelectronic communications, the QD-MLLs-based OFC sources with a larger mode-spacing are more preferred due to their capability of potentially diminishing the total number of required light sources in the DWDM transmission systems. Despite the fact that a wide variety of 100 GHz comb sources are currently available via high order harmonics [6-8] or complicated system-level setups [5], it is still difficult to obtain such large mode-spacing combs by the fundamental repetition rate of a QD-MLL, mainly attribute to the shortage of high-gain materials needed for extreme-short cavities.

Here, we report a QD-MLL lasing from a cavity length as short as 405 µm, corresponding to a 100 GHz fundamental repetition rate. The high dot density and good QDs uniformity resulting from the optimised growth conditions played an essential role in ensuring the high-performance operation of the devices. Also, thanks to the carefully designed SA-to-gain length ratio, the mode-locking was observed with the current source only, whereas the SA section was left floating. Such a structure could provide a great convenience in device operation. Meanwhile, the nearly-transform-limited pulses were detected within the entire test range, indicating a high pulse quality of our QD-MLLs. The excellent noise performance with a typical integrated average RIN value of less than -134 dB Hz^{-1} was obtained over the frequency range from 100 MHz to 10 GHz. Seven tones were selected as optical carriers to carry out the system-level data transmission experiments via 5-km SSMF or 2-m free space. Our 100 GHz QD-MLLs succeed in realising up to 64 Gbaud PAM-4 (128 Gbit s^{-1}) fibre transmission and up to 64 Gbaud NRZ FSO transmission. The measured optical eye-diagrams in conjunction with the BER plots suggest that our QD-MLL is feasible to handle high-speed optical data transmission with promising

transmission capacities. Hence, our proposed two-section QD-MLL could be a compelling candidate as a compact, low power consumption, easy-operation, cost-efficient, and integratable light source in the future high-speed optical communication networks.

5.6 Reference

[1]   K. Zeb *et al.*, "Broadband Optical Heterodyne Millimeter Wave-over-Fiber Wireless Links Based on a Quantum Dash Dual-Wavelength DFB Laser," *Journal of Lightwave Technology,* 2022.

[2]   R. Antil, S. B. Pinki, and S. Beniwal, "An overview of DWDM technology & network," *Int. J. Sci. Technol. Res,* vol. 1, no. 11, pp. 43-46, 2012.

[3]   ITU-T. "Spectral grids for WDM applications: DWDM frequency grid." (accessed.

[4]   A. Ukhanov, A. Stintz, P. Eliseev, and K. Malloy, "Comparison of the carrier induced refractive index, gain, and linewidth enhancement factor in quantum dot and quantum well lasers," *Appl Phys Lett,* vol. 84, no. 7, pp. 1058-1060, 2004.

[5]   N. Yamamoto, Y. Yoshioka, K. Akahane, T. Kawanishi, H. Sotobayashi, and H. Takai, "100-GHz channel spacing and O-band quantum dot optical frequency comb generator with interference injection locking technique," in *CLEO: Science and Innovations*, 2011: Optical Society of America, p. CTuV7.

[6]   A. Rae *et al.*, "Harmonic mode-locking of a quantum-dot laser diode," in *LEOS 2006-19th Annual Meeting of the IEEE Lasers and Electro-Optics Society*, 2006: IEEE, pp. 874-875.

[7]   G. Kurczveil, C. Zhang, A. Descos, D. Liang, M. Fiorentino, and R. Beausoleil, "On-chip hybrid silicon quantum dot comb laser with 14 error-free channels," in *2018 IEEE International Semiconductor Laser Conference (ISLC)*, 2018: IEEE, pp. 1-2.

[8]   S. Liu *et al.*, "100 GHz colliding pulse mode locked quantum dot lasers directly grown on Si for WDM application," in *CLEO: Applications and Technology*, 2019: Optical Society of America, p. ATu3P. 5.

[9]   N. Yamamoto, Y. Omigawa, K. Akahane, T. Kawanishi, and H. Sotobayashi, "Simultaneous 3× 10 Gbps optical data transmission in 1-μm, C-, and L-wavebands over a single holey fiber using an ultra-broadband photonic transport system," *Optics Express,* vol. 18, no. 5, pp. 4695-4700, 2010.

[10]   B. Shariati, A. Bogris, P. Dijk, C. Roeloffzen, I. Tomkos, and D. Syvridis, "Free Space Intra-Datacenter Interconnection Utilizing 2D Optical Beam Steering," in *Optical Fiber Communication Conference*, 2018: Optical Society of America, p. Tu2I. 7.

[11]   H. Dahrouj, A. Douik, F. Rayal, T. Y. Al-Naffouri, and M.-S. Alouini, "Cost-effective hybrid RF/FSO backhaul solution for next generation wireless systems," *IEEE Wireless Communications,* vol. 22, no. 5, pp. 98-104, 2015.

[12]   J. Tan, Z. Zhao, Y. Wang, Z. Zhang, J. Liu, and N. Zhu, "12.5 Gb/s multi-channel broadcasting transmission for free-space optical communication based on the optical frequency comb module," *Optics express,* vol. 26, no. 2, pp. 2099-2106, 2018.

[13]   A. K. Majumdar, *Advanced free space optics (FSO): a systems approach*. Springer, 2014.

[14]   Z. Lu *et al.*, "An L-band monolithic InAs/InP quantum dot mode-locked laser with femtosecond pulses," *Optics Express,* vol. 17, no. 16, pp. 13609-13614, 2009.

[15]   C. Gosset *et al.*, "Subpicosecond pulse generation at 134 GHz using a quantum-dash-based Fabry-Perot laser emitting at 1.56 μ m," *Appl Phys Lett,* vol. 88, no. 24, p. 241105, 2006.

[16]   Z. Lu, J. Liu, S. Raymond, P. Poole, P. Barrios, and D. Poitras, "312-fs pulse generation from a passive C-band InAs/InP quantum dot mode-locked laser," *Optics Express,* vol. 16, no. 14, pp. 10835-10840, 2008.

[17]   Z. Lu *et al.*, "Ultra-high repetition rate InAs/InP quantum dot mode-locked lasers," *Opt Commun,* vol. 284, no. 9, pp. 2323-2326, 2011.

[18]   N. Yamamoto, K. Akahane, T. Kawanishi, R. Katouf, and H. Sotobayashi, "Quantum dot optical frequency comb laser with mode-selection technique for 1-μm waveband photonic transport system," *Japanese Journal of Applied Physics,* vol. 49, no. 4S, p. 04DG03, 2010.

[19]   S. Pan *et al.*, "Multi-wavelength 128 Gbit s$-$ 1 $\lambda-$ 1 PAM4 optical transmission enabled by a 100 GHz quantum dot mode-locked optical frequency comb," *Journal of Physics D: Applied Physics,* vol. 55, no. 14, p. 144001, 2022.

[20]   T. Sugaya *et al.*, "Tunnel current through a miniband in InGaAs quantum dot superlattice solar cells," *Solar energy materials and solar cells,* vol. 95, no. 10, pp. 2920-2923, 2011.

[21]   K. Nishi, K. Takemasa, M. Sugawara, and Y. Arakawa, "Development of quantum dot lasers for data-com and silicon photonics applications," *IEEE Journal of Selected Topics in Quantum Electronics,* vol. 23, no. 6, pp. 1-7, 2017.

[22]   K. Nishi, H. Saito, S. Sugou, and J.-S. Lee, "A narrow photoluminescence linewidth of 21 meV at 1.35 µm from strain-reduced InAs quantum dots covered by In 0.2 Ga 0.8 As grown on GaAs substrates," *Appl Phys Lett,* vol. 74, no. 8, pp. 1111-1113, 1999.

[23]   H. Saito, K. Nishi, and S. Sugou, "Influence of GaAs capping on the optical properties of InGaAs/GaAs surface quantum dots with 1.5 µm emission," *Appl Phys Lett,* vol. 73, no. 19, pp. 2742-2744, 1998.

[24]   R. Scheps, "Introduction to laser diode-pumped solid state lasers," *Tutorial texts in optical engineering,* 2002.

[25]   M. G. Thompson, A. R. Rae, M. Xia, R. V. Penty, and I. H. White, "InGaAs quantum-dot mode-locked laser diodes," *IEEE Journal of Selected Topics in Quantum Electronics,* vol. 15, no. 3, pp. 661-672, 2009.

[26]   A. Abdollahinia *et al.*, "Temperature stability of static and dynamic properties of 1.55 µm quantum dot lasers," *Optics express,* vol. 26, no. 5, pp. 6056-6066, 2018.

[27]   C.-Z. Ning, "Semiconductor nanolasers and the size-energy-efficiency challenge: a review," *Advanced Photonics,* vol. 1, no. 1, p. 014002, 2019.

[28]   E. Sooudi *et al.*, "Injection-locking properties of InAs/InP-based mode-locked quantum-dash lasers at 21 GHz," *Ieee Photonic Tech L,* vol. 23, no. 20, pp. 1544-1546, 2011.

[29]   H. Asghar, W. Wei, P. Kumar, E. Sooudi, and J. G. McInerney, "Stabilization of self-mode-locked quantum dash lasers by symmetric dual-loop optical feedback," *Optics Express,* vol. 26, no. 4, pp. 4581-4592, 2018.

[30]   G. P. Agrawal and N. A. Olsson, "Self-phase modulation and spectral broadening of optical pulses in semiconductor laser amplifiers," *Ieee J Quantum Elect,* vol. 25, no. 11, pp. 2297-2306, 1989.

[31]   L. Seravalli, M. Minelli, P. Frigeri, P. Allegri, V. Avanzini, and S. Franchi, "The effect of strain on tuning of light emission energy of InAs/InGaAs quantum-dot nanostructures," *Appl Phys Lett,* vol. 82, no. 14, pp. 2341-2343, 2003.

[32]   J. D. Thomson, H. D. Summers, P. M. Smowton, E. Herrmann, P. Blood, and M. Hopkinson, "Temperature dependence of the lasing wavelength of InGaAs quantum dot lasers," *Journal of applied physics,* vol. 90, no. 9, pp. 4859-4861, 2001.

[33]   M. Thompson *et al.*, "Subpicosecond high-power mode locking using flared waveguide monolithic quantum-dot lasers," *Appl Phys Lett,* vol. 88, no. 13, p. 133119, 2006.

[34] S. T. Liu *et al.*, "High-channel-count 20 GHz passively mode-locked quantum dot laser directly grown on Si with 4.1 Tbit/s transmission capacity," (in English), *Optica,* vol. 6, no. 2, pp. 128-134, Feb 20 2019, doi: 10.1364/Optica.6.000128.

[35] M. Kuntz *et al.*, "35 GHz mode-locking of 1.3 μ m quantum dot lasers," *Appl Phys Lett,* vol. 85, no. 5, pp. 843-845, 2004.

[36] D. I. Nikitichev *et al.*, "High-power passively mode-locked tapered InAs/GaAs quantum-dot lasers," *Applied Physics B,* vol. 103, no. 3, pp. 609-613, 2011.

[37] M. Thompson, R. Penty, and I. White, "Regimes of mode-locking in tapered quantum dot laser diodes," in *2008 IEEE 21st International Semiconductor Laser Conference*, 2008: IEEE, pp. 27-28.

[38] R. M. Arkhipov, M. Arkhipov, and I. Babushkin, "On coherent mode-locking in a two-section laser," *JETP Letters,* vol. 101, no. 3, pp. 149-153, 2015.

[39] R. Arkhipov, A. Pakhomov, M. Arkhipov, I. Babushkin, and N. Rosanov, "Stable coherent mode-locking based on $$\pi$$ π pulse formation in single-section lasers," *Scientific Reports,* vol. 11, no. 1, pp. 1-13, 2021.

[40] S. Pan *et al.*, "Quantum dot mode-locked frequency comb with ultra-stable 25.5 GHz spacing between 20° C and 120° C," *Photonics Research,* vol. 8, no. 12, pp. 1937-1942, 2020.

[41] K. Sato and H. Toba, "Reduction of mode partition noise by using semiconductor optical amplifiers," *IEEE Journal of Selected Topics in Quantum Electronics,* vol. 7, no. 2, pp. 328-333, 2001.

[42] Z. Lu, "Quantum-dot coherent comb lasers for terabit optical networking systems," in *Integrated Optics: Devices, Materials, and Technologies XXIII*, 2019, vol. 10921: SPIE, pp. 65-74.

[43] N. Eiselt *et al.*, "Real-time 200 Gb/s (4× 56.25 Gb/s) PAM-4 transmission over 80 km SSMF using quantum-dot laser and silicon ring-modulator," in *Optical Fiber Communication Conference*, 2017: Optical Society of America, p. W4D. 3.

[44] H. Zhang *et al.*, "800 Gbit/s transmission over 1 km single-mode fiber using a four-channel silicon photonic transmitter," *Photonics Research,* vol. 8, no. 11, pp. 1776-1782, 2020.

[45] J. Pfeifle *et al.*, "Microresonator-based optical frequency combs for high-bitrate WDM data transmission," in *Optical Fiber Communication Conference*, 2012: Optical Society of America, p. OW1C. 4.

[46]   X. Miao, M. Bi, Y. Fu, L. Li, and W. Hu, "Experimental study of NRZ, Duobinary, and PAM-4 in O-band DML-based 100G-EPON," *Ieee Photonic Tech L,* vol. 29, no. 17, pp. 1490-1493, 2017.

[47]   M. Liao *et al.*, "Low-noise 1.3 μm InAs/GaAs quantum dot laser monolithically grown on silicon," *Photonics Research,* vol. 6, no. 11, pp. 1062-1066, 2018.

[48]   D. Behera, S. Varshney, S. Srivastava, and S. Tiwari, "Eye Diagram Basics: Reading and applying eye diagrams," *EDN Network,* 2011.

[49]   F. Gomez-Agis, S. P. van de Heide, C. M. Okonkwo, E. Tangdiongga, and A. Koonen, "112 Gbit/s transmission in a 2D beam steering AWG-based optical wireless communication system," in *2017 European Conference on Optical Communication (ECOC)*, 2017: IEEE, pp. 1-3.

[50]   H.-H. Lu *et al.*, "A 56 Gb/s PAM4 VCSEL-based LiFi transmission with two-stage injection-locked technique," *Ieee Photonics J,* vol. 9, no. 1, pp. 1-8, 2016.

[51]   C. D. Muñoz, J. Coronel, M. Varon, F. Destic, and A. Rissons, "Low-Timing-Jitter and Low-Phase-Noise Microwave Signal Generation Using a VCSEL-Based Optoelectronic Oscillator," *Ingeniería e Investigación,* vol. 42, no. 2, pp. e87189-e87189, 2022.

Chapter 6 Conclusion and Future work

6.1 Conclusion

This thesis aims to develop high-performance OFC sources based on two-section InAs QD MLLs for optical telecommunication applications. Overall, several milestones have been achieved during the development of this thesis. And the contents of each chapter are summarised below.

In Chapter 1, the background and motivation for developing superior OFCs for high-capacity optical communications were first presented. Followed by an illustration of the basics of how an OFC works. Then, different methods for OFCs generations were described. The major comb parameters that are relevant to coherent data transmission, together with the inherent properties of QD structures were also explained. As discussed, the two-section QD MLLs, owing to their compactness, low power consumption, high energy efficiency and potential for monolithic integrations, appear to be especially suitable for optical communication applications over other OFCs technologies.

In Chapter 2, the methodologies used for developing and evaluating the QD MLLs used throughout this thesis were introduced. Detailed information about the epitaxial layer structures of the laser devices, the fabrication process, and the experimental setups for device characteristics was given. The self-assembled InAs QDs were directly grown on GaAs to obtain emission at around 1.3 μm. A larger than the usual number of QD layers were employed to obtain the desired high optical gain. Besides, various cavity geometries were designed to study the effect of cavity configuration on mode-locking performance, involving a total of two different ridge structures (the ridged waveguide and the tapered waveguide) and five different SA-to-gain length ratios (from 1: 3 to 1: 7).

Chapter 3 investigates the impact of cavity configurations on room-temperature lasing performance. I found that, for a given cavity length, the devices with tapered waveguide structures typically emit at a lower current density level with a higher slope efficiency than those with ridged waveguide structures. Hence, the tapered waveguide structure should be more suitable for high-power applications. Meanwhile, a 25.5 GHz ridged QD MLL was chosen as an example for a systematic study of mode-locking characteristics in both spectra and temporal domains.

Chapter 4 presents the temperature-dependent performance of QD MLLs. Laser devices with different cavity configurations were extensively studied over a wide range of working temperatures. The measured *L-I* curves indicate that the devices with a longer cavity length could operate in a broader temperature range under a wider driving condition. Moreover, the tapered structure exhibits better thermal stability than the conventional ridged waveguide structure owing to its larger resonant area for heat dissipation. In addition, I reported a stable 25.5 GHz QD mode-locked comb source that can maintain GS emission to a world-record high temperature (120 °C) with a tiny variation in tone spacing (~ 0.07 GHz). The device showed a reasonable broad comb bandwidth (4.81 nm and 31 tones within a 6 dB window) even at an elevated temperature of 100 °C, corresponding to an averaged RIN of -146 dBc/Hz in the frequency range 0.5 GHz to 10 GHz. Those results suggest that the InAs QD MLLs could be used as ultra-stable comb sources in high-capacity and low-power consumption optical communications.

In Chapter 5, I successfully demonstrated the potential of our fabricated QD mode-locked OFCs in two application scenarios in the optical communication field, that is the optical data transmission through fibre-optic cables and air. An ultrashort two-section InAs QD MLL with a fundamental repetition rate of ~ 100 GHz was developed as the multi-wavelength light source. By pumping the gain

section and leaving the SA section floating, nearly Fourier-transform-limited pulses can be observed in the entire test range. The typical integrated RIN of the whole spectrum and a filtered tone are −152 and −137 dB Hz^{-1} in the range of 100 MHz to 10 GHz, respectively. In both cases, seven tones were selected as optical carriers for realising the system-level data transmission. And our devices succeed in realising up to 128 Gbit s^{-1} λ^{-1} PAM-4 5-km SSMF transmission and up to 64 Gbit s^{-1} λ^{-1} NRZ 2-m FSO transmission. The BER plots, together with the captured eye diagrams indicate that our QD mode-locked OFCs are a promising candidate for future high-speed optical communication networks.

6.2 Future work

Over the last few years, our society becomes increasingly dependent on information transmission and processing [1]. The unprecedented growth in the proliferation of new emerging wireless applications and services has dramatically increased the demand for high data rate transmission. Under this circumstance, it is generally agreed that the future big-data-driven 5G and beyond networks should feature super-high data rate, almost zero latency, and anywhere-anytime connection requirements [2]. As a matter of fact, this is either infeasible or very costly when using solely optical fibre transmissions. Meanwhile, the demand for unoccupied and unregulated bandwidth for wireless communication systems has inevitably led to the extension of operation frequencies toward the THz frequency region [1]. Consequently, the THz transmission as a wireless backhaul extension of the optical fibres is considered as the main technology trend to break the barriers of optical communication and guarantee excellent performance for future network development and deployment [3]. At the same time, the THz wireless communication is also one of the technologies that little explored resources are needed for validation and exploitation, which can fully leverage the potential of current communication

systems [4-6].

Based on the research works in previous chapters, our future investigation will be devoted to the generation of THz beat signals using passively 100 GHz QD MLLs through monolithic or hybrid integration with multiple ring resonator-based add-drop filters. The schematic diagram of the proposed device is presented in Fig. 6.1. As shown, the QD mode-locked OFC source with 100 GHz mode-spacing should contain at least 11 lines within the 3dB bandwidth to ensure the THz gap formation. Then, the light emitted from the QD MLL will first be coupled into two resonant-ring based 2x2 add-drop filters with different geometrical parameters (MRR1 and MRR2), after which the corresponding resonant wavelengths will be transferred to the drop ports (λ_1 and λ_2, respectively), and those non-resonant wavelengths will be transmitted to the throughput port without loss [7]. Then, the two filtered wavelengths will be combined by a 3dB coupler, and the output signal will be collected by a uni-travelling-carrier photodiode (UTC-PD). Finally, the THz signal can be obtained by simply heterodyning the two extracted modes [8]. In this way, our mode-locked OFCs could expand their application as a compact, broad bandwidth, easy operation, and cost-effective light source in high-speed THz wireless communications for the upcoming big-data era.

It is undeniable that the performance of our InAs QD mode-locked OFCs still has room for improvement in multiple aspects, such as emission spectral bandwidth, output power, and pulse duration. To achieve the envisaged goals, the proposed works as a follow-up to this project are outlined below.
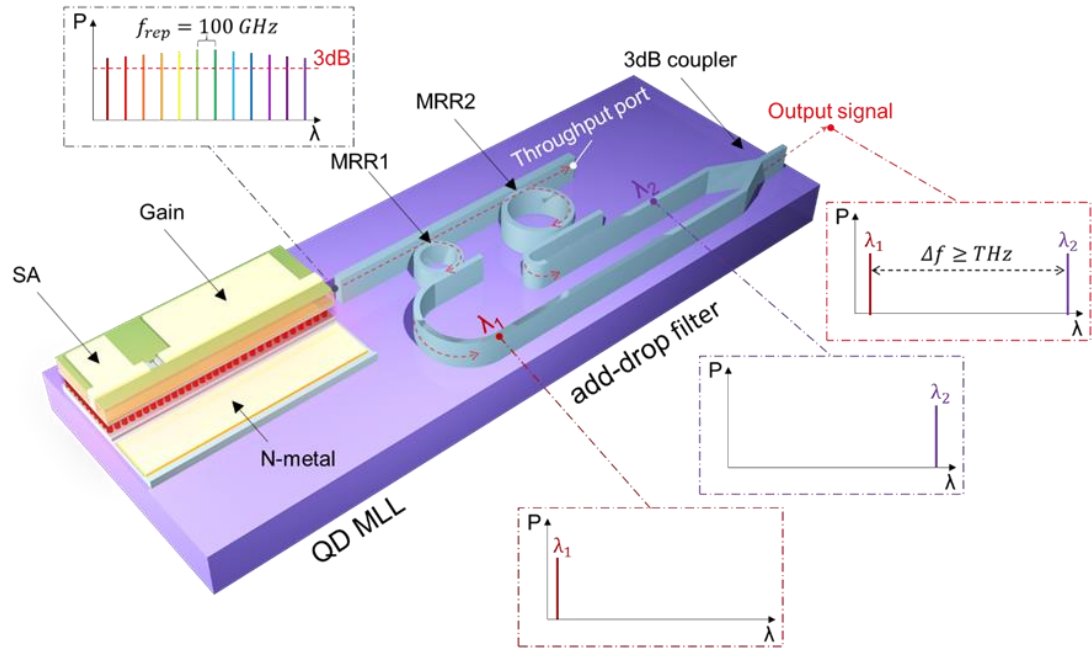
Figure 6.1 Prototype of Si-based THz beat signal generation using a 100 GHz two-section QD MLL and multiple ring-based optical add-drop filters.

6.2.1 QD mode-locked OFCs with ultra-broad bandwidth

The broadband sources are always favoured in optical communications since they can potentially offer more optical carriers for data transmission, hence, increasing the transmission capacity. To achieve the ultra-broad emission bandwidth for mode-locked OFCs, either chirped structure or hybrid QW/QD structure could be employed in the active region. Figure 6.2 shows the schematic diagrams for those two designed epitaxial structures.

The chirped structure contains multiple QD layers with different emission wavelengths (e.g., 1280 nm and 1230 nm), which can be achieved by changing the QDs composition [9], varying the QDs size [10], or modifying the matrix surrounding the QDs [11, 12]. As a result, there will exist two ground states, corresponding to the two strong peaks in the PL spectrum [13]. The overlapping between the PL spectrum of each peak enables a broad spectral width in the chirped structure.

On the other hand, the hybrid QW/QD structure introduces a single InGaAs QW located on the n-side relative to the QDs stack layers [14]. The QW layer will be engineered to have the lowest energy transition, thus, emitting at a wavelength that coincides with the emission wavelength of the second ES (ES2) of the QDs [15]. With optimal growth conditions, simultaneous three-state lasing could be achieved at room temperature. Meanwhile, it has been shown that the combined effects of QD's GS emission, QD ES1 emission and QW emission could achieve spectra with bandwidths over several hundred nm [16, 17]. If chirped QDs were used in hybrid structures, then, the spectral bandwidths could be further enhanced [18].
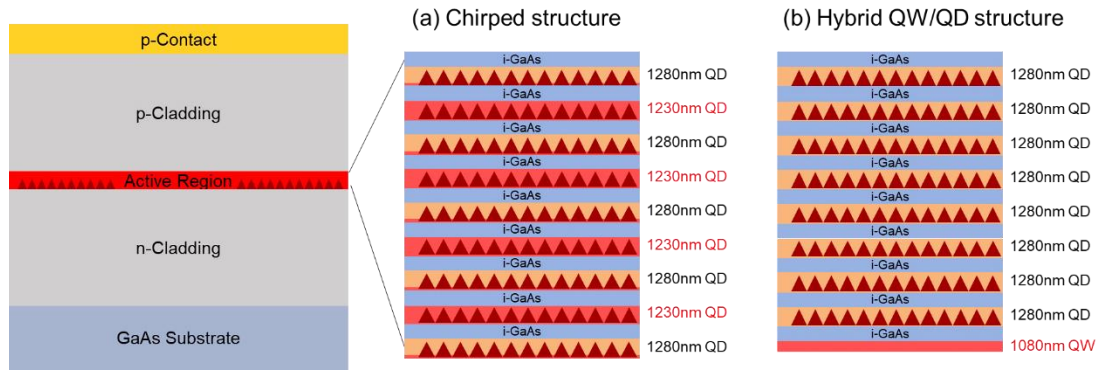

Figure 6.2 Schematic diagrams of a typical p-i-n laser diode with the proposed active region of (a) chirped structure, and (b) hybrid QW/QD structure.

6.2.2 High-power QD mode-locked OFCs

Apart from the broad-spectrum operation, researchers are also pursuing high-power OFCs that benefit from compactness, energy efficiency, and low running costs [19]. As an important quantity, the output power of frequency combs plays an essential role in many applications, such as metrology, light detection and ranging (LiDAR), and free-space optical transmission [20]. The QD mode-locked OFCs with high output power are extremely attractive since they offer the possibility to replace the large benchtop lasers and enable vast simplification of device setups.

171

As already discussed in Chapter 3, laser devices with the tapered-waveguide structure are ideal for high-power applications. Unfortunately, only few measurements have been performed on the tapered structure and much work remains to investigate, such as the pulse width, emission spectra, and mode-locking regime as a function of the driving conditions. Further measurements should be carried out. Also, when available, it would be interesting to compare the MLLs with different tapered angles.

In addition, it has been suggested that the anti-colliding pulse mode-locking (ACPML) configuration, where the low-reflectivity (LR) coating is implemented on the facet near the SA section, could significantly improve the output power of the pulses while maintaining the low timing-jitter [21, 22]. Therefore, OFCs generated by QD MLLs with anti-colliding structures could be the subject of future investigations.

6.3 Reference

[1]   T. Kleine-Ostmann and T. Nagatsuma, "A review on terahertz communications research," *Journal of Infrared, Millimeter, and Terahertz Waves,* vol. 32, no. 2, pp. 143-171, 2011.

[2]   A.-A. A. Boulogeorgos *et al.*, "Wireless terahertz system architectures for networks beyond 5G," *arXiv preprint arXiv:1810.12260,* 2018.

[3]   A.-A. A. Boulogeorgos *et al.*, "Terahertz technologies to deliver optical network quality of experience in wireless systems beyond 5G," *IEEE Communications Magazine,* vol. 56, no. 6, pp. 144-151, 2018.

[4]   M. Giordani, M. Polese, M. Mezzavilla, S. Rangan, and M. Zorzi, "Toward 6G networks: Use cases and technologies," *IEEE Communications Magazine,* vol. 58, no. 3, pp. 55-61, 2020.

[5]   P. Yang, Y. Xiao, M. Xiao, and S. Li, "6G wireless communications: Vision and potential techniques," *IEEE network,* vol. 33, no. 4, pp. 70-75, 2019.

[6]   I. F. Akyildiz, J. M. Jornet, and C. Han, "Terahertz band: Next frontier for wireless communications," *Physical communication,* vol. 12, pp. 16-32, 2014.

[7]   F. Monifi, J. Friedlein, Ş. Özdemir, and L. Yang, "A Robust and Tunable Add–Drop Filter Using Whispering Gallery Mode Microtoroid Resonator," *Journal of Lightwave Technology,* vol. 30, no. 21, pp. 3306-3315, 2012/11/01 2012. [Online]. Available: http://opg.optica.org/jlt/abstract.cfm?URI=jlt-30-21-3306.

[8]   M. Pelusi, H. Liu, D. Novak, and Y. Ogawa, "THz optical beat frequency generation from a single mode locked semiconductor laser," *Appl Phys Lett,* vol. 71, no. 4, pp. 449-451, 1997.

[9]   I. K. Han, D. C. Heo, J. D. Song, J. I. Lee, and J. I. Lee, "Study on superluminescent diodes using InGaAs-InAs chirped quantum dots," *Journal of the Korean Physical Society,* vol. 45, no. 5, pp. 1193-1195, 2004.

[10]   Y. Yoo, I. Han, and J. Lee, "High power broadband superluminescent diodes with chirped multiple quantum dots," *Electron Lett,* vol. 43, no. 19, pp. 1045-1047, 2007.

[11]   S. Ray, K. Groom, M. Beattie, H. Liu, M. Hopkinson, and R. Hogg, "Broad-band superluminescent light-emitting diodes incorporating quantum dots in compositionally modulated quantum wells," *Ieee Photonic Tech L,* vol. 18, no. 1, pp. 58-60, 2005.

[12]   L. Li, M. Rossetti, A. Fiore, L. Occhi, and C. Velez, "Wide emission spectrum from superluminescent diodes with chirped quantum dot multilayers," *Electron Lett,* vol. 41, no. 1, pp. 41-43, 2005.

[13]   D. Gammon, E. Snow, B. Shanabrook, D. Katzer, and D. Park, "Homogeneous linewidths in the optical spectrum of a single gallium arsenide quantum dot," *Science,* vol. 273, no. 5271, pp. 87-90, 1996.

[14]   S. Chen *et al.*, "Hybrid quantum well/quantum dot structure for broad spectral bandwidth emitters," *IEEE Journal of Selected Topics in Quantum Electronics,* vol. 19, no. 4, pp. 1900209-1900209, 2012.

[15]   S. Chen *et al.*, "Broad bandwidth emission from hybrid QW/QD structures," *2013 Conference on Lasers and Electro-Optics Pacific Rim (CLEOPR),* pp. 1-2, 2013.

[16]   S. Chen *et al.*, "GaAs-based superluminescent light-emitting diodes with 290-nm emission bandwidth by using hybrid quantum well/quantum dot structures," *Nanoscale Research Letters,* vol. 10, no. 1, pp. 1-8, 2015.

[17]   S. Chen *et al.*, "Ultra-broad spontaneous emission and modal gain spectrum from a hybrid quantum well/quantum dot laser structure," *Appl Phys Lett,* vol. 100, no. 4, p. 041118, 2012.

[18]   N. Peyvast *et al.*, "Development of broad spectral bandwidth hybrid QW/QD structures from 1000-1400 nm," in *Novel In-Plane Semiconductor Lasers XIII*, 2014, vol. 9002: SPIE, p. 900204.

[19]   L. Li, "The advances and characteristics of high-power diode laser materials processing," *Optics and lasers in engineering,* vol. 34, no. 4-6, pp. 231-253, 2000.

[20]   T. Fortier and E. Baumann, "20 years of developments in optical frequency comb technology and applications," *Communications Physics,* vol. 2, no. 1, pp. 1-16, 2019.

[21]   J.-P. Zhuang, V. Pusino, Y. Ding, S.-C. Chan, and M. Sorel, "Experimental investigation of anti-colliding pulse mode-locked semiconductor lasers," *Opt Lett,* vol. 40, no. 4, pp. 617-620, 2015.

[22]   J. Javaloyes and S. Balle, "Anticolliding design for monolithic passively mode-locked semiconductor lasers," *Opt Lett,* vol. 36, no. 22, pp. 4407-4409, 2011.

Appendix A

Fabrication Processes of MLLs

Version: IOP_20211124

Wafer: PIN laser structure on GaAs

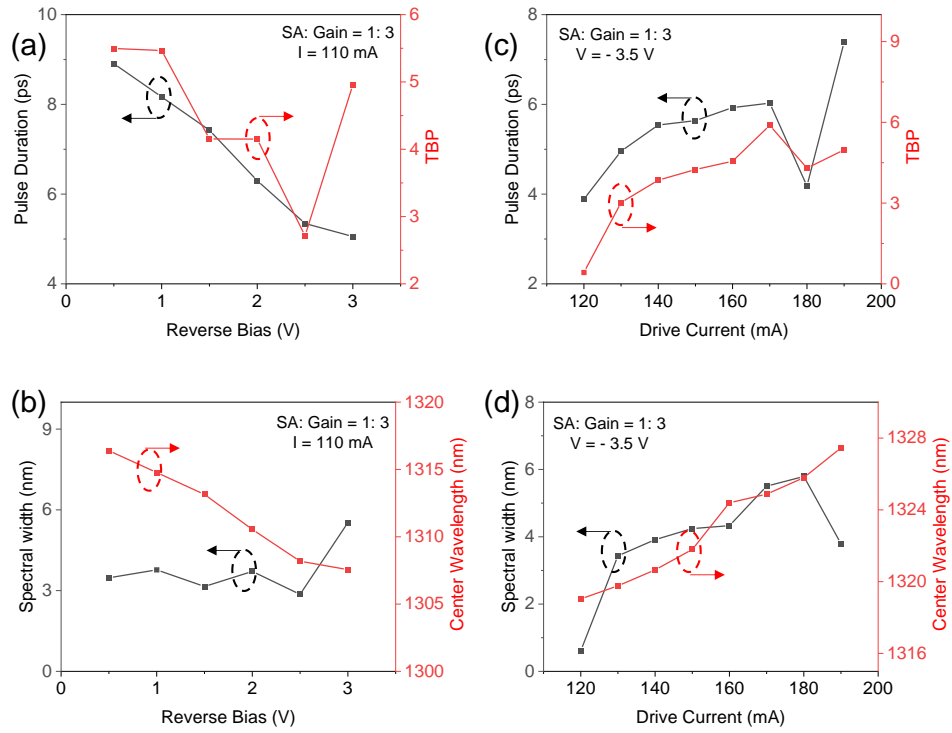| Step Name	Process	Note
1: Wafer Clean	Clean wafer after dicing into 3 cm x 3 cm. Steps: 1. Rinse in acetone for 5 mins. 2. Rinse in IPA for 5 mins. 3. Rinse in water for 5 mins. 4. Dry wafer with N_2 gas.	
2. 1st spin coating SPR220 + LOR10B	1. Prebake: 150 ^{0}C for 3 mins. 2. Spin coating LOR5A @ 3000 rpm for 1 min, thickness ~ 500 nm. 3. Pre-exposure bake: 180 ^{0}C for 5 mins. 4. Spin coating SPR220-3.0 @ 2000 rpm for 1 min, thickness ~ 4 µm. 5. Post bake: 115 ^{0}C for 90s.	
3. 1st lithography (Laser direct writing)	Define P-metal pattern. Parameters: a. Laser power: 60 mW. b. Focal length: 5 mm. c. Intensity: 60. d. Filter: 100.	Post exposure bake @ 115 ^{0}C for 90s;
4: Development	1. Rinse in MIF-300 for 1 min. 2. Rinse in water for 30s. 3. Dry wafer with N_2 gas. 4. O_2 plasma clean.	
5: 1st P-metal deposition (Ridge)	Parameters: a. Ti_20 nm/ Pt_20 nm / Ti_20 nm /Au_200 nm. b. Vacuum Pressure < 5e-6.	
6. Lift-off	1. Rinse in acetone. 2. Rinse in IPA. 3. Rinse in water. 4. Rinse in PG remover. 5. Rinse in water. 6. Dry wafer with N_2 gas	
7: 1st annealing (Ridge)	Thermal annealing. 1. 425 ^{0}C for 1 min.	

8: Hard-mask growth	Deposit hard mask on wafer.
	  1. ICPECVD
	  2. Deposit temperature: 80 ^{0}C.
	  3. Deposit rate: 25.8 nm/min.
	  4. Deposit time: 20 mins.
		Thickness of SiO$_2$: around 500 nm.

9: 2st spin coating AR300-80 +SPR220-3.0	1. Prebake: 150 ^{0}C for 3 mins. 2. Spin coating AR300-80 @ 4000 rpm for 3 mins, thickness ~ 3. Pre-exposure bake: 180 ^{0}C for 3 mins. 4. Spin coating SPR220-3.0, thickness ~ 4 µm. 5. Post bake: 115 ^{0}C for 90s.	

10: 2st lithography (Laser direct writing)	Define Ridge pattern.
	Parameters:
	  a. Laser power: 60 mW.
	  b. Focal length: 5 mm.
	  c. Intensity: 60.
	  d. Filter: 100.	

11: Development	1. Rinse in MIF-300 for 1 min. 2. Rinse in water for 30s. 3. Dry wafer with N$_2$ gas. 4. O$_2$ plasma ash.	

12: 1st SiO$_2$ dry etching	RIE etching
	  1. Pressure: 100 mTorr.
	  2. Etch time: 19 mins.
	  3. Etch temperature: 10 ^{0}C.
	  4. O$_2$ plasma ash.
		Etching rate: 30 nm/min

13: Removing Resist	1. Rinse in hot bath (70 ^{0}C). 2. PG remover (1165). 3. Rinse in DI water. 4. Dry wafer with N$_2$ gas.	

14: III-V ridge etching	ICP etching
	  1. BCl$_3$/Cl$_2$/Ar: 10/6/4 sccm.
	  2. Etch depth: 1.6 – 1.8 µm.
	  3. O$_2$ plasma ash.
		Etching rate: 16.8 nm/min.

15: Passivation	Deposit passivation layer on wafer.
	  1. ICPECVD
	  2. Deposit temperature: 80 ^{0}C
	  3. Deposit rate: 25.8 nm/min
	  4. Deposit time: 20 mins.
		Thickness of SiO$_2$: around 500 nm.

16: 3rd spin coating AR300-80 + SPR220-3.0	1. Prebake: 150 ^{0}C for 3 mins. 2. Spin coating AR300-80 @ 4000 rpm for 3 mins, thickness ~ 3. Pre-exposure bake: 180 ^{0}C for 3 mins. 4. Spin coating SPR220-3.0, thickness ~ 4 µm. 5. Post bake: 115 ^{0}C for 90s.	AR300-80 is an adhesion promoter.

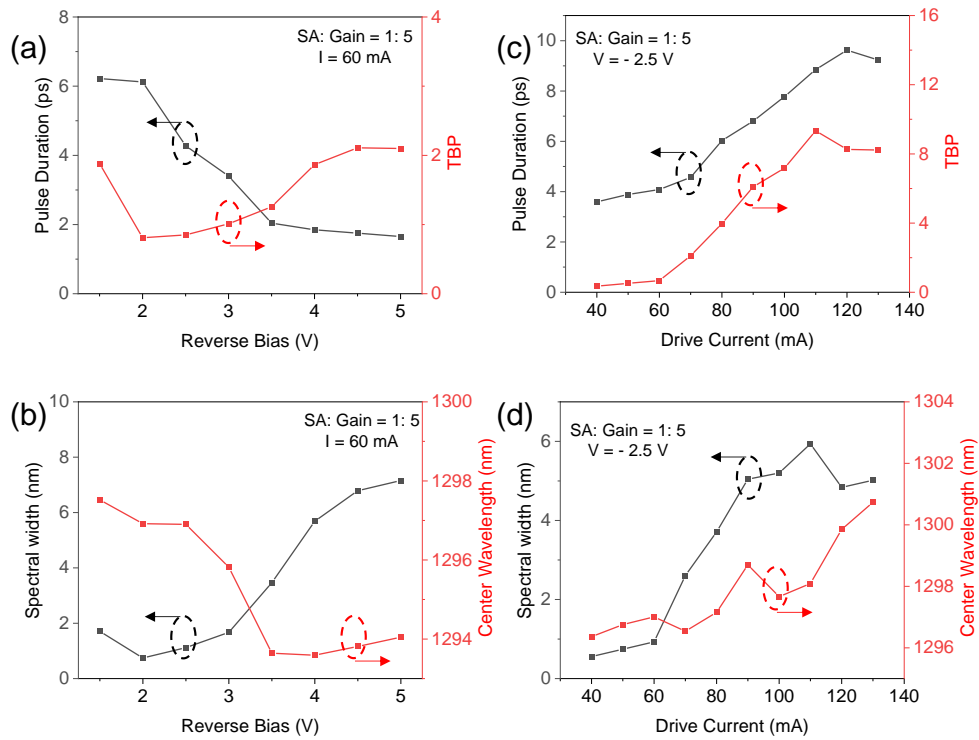| 17: 3rd lithography (Laser direct writing) "Open window"	Define P-contact metal pattern.
	Parameters:
	  a. Laser power: 60 mW.
	  b. Focal length: 5 mm.
	  c. Intensity: 50.
	  d. Filter: 100.	

18: Development	1. Rinse in MIF-300 for 1 min. 2. Rinse in water for 30s. 3. Dry wafer with N_2 gas. 4. O_2 plasma clean.	
19: 2nd SiO_2 dry etching	RIE etching 5. Pressure: 100 mTorr. 6. Etch time: 20 mins. 7. Etch temperature: 10 ^{0}C 5. O_2 plasma ash.	Etching rate: 30 nm/min
20: Removing Resist	1. Rinse in hot bath. 2. PG remover (1165). 3. Rinse in DI water. 4. Dry wafer with N_2 gas.	
21: 4th spin coating LOR10B + SPR220	1. Prebake: 150 ^{0}C for 3 mins. 2. Spin coating LOR10B @ 3000 rpm for 1 min, thickness ~ 1 µm. 3. Pre-exposure bake: 180 ^{0}C for 5 mins. 4. Spin coating SPR220-3.0 @ 2000 rpm for 1 min, thickness ~ 4 µm. 5. Post bake: 115 ^{0}C for 90s.	

22: 4th lithography (Laser direct writing) "P-contact"	Define 'P-contact" pattern.
	Parameters:
	  a. Laser power: 60 mW.
	  b. Focal length: 5 mm.
	  c. Intensity: 60.
	  d. Filter: 100.	

23: Development	1. Rinse in MIF-300 for 1 min. 2. Rinse in water for 30s. 3. Dry wafer with N_2 gas. 4. O_2 plasma clean.	

24: 2nd P-metal deposition (Contact)	Parameters:
	  a. Ti_20 nm/ Au_400 nm / Ti_20 nm /Au_400 nm/ Ti_20 nm /Au_600 nm.
	  b. Vacuum Pressure < 5e-6.	

25: Lift-off	1. Rinse in acetone. 2. Rinse in IPA. 3. Rinse in water. 4. Rinse in PG Remover. 5. Rinse in water. 6. Dry wafer with N_2 gas.	
26: 5th spin	1. Prebake: 150 ^{0}C for 3 mins.	

coating SPR220	2. Spin coating SPR220-3.0, thickness ~ 2 μm. 3. Post bake: 115 ^{0}C for 90s.	

27: 5th lithography (Laser direct writing) "Gap Etch"	Define 'P-contact" pattern.
	Parameters:
	  a. Laser power: 60 mW.
	  b. Focal length: 5 mm.
	  c. Intensity: 60.
	  d. Filter: 100.	

28: Development	1. Rinse in MIF-300 for 1 min. 2. Rinse in water for 30s. 3. Dry wafer with N_2 gas. 4. O_2 plasma clean.	
29: III-V wet etching	1. Wet etching for 1 min in mixed solution (Citric: $H_2O_{2:}$ H_2O = 10:1:10) 2. Rinse in water for 30s.	Etching rate: 200 nm/min.
30: Removing Resist	1. Rinse in acetone. 2. Rinse in IPA. 3. Rinse in DI water. 4. Dry wafer with N_2 gas.	
29: Lapping	Lapping the sample to ~ 120 μm.	

30: N-metal deposition	Parameters:
	  a. Ni_25 nm/ Ge_32.5 nm / Au_65 nm /Ti_20 nm/Au_200 nm.
	  b. Vacuum Pressure < 5e-6.	

31: Thermal annealing	Thermal annealing. 1. 350 ^{0}C for 1 min.	

Appendix B

SA: Gain = 1: 3

SA: Gain = 1: 5

SA: Gain = 1: 6

SA: Gain = 1: 7